8-26-2022 11:00 AM

Improved Imaging Of Dense Non-Aqueous Phase Liquids With Three-Dimensional Surface-To-Horizontal Borehole Electrical Resistivity Tomography (S2HB ERT)

Maxwell L. Servos, *The University of Western Ontario*

Supervisor: Power, Christopher A., *The University of Western Ontario*

A thesis submitted in partial fulfillment of the requirements for the Master of Engineering Science degree in Civil and Environmental Engineering

Abstract

Clean-up of sites polluted with dense non-aqueous phase liquids (DNAPLs) remain a highly challenging problem. Numerous technologies are available for remediating DNAPL-contaminated sites, but their performance relies on accurate characterization and monitoring of the subsurface. Electrical resistivity tomography (ERT) is a well-established and widely used geophysical method that has been used effectively for mapping subsurface features and processes of interest. ERT can gather large volumes of continuous subsurface information in a non-destructive, cost-effective, and time-efficient manner, and exhibits highly desirable characteristics for application to DNAPL sites. However, the most traditional configuration for employing ERT is from the surface, and this suffers from poorer imaging quality with increasing depth from the surface. To overcome this issue, which is particularly problematic at DNAPL sites, ERT may take advantage of horizontal borehole technology to enhance image quality at depth.

The objective of this thesis is to evaluate the performance of novel three-dimensional ERT that utilizes both the ground surface and horizontal boreholes to improve characterization and monitoring capabilities of ERT at DNAPL sites. A range of numerical and laboratory tank experiments were conducted on various DNAPL targets in different environments (e.g., water and plastic, sand and NAPL). Results demonstrate the high potential of 3D S2HB ERT for characterizing DNAPL targets, especially when compared to surface ERT. Furthermore, implementation of a single borehole with a 2D surface array (i.e., S2HB-1BH) provided adequate resolving ability compared to a S2HB configuration that utilized a 2D horizontal borehole array matching the surface array (e.g., 11 surface lines and 11 borehole lines) (i.e., S2HB-FULL). This enhanced our understanding of ideal borehole electrode implementation. A full 2D array of boreholes would be highly impractical at DNAPL sites, and the adequate performance by a more practical single borehole is highly encouraging.

Keywords: Dense non-aqueous phase liquids, electrical resistivity tomography, horizontal boreholes

Summary for Lay Audience

The release of pollutants from industrial applications can be very damaging to the environment. Many of these pollutants leach into the ground and can cause unsafe groundwater conditions. If not managed in a timely manner, these pollutants can be a long-term source of groundwater contamination. There are many methods for cleaning up pollutants from the ground, but for them to be effective, the location and volume of these pollutants needs to be determined. This is a major challenge because traditional methods for determining properties of the ground, such as drilling or digging, can be destructive and gather information over a very limited space, thereby being ineffective for this task. A new method of locating these pollutants was therefore desired. This was accomplished using a geophysical technique that sends electrical current into the ground and monitors where, and how fast, the current moves to produce an image much like an X-ray. It also has the advantage of not being destructive and can gather data over very large volumes with little effort compared to traditional methods. In this study, a brand-new configuration is proposed that uses horizontally drilled holes in the ground to use more sensors and get better images. A range of numerical models and laboratory experiments in a plastic tank were used to understand this new configuration and show that it has the potential to be used to help clean up pollutants in the ground.

Co-Authorship Statement

This thesis was written with accordance to the guidelines for an Integrated Article specified by the School of Graduate and Postgraduate Studies at the University of Western Ontario. The candidate is responsible for the collection and analysis of numerical and laboratory data and drafting all chapters of this thesis. Dr. Christopher Power provided initial motivation for this research, assisted with laboratory experiments and numerical modeling, provided analysis for the resulting data, and provided revisions of this thesis. The co-authorship breakdown of Chapter 3 is as follows:

Authors: Maxwell Servos, Christopher Power

Contributions:

Maxwell Servos conducted numerical models and laboratory experiments, interpreted the results, and was the lead author for this paper.

Christopher Power supervised the laboratory experiments and numerical models, provided insight for the results, and reviewed the draft of the chapter 3.

Acknowledgments

Thank you to my supervisor Christopher Power. I am incredibly grateful for your support, guidance, and encouragement. Your efforts have helped me achieve academic success further than I ever would have thought possible. It is a great privilege to have had you as my supervisor, and I appreciate every opportunity you have given me.

Thank you to Dr. Clare Robinson, Dr. Jason Gerhard, and the RESTORE research group. I am very appreciative for all the feedback, help, and experiences I have gotten to share with you all throughout my graduate and undergraduate studies.

Finally, I would like to thank my family and friends. Your unwavering love and support has provided the ultimate foundation for me to grow as a person and strive for my dreams.

Table of Contents

List of Tables

List of Figures

Chapter 1

1 Introduction

1.1 Research Background

Groundwater contamination from hazardous chlorinated solvents is a major consequence from their widespread production that began in the 1970s (Pankow et al., 1996). Many of these contaminants fall under the category of dense non-aqueous phase liquids (DNAPLs). DNAPL products, such as coal tar, trichloroethylene (TCE) and perchloroethylene (PCE) have stable chemical structures and degrade very slowly in the environment. This is problematic because it allows them to serve as long-term sources of groundwater contamination (Lin et al., 2018). A very small amount of dissolved DNAPL is all that is required to cause the groundwater conditions to negatively impact the health of humans and the surrounding ecosystem (Pan et al., 2020).

Remediating sites contaminated with DNAPLs has long been, and remains, a major environmental challenge (Yang et al., 2022). Many remediation technologies such as thermal technologies, *in situ* chemical oxidation, and *in situ* biodegradation (e.g., Li & Shwartz, 2004; Soga et al., 2004) depend on accurate characterization of the subsurface due to complex heterogeneity (Zhang et al., 2008). Accurate time-lapse monitoring is also necessary for tracking the performance of the chosen remediation strategy (e.g., Chambers et al., 2010). Subsurface characterization of features, and monitoring of time-lapse changes, are therefore an essential aspect of DNAPL remediation (Guo et al., 2021).

Traditional methods for characterizing the subsurface, such as core sampling, trial pits, and monitoring wells, are some of the most common methods employed on contaminated sites (e.g., Griffin and Watson, 2002; Kueper et al., 2004; McMillan et al., 2018). However, these methods suffer from many limitations including labor intensity, cost, poor sampling density, and potential remobilization of contaminants though preferential pathways created from disturbing the subsurface (Kueper et al., 2004).

More recently, geophysical methods such as electrical resistivity tomography (ERT) have been effectively used for characterizing the subsurface (e.g. Binley et al., 2015; Slater and

Binley , 2021). ERT is a non-invasive geophysical method that induces an electric current into the ground and characterizes the subsurface based on resistivity data (Ducut et al., 2022). ERT is also spatially continuous giving it the potential to provide more complete site characterization (e.g., Brewster et al., 1995; Revil et al., 2012). Previous studies have demonstrated the potential of ERT for characterizing DNAPLs in the subsurface (e.g., Chambers et al., 2004; Deng et al., 2017; Trento et al., 2021;). ERT can characterize DNAPLs as distinct targets in the subsurface due to the contrast between resistive DNAPL source zones and the conductive groundwater (Lucius et al., 1992).

Generally, most studies examine surface ERT in which electrodes are only applied to the ground surface (e.g., Forquet and French, 2012; von Bülow et al., 2021; Mohammed Nazifi et al., 2022). Although surface ERT is very practical to implement on a DNAPL site, its subsurface characterization is often limited due to loss of resolution with depth (Folch et al., 2020; Wang et al., 2020). To characterize the subsurface below the capable depth of surface ERT, studies have also examined cross-hole ERT in which electrodes are placed in vertical boreholes (e.g., Chambers et al., 2010; Wang et al., 2020, Almpanis et al., 2021b). However, cross-hole ERT can be impractical and expensive to implement on a DNAPL site due the number of vertical boreholes required to accurately characterize the site (Chambers et al. 2010).

More recently, studies have been completed with electrodes installed in tunnels and horizontal boreholes. Tunnel-to-tunnel configurations were used to image geological features in advance of tunnel borings (Danielsen and Dahlin, 2010) and image disruptive geological structures ahead of mining (van Schoor and Binley, 2010), while Power et al. (2015) conducted numerical and laboratory experiments to demonstrate improved imaging of DNAPL source zones and DNAPL mass changes occurring during their remediation. Kiflu et al. (2016) presented a direct-push technology technique to implant electrodes into the subsurface along horizontal lines (e.g., Kiflu et al., 2016). All aforementioned studies demonstrated significantly improved ERT imaging due to the benefit of deploying electrodes along horizontal lines above and below the target zone, increasing the proximity of electrodes to the target. However, these studies were only completed in two-dimensions, limiting the total characterization of the subsurface. This is particularly problematic for

DNAPL source zones due to their high lateral and vertical heterogeneity, which makes it overly simplistic and risky to assume uniformity in third dimension. As a result, horizontal borehole ERT should be demonstrated in three dimensions (3D) to accurately characterize the complex heterogeneity of these source zones. This could provide more accurate characterization and monitoring capability in subsurface regions that surface ERT is unable to resolve, which can lead to improved remedial programs at DNAPL sites.

The objective of this thesis was to evaluate 3D surface-to-horizontal borehole (S2HB) ERT to demonstrate improved DNAPL target characterization. Numerical models and laboratory experiments were completed using numerous 3D electrode configurations (with various numbers of horizontal boreholes) and target arrangements to analyze 3D S2HB ERT for a variety of circumstances. This allowed for a comprehensive examination of the imaging improvements and limitations of 3D S2HB ERT.

1.2 Research Objectives

The overall goal of this thesis is to evaluate the potential of S2HB ERT in three dimensions for the purpose of characterizing DNAPL source zones. To complete this goal, two subobjectives were addressed:

1. Conduct three-dimensional numerical modeling and laboratory experiments to demonstrate the potential of S2HB ERT in comparison to surface ERT for characterization of DNAPL source zones in the subsurface.

2. Conduct a sensitivity analysis of S2HB ERT by comparing multiple S2HB electrode configurations and target arrangements in the subsurface to enhance the understanding of optimal borehole electrode placement.

1.3 Thesis Outline

This thesis is written in an “Integrated Article” format. A brief description of the subsequent chapters presented are as follows:

- Chapter 2: summarizes the scientific literature relevant to dense non-aqueous phase liquids (DNAPLs) and electrical resistivity tomography (ERT). DNAPL

characteristics and remediation techniques are discussed, as well as ERT basic theory, electrode configurations, and data processing.

- Chapter 3: details the methodology and presents the results for numerical modeling and laboratory experiments used to evaluate S2HB ERT in three-dimensions to improve the subsurface characterization of DNAPL source zones.
- Chapter 4: summarizes the 3D S2HB ERT findings for surface ERT comparison and the sensitivity analysis. Recommendations for future work are also suggested.
- Appendices: supplementary numerical model results

1.4 References

Almpanis, A., Tsourlos, P., Vargemezis, G. and Papazachos, C. (2021), Application of crosshole electrical resistivity tomography measurements under the influence of horizontally slotted plastic cased boreholes. Near Surface Geophysics, 20: 46-63. https://doi.org/10.1002/nsg.12187

Binley, A., Hubbard, S., Huisman, J., Revil, A., Robinson, D., Singha, K., & Slater, L. (2015). The emergence of hydrogeophysics for improved understanding of subsurface processes over multiple scales _ Enhanced Reader. *Water Resources Reseach*, *51*.

Brewster, M., Annan, A., Greenhouse, J., Kueper, B., Olhoeft, G., Redman, J., & Sander, K. (1995). *Observed Migration of a Controlled DNAPL Release by Geophysical Methods*.

Cardarelli, E., & di Filippo, G. (2009). Electrical resistivity and induced polarization tomography in identifying the plume of chlorinated hydrocarbons in sedimentary formation: A case study in Rho (Milan - Italy). *Waste Management and Research*, *27*(6), 595–602. https://doi.org/10.1177/0734242X09102524

Chambers, J. E., Loke, M. H., Ogilvy, R. D., & Meldrum, P. I. (2004). Noninvasive monitoring of DNAPL migration through a saturated porous medium using electrical impedance tomography. *Journal of Contaminant Hydrology*, *68*(1–2), 1–22. https://doi.org/10.1016/S0169-7722(03)00142-6

Chambers, J. E., Wilkinson, P. B., Wealthall, G. P., Loke, M. H., Dearden, R., Wilson, R., Allen, D., & Ogilvy, R. D. (2010a). Hydrogeophysical imaging of deposit heterogeneity and groundwater chemistry changes during DNAPL source zone bioremediation. *Journal of Contaminant Hydrology*, *118*(1–2), 43–61. https://doi.org/10.1016/j.jconhyd.2010.07.001

Danielsen, B. E., & Dahlin, T. (2010). Numerical modeling of resolution and sensitivity of ERT in horizontal boreholes. *Journal of Applied Geophysics*, *70*(3), 245–254. https://doi.org/10.1016/j.jappgeo.2010.01.005

Deng, Y., Shi, X., Xu, H., Sun, Y., Wu, J., & Revil, A. (2017). Quantitative assessment of electrical resistivity tomography for monitoring DNAPLs migration – Comparison with high-resolution light transmission visualization in laboratory sandbox. *Journal of Hydrology*, *544*, 254–266. https://doi.org/10.1016/j.jhydrol.2016.11.036

Dhu, T., & Heinson, G. (2004). Numerical and laboratory investigations of electrical resistance tomography for environmental monitoring. Exploration Geophysics, 35(1), 33–40. https://doi.org/10.1071/EG04033

Ducut, J. D., Alipio, M., Go, P. J., Concepcion, R., Vicerra, R. R., Bandala, A., & Dadios, E. (2022). A Review of Electrical Resistivity Tomography Applications in Underground Imaging and Object Detection. In *Displays* (Vol. 73). Elsevier B.V. https://doi.org/10.1016/j.displa.2022.102208

Folch, A., del Val, L., Luquot, L., Martínez-Pérez, L., Bellmunt, F., le Lay, H., Rodellas, V., Ferrer, N., Palacios, A., Fernández, S., Marazuela, M. A., Diego-Feliu, M., Pool, M., Goyetche, T., Ledo, J., Pezard, P., Bour, O., Queralt, P., Marcuello, A., … Carrera, J. (2020). Combining fiber optic DTS, cross-hole ERT and time-lapse induction logging to characterize and monitor a coastal aquifer. *Journal of Hydrology*, *588*. https://doi.org/10.1016/j.jhydrol.2020.125050

Forquet, N., & French, H. K. (2012). Application of 2D surface ERT to on-site wastewater treatment survey. *Journal of Applied Geophysics*, *80*, 144–150. https://doi.org/10.1016/j.jappgeo.2012.02.002

Griffin, T., & Watson, K. (2002). *A Comparison of Field Techniques for Confirming Dense Nonaqueous Phase Liquids*.

Guo, Q., Shi, X., Kang, X., Hao, S., Liu, L., & Wu, J. (2021). Evaluation of the benefits of improved permeability estimation on high-resolution characterization of DNAPL distribution in aquifers with low-permeability lenses. *Journal of Hydrology*, *603*. https://doi.org/10.1016/j.jhydrol.2021.126955

Kiflu, H., Kruse, S., Loke, M. H., Wilkinson, P. B., & Harro, D. (2016). Improving resistivity survey resolution at sites with limited spatial extent using buried electrode arrays. *Journal of Applied Geophysics*, *135*, 338–355. https://doi.org/10.1016/j.jappgeo.2016.10.011

Kueper, B. H., & Great Britain. Environment Agency. (2004). *An illustrated handbook of DNAPL transport and fate in the subsurface*. Environment Agency.

Li, X. D., & Schwartz, F. W. (2004). DNAPL remediation with in situ chemical oxidation using potassium permanganate - II. Increasing removal efficiency by dissolving Mn oxide precipitates. *Journal of Contaminant Hydrology*, *68*(3–4), 269–287. https://doi.org/10.1016/S0169-7722(03)00145-1

Lin, K. S., Mdlovu, N. V., Chen, C. Y., Chiang, C. L., & Dehvari, K. (2018). Degradation of TCE, PCE, and 1,2–DCE DNAPLs in contaminated groundwater using polyethylenimine-modified zero-valent iron nanoparticles. *Journal of Cleaner Production*, *175*, 456–466. https://doi.org/10.1016/j.jclepro.2017.12.074

Loke, M. H., Chambers, J. E., Rucker, D. F., Kuras, O., & Wilkinson, P. B. (2013). Recent developments in the direct-current geoelectrical imaging method. *Journal of Applied Geophysics*, *95*, 135–156. https://doi.org/10.1016/j.jappgeo.2013.02.017

Lucius1, J. E., Olhoeft1, G. R., Hill1, P. L., & Duke2, S. K. (1992). *PROPERTIES AND HAZARDS OF 108 SELECTED SUBSTANCES-1992 EDITION*.

McMillan, L. A., Rivett, M. O., Wealthall, G. P., Zeeb, P., & Dumble, P. (2018). Monitoring well utility in a heterogeneous DNAPL source zone area: Insights from proximal multilevel sampler wells and sampling capture-zone modeling. *Journal of Contaminant Hydrology*, *210*, 15–30. https://doi.org/10.1016/j.jconhyd.2018.02.001

Mohammed Nazifi, H., Gülen, L., Gürbüz, E., & Pekşen, E. (2022). Time-lapse electrical resistivity tomography (ERT) monitoring of used engine oil contamination in laboratory setting. *Journal of Applied Geophysics*, *197*. https://doi.org/10.1016/j.jappgeo.2022.104531

Pan, Y., Zeng, X., Xu, H., Sun, Y., Wang, D., & Wu, J. (2020). Assessing human health risk of groundwater DNAPL contamination by quantifying the model structure uncertainty. *Journal of Hydrology*, *584*. https://doi.org/10.1016/j.jhydrol.2020.124690

Pankow, J. F., & Cherry, J. A. (1996). *DENSE CHLORINATED SOLVENTS and other DNAPLs in Groundwater: History, Behavior, and Remediation*.

Power, C., Gerhard, J. I., Karaoulis, M., Tsourlos, P., & Giannopoulos, A. (2014). Evaluating four-dimensional time-lapse electrical resistivity tomography for monitoring DNAPL source zone remediation. Journal of Contaminant Hydrology, 162–163, 27–46. https://doi.org/10.1016/j.jconhyd.2014.04.004

Power, C., Gerhard, J. I., Tsourlos, P., Soupios, P., Simyrdanis, K., & Karaoulis, M. (2015). Improved time-lapse electrical resistivity tomography monitoring of dense non-aqueous phase liquids with surface-to-horizontal borehole arrays. *Journal of Applied Geophysics, 112*, 1–13. https://doi.org/10.1016/j.jappgeo.2014.10.022

Revil, A., Karaoulis, M., Johnson, T., & Kemna, A. (2012). Review: Some low-frequency electrical methods for subsurface characterization and monitoring in hydrogeology. *Hydrogeology Journal*, *20*(4), 617–658. https://doi.org/10.1007/s10040-011-0819-x

Slater, L., & Binley, A. (2021). Advancing hydrological process understanding from long-term resistivity monitoring systems. In Wiley Interdisciplinary Reviews: Water (Vol. 8, Issue 3). John Wiley and Sons Inc. https://doi.org/10.1002/wat2.1513

Soga, K., Page, J. W. E., & Illangasekare, T. H. (2004). A review of NAPL source zone remediation efficiency and the mass flux approach. *Journal of Hazardous Materials*, *110*(1–3), 13–27. https://doi.org/10.1016/j.jhazmat.2004.02.034

Trento, L. M., Tsourlos, P., & Gerhard, J. I. (2021). Time-lapse electrical resistivity tomography mapping of DNAPL remediation at a STAR field site. *Journal of Applied Geophysics*, *184*. https://doi.org/10.1016/j.jappgeo.2020.104244

van Schoor, M., & Binley, A. (2010). *In-mine (tunnel-to-tunnel) electrical resistance 1 tomography in South African platinum mines*

von Bülow, R., Klitzsch, N., & Wellmann, F. (2021). Strategies to overcome near surface disturbances while inverting time-lapse surface ERT data. *Journal of Applied Geophysics*, *195*. https://doi.org/10.1016/j.jappgeo.2021.104463

Wang, H., Lin, C. P., & Liu, H. C. (2020). Pitfalls and refinement of 2D cross-hole electrical resistivity tomography. *Journal of Applied Geophysics*, *181*. https://doi.org/10.1016/j.jappgeo.2020.104143

Yang, P., Guo, H., Wang, Z., & Zhao, E. (2022). Influence of distribution characteristics of residual DNAPL on mass transfer in porous media under ethanol co-solvent flushing. *Journal of Hydrology*, *610*. https://doi.org/10.1016/j.jhydrol.2022.127932

Zhang, C., Yoon, H., Werth, C. J., Valocchi, A. J., Basu, N. B., & Jawitz, J. W. (2008). Evaluation of simplified mass transfer models to simulate the impacts of source zone architecture on nonaqueous phase liquid dissolution in heterogeneous porous media. *Journal of Contaminant Hydrology*, *102*(1–2), 49–60. https://doi.org/10.1016/j.jconhyd.2008.05.007

Zou, C., & Zhang, S. (2022). Precise estimation of subsurface moisture content based on laboratory measurement and 3D GPR field survey. *Journal of Applied Geophysics*, 104752. https://doi.org/10.1016/j.jappgeo.2022.104752

Chapter 2

2 Literature Review

This chapter summarizes the literature relevant to dense non-aqueous phase liquids (DNAPLs) and electrical resistivity tomography (ERT). The review begins by analyzing DNAPL characteristics, migration patterns, and remediation techniques. It then discusses the current state of knowledge of ERT including basic theory, electrode configurations, electrode array types, and ERT data processing.

2.1 Dense Non-Aqueous Phase Liquids

2.1.1 Introduction

The widespread production of hazardous chlorinated solvents began during World War II and were largely unrecognized as a major source of groundwater contamination until the 1970s (Pankow et al., 1996). Dense non-aqueous phase liquids (DNAPLs) refer to a specific class of chlorinated solvents that are denser than water. DNAPL products and biproducts such as polychlorinated biphenyls (PCBs), trichloroethylene (TCE), and coal tar were present in many industrial and commercial applications such as petroleum, electronic, and cleaning products (Pankow et al., 1996). Generally, DNAPLs are considered immiscible in water, however they are slightly soluble. This creates a groundwater contamination risk because a miniscule amount of dissolved DNAPL can cause the groundwater conditions to no longer be safe for consumption (Kueper et al., 2004; Pan et al., 2020; Koohbor et al., 2022). DNAPLs can therefore act as a long-term source of groundwater contamination, capable of polluting enormous amounts of groundwater (Karaoglu et al. 2019).

2.1.2 DNAPL Migration

DNAPL migration within the subsurface occurs under complex multiphase flow conditions. Factors such as the flow of groundwater, porous media properties, and gravity all need to be considered when analyzing DNAPL migration (Karaoglu et al., 2019). Even small changes to the porous media have been demonstrated to affect the migration path and residual locations of DNAPL (Poulsen and Kueper, 1992).

Figure 2-1 illustrates general DNAPL migration and distribution from a near-surface release. After the DNAPL release at the surface, the DNAPL migration is both vertical and lateral, following the path of least resistance. Small residuals and large pools form at the trailing end of DNAPL migration due to pore-scale hydrodynamic instabilities, held together by capillary forces. In most porous media, even when a large hydraulic gradient is present, re-mobilization of the residual DNAPL is not possible (Kueper et al., 2004). The DNAPL pools and residuals slowly dissolve into plumes and are therefore long-term sources of groundwater contamination.

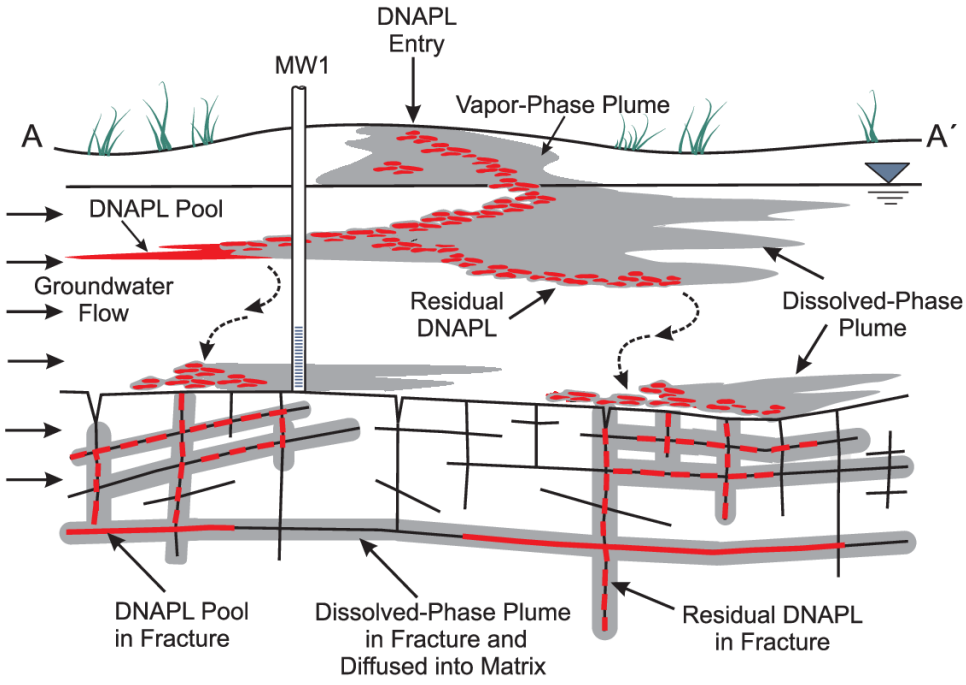

Figure 2-1: DNAPL distribution in unconsolidated deposits (Kueper and Davies., 2009). This figure illistrates the complex flowpath of DNAPL in heterogenous soil and fractured bedrock.

Figure 2-2 illistrates residual DNAPL in a saturated porous media. The residual DNAPL forms blobs of ganglia that are disconnected from eachother (Kueper et al., 2004). In porous media satuated with water, DNAPL is often the non-wetting fluid on the soil grains. This means that in order for the DNAPL to migrate, the DNAPL has to overcome the capillary forces to displace that water. The capillary forces are a function of the pore geometry, interfacial tension, and contact angle (NRC, 2005). In Figure 2-2, the residual DNAPL can be seen as the wetting fluid on the soils grains with respect to the water.

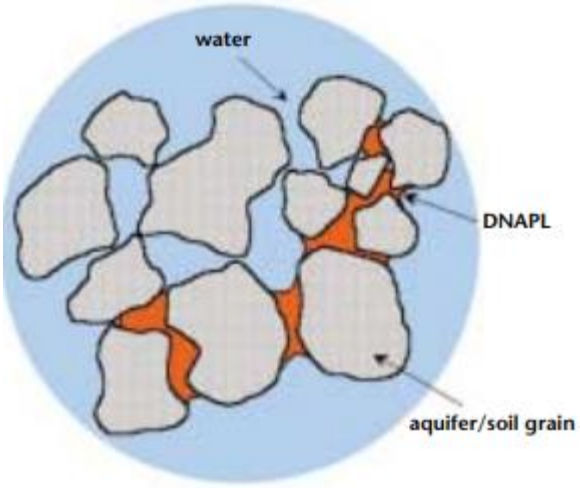

Figure 2-2: Residual DNAPL in a saturated porous media (Kueper et al., 2004). This figure illistrates DNAPL as the wetting fluid that has overcome the capillary forces to displace the water on the soil grains.

2.1.3 DNAPL Remediation

Remediation of sites contaminated with DNAPLs continue to be a major environmental challenge (Yang et al., 2022). Over the past two decades, the amount of information on DNAPL source zone depletion technologies have grown significantly. Examples of these technologies include thermal technologies such as thermal desorption (e.g., Vidonsih et al., 2016), in-situ surfactant and cosolvent flushing which increase DNAPL mobilization for extraction (e.g., Saenton and Illangasekare, 2013), and smoldering combustion which ignite a smoldering and combustion reaction to propagate through contaminated soil (e.g., Pironi et al., 2009). Large quantities of DNAPL have been proven to be removed from source zones using these technologies, with the magnitude of the removal being highly dependent on a site's heterogeneity, as well as technology specific factors (Zhang et al., 2008). Even if only partial DNAPL source zone depletion is achieved, benefits such as eliminating DNAPL mobility and reduction of the DNAPL mass depletion rate can benefit the local environmental conditions (Kavanaugh et al., 2003).

It is also very important to characterize the DNAPL contaminated site before implementing the appropriate remediation technology (Guo et al., 2021). For example, in-situ chemical oxidation requires accurate estimates of the source zone mass, location, and geometry, and

the matrix oxygen demand. Otherwise, the magnitude of the DNAPL source zone depletion will be negatively impacted (NRC, 2005).

2.2 DNAPL Source Zone Characterization

2.2.1 Introduction

The complex migration and heterogenous distribution of DNAPL in the subsurface described in the previous literature review section indicates the difficulty of accurately determining the location of DNAPL source zones. However, accurate characterization of DNAPL source zones in the subsurface is necessary for determining the appropriate remediation strategy for a contaminated site (Soga et al., 2004). Studies have been completed that discuss multiple DNAPL characterization methods and their advantages and disadvantages (e.g., Kram et al., 2001; NRC, 2005; Basu et al., 2009).

2.2.2 Invasive Techniques

Traditional techniques for characterizing the location of DNAPL source zones are typically invasive. These techniques disturb the subsurface and can potentially disturb the location of the DNAPL source zone distribution. Papers have studied the effectiveness of some of these techniques including core sampling, trial pits, direct push technologies such as TarGOST laser-induced fluorescence (Okin et al., 2006), and monitoring wells (e.g., Griffin and Watson, 2002; Kueper et al., 2004; McMillan et al., 2018). Although many of these techniques are commonly implemented on contaminated sites, they suffer from major limitations such as poor sampling density that is widely spaced (Kueper et al., 2004). This limitation is a major issue because it restricts accurate characterization of the DNAPL source zone which is required to determine the appropriate remediation strategy (Chambers et al., 2010). Other limitations include the techniques being costly and time-consuming (Griffin and Watson, 2002).

2.2.3 Non-Invasive Techniques

Research regarding non-invasive geophysical techniques used for characterizing the subsurface has advanced significantly in recent years. Non-invasive techniques typically have the advantage of being spatially continuous and therefore gather subsurface data over

a much larger domain then invasive techniques (e.g., Brewster et al., 1995; Revil et al., 2012; Loke et al., 2013). DNAPLs are generally more electrically resistive then groundwater and can be measured as distinct targets in the pore space of the subsurface in comparison to groundwater (Lucius et al., 1992). The contrast of electrical resistivity between DNAPLs and groundwater allows for the utilization of non-invasive geoelectrical techniques for characterizing DNAPL source zones. Geoelectrical techniques such as electrical resistivity tomography (ERT), induced polarization (IP) and ground penetrating radar (GPR) have become increasingly popular in recent years and have been used across a wide range of hydrogeological investigations (e.g., Zhou et al., 2001; Loke et al., 2013; Binley e t al., 2015; Deng et al., 2017; Trento et al., 2021; Zou et al., 2022;).

2.3 Electrical Resistivity Tomography

2.3.1 Introduction

Electrical resistivity tomography (ERT) is one of the most common and long-standing geophysical surveying methods (Loke et al., 2013). The purpose of these surveys is to measure the variation of electrical resistivity in the subsurface. The ground resistivity is related to various geological parameters such as fluid and mineral content, porosity, and degree of water saturation (Deng et al., 2017). ERT has advanced significantly over the years with improved instruments, speed and quality of data acquisition, and better data processing and inversion programs (e.g., Stummer et al., 2004; Ogilvy et al., 2009; Boyd et al., 2019). ERT is being widely applied in geotechnical, hydrogeological, mining, and environmental applications (e.g., Al-Heety et al., 2021; Moreira et al., 2021; Mendoza et al., 2021).

2.3.2 Basic Resistivity Theory

The flow of electrical current into the ground is governed by Ohm's Law. In vector form, Ohm's Law for current flow into a continuous medium is governed by (Tsourlos, 1995):

$$J = \sigma E \tag{2.1}$$

where J is the current density, σ is the conductivity of the medium, and E is the electric field intensity. However, geophysical surveys in the field generally measure electric field

potential Φ. The relationship between electric field potential and the electric field intensity is governed by:

$$E = -\nabla\Phi \tag{2.2}$$

Combining equations 2.1 and 2.2:

$$J = -\sigma\nabla\Phi \tag{2.3}$$

2.3.3 ERT Data Acquisition

ERT data acquisition involves injecting current into the subsurface using point electrodes. The potential difference is measured at other monitoring electrodes within the current flow area. Figure 2-3 depicts a current source from a single electrode on the ground surface assuming uniform resistivity throughout the subsurface.

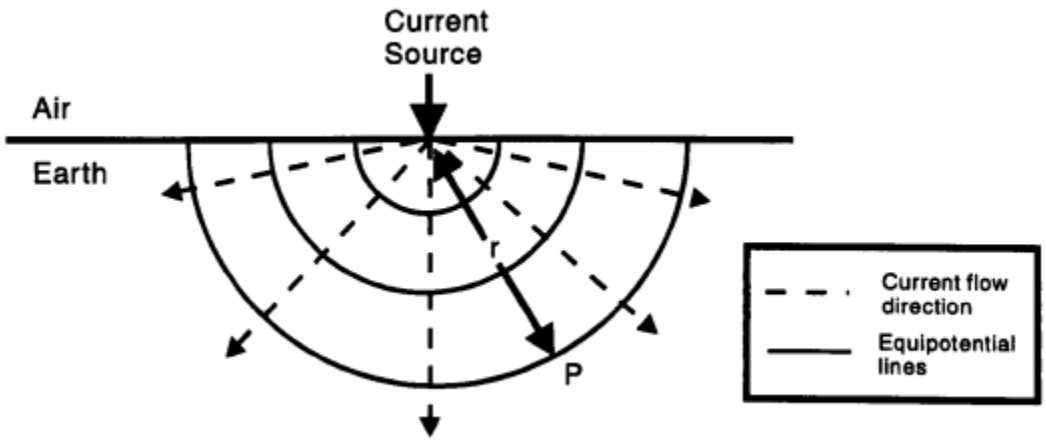

Figure 2-3: The equipotential surfaces and the directions of the current from one point source electrode (Tsourlos, 1995).

The current source *I* travels in all directions along the subsurface radius creating a hemispherical distribution of resistivity ρ assuming the subsurface is homogenous. At a distance *r* from the current source, the surface area of the hemisphere is $2\pi r^2$, so the electric field potential at point P is given by (Tsourlos, 1995):

$$\Phi_P = \frac{I\rho}{2\mathrm{pr}} \tag{2.4}$$

Geophysical surveys utilize at least one positive and one negative current electrode. Figure 2-4 depicts the positive electrode A injecting a current (source) into the ground and the negative electrode B collecting the current (sink).

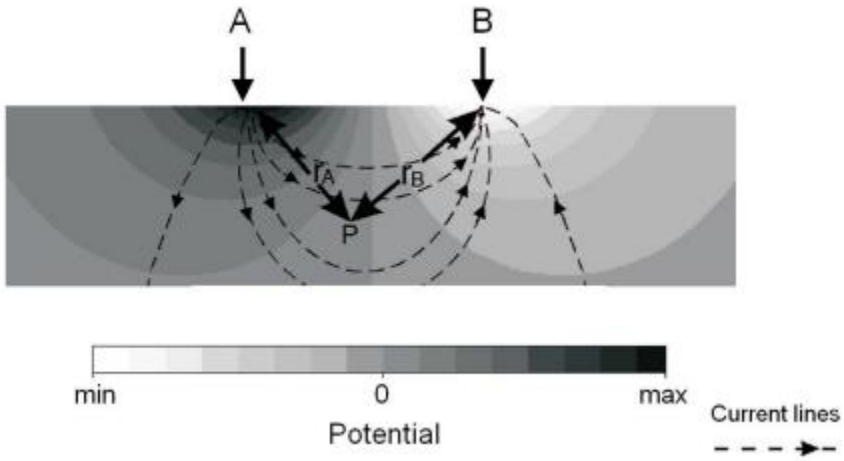

Figure 2-4: Current lines and equipotential surfaces from two point source electrodes (Power et al., 2014).

The electric field potential at point P, distance r_A from source electrode A and distance r_B from sink electrode B is:

$$\Phi_P = \frac{I\rho}{2\mathrm{p}}\left(\frac{1}{r_A} - \frac{1}{r_B}\right) \tag{2.5}$$

Generally, two pairs of electrodes are utilized for ERT surveys. Two current electrodes, A and B, inject current *I* into the subsurface, and two potential electrodes, M and N, measure the potential voltage. Figure 2-5 depicts a four-electrode setup using current electrodes A, B and potential electrodes M, N assuming a homogenous subsurface.

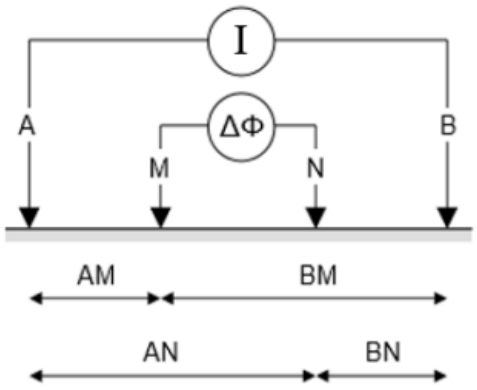

Figure 2-5: A four-electrode array with current electrodes A, B and potential electrodes M, N (Power el al., 2014).

The electric potential at M and N can be measured using equation:

$$\Phi_M = \frac{I\rho}{2\mathrm{p}}\left(\frac{1}{AM} - \frac{1}{BM}\right) \tag{2.6}$$

$$\Phi_N = \frac{I\rho}{2\mathrm{p}}\left(\frac{1}{AN} - \frac{1}{BN}\right) \tag{2.7}$$

The potential difference is therefore:

$$\Delta\Phi = \Phi_M - \Phi_N = \frac{I\rho}{2\mathrm{p}}\left(\frac{1}{AM} - \frac{1}{BM} - \frac{1}{AN} + \frac{1}{BN}\right) \tag{2.8}$$

This equation assumes that the subsurface is homogenous and isotropic, but in the field, it is understood that the subsurface is heterogenous. The observed resistivity values are therefore considered 'apparent'. The apparent resistivity value is not the true resistivity value of the subsurface and can be described as the weighted average resistivity of the subsurface. The apparent resistivity is:

$$\rho_a = G_f\left(\frac{\Delta\Phi}{\mathrm{I}}\right) \tag{2.9}$$

where G_f is the geometric factor that is dependent on the current and potential electrode sequence and is determined using:

$$G_f = 2\mathrm{p} \,/\, \left(\frac{1}{AM} - \frac{1}{BM} - \frac{1}{AN} + \frac{1}{BN}\right) \tag{2.10}$$

Many electrode sequences exist and will be discussed in section 2.3.4.

2.3.4 Electrode Sequences

Since the 1950's, many different electrode sequences have been utilized when gathering ERT data. Each electrode array has its own advantages and limitations. These include different sensitivities with respect to lateral and vertical resistivity variation, depth of investigation, and signal-to-noise ratios (Dahlin and Zhou, 2004). The type of electrode arrangement also corresponds to the geometric factor. Figure 2-6 depicts some of the most common electrode array types including the location of the current and potential electrodes, and the specific geometric factor (Loke, 2013).

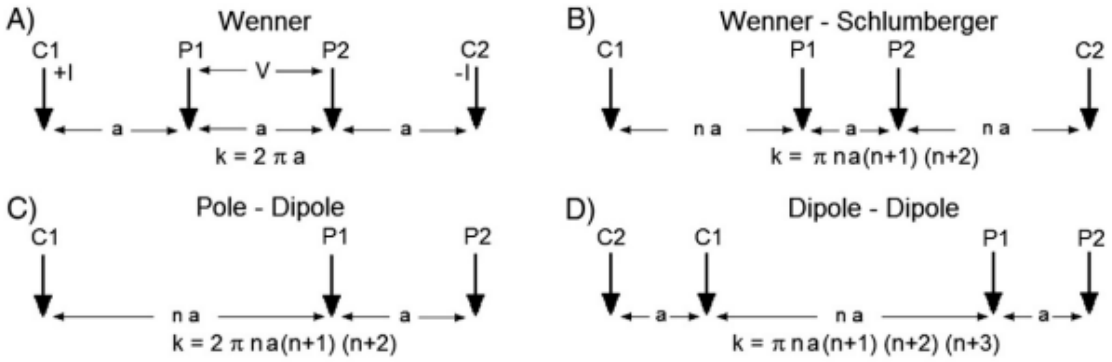

Figure 2-6: Common electrode array types and geometric factors (Loke et al., 2013)

Many studies have been done to determine which electrode array type is optimal for resolving specific targets of interest. Dahlin and Zhou (2004) conducted a study where ten different electrode arrays were used, including the ones seen in Figure 2-6, to classify 4 different subsurface scenarios. The results included a detailed list of the advantages and limitations of each array studied such as the dipole-dipole and wenner-schlumberger arrays. The dipole-dipole array was noted to have accurate vertical and horizontal resolving ability but is more sensitive to noise in comparison to other arrays. And the wenner-schumberger array is less sensitive to noise but had a lower accuracy for mapping horizontal subsurface changes and was only able to characterize vertical changes.

Bing and Greenhalgh (2000) conducted a cross-hole ERT study in which electrodes were placed in vertical boreholes as seen in Figure 2-7. This study looked at multiple electrode

arrays constructed in vertical boreholes. These results discussed the advantages and disadvantages of each cross-hole configuration.

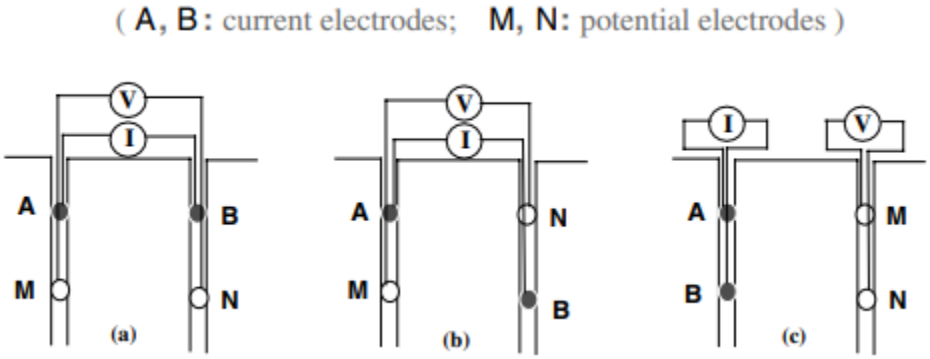

Figure 2-7: Cross-hole bipole-bipole array using various current and potential electrode configurations (Bing and Greenhalgh, 2000)

2.3.5 Electrode Configurations

Surface ERT Arrays

ERT surveys can be classified based on the horizontal and vertical placement of the electrodes. The most common ERT survey done for geophysical investigations is surface ERT where electrodes are only placed upon the ground surface (e.g., Forquet and French, 2012; von Bülow et al., 2021; Mohammed Nazifi et al., 2022). Surface ERT has the advantage of being very practical to implement and being non-invasive. However, surface ERT loses resolution with depth making it difficult to characterize subsurface conditions farther from the surface (Folch et al., 2020; Wang et al., 2020).

Vertical ERT Arrays

To rectify this issue, cross-hole ERT (e.g., Chambers et al. 2010; Wang et al., 2020; Almpanis et al., 2021b) and surface ERT can be coupled. As mentioned previously, cross-hole ERT involves placing electrodes in vertical boreholes to increase resolution with depth. However, cross-hole ERT can often be expensive due to the number of boreholes needed to achieve a large spatial coverage (Chambers et al. 2010). Drilling vertical

boreholes can also potentially remobilize DNAPL by creating new preferential pathways (Cohen and Mercer, 1993)

Horizontal ERT Arrays

Horizontal boreholes and directional drilling are becoming more popularized in the field (e.g. Duan et al., 2022; Lan et al, 2022). Specifically, at DNAPL sites, horizontal remediation wells have been applied for soil vapor extraction, air sparging, bioremediation, and horizontal soil sampling (e.g., van Heest et al., 2013; Moran and Losonsky, 2008; Bortone et al., 2020). Even though horizontal boreholes are more expensive to install on a DNAPL site than vertical boreholes, horizontal boreholes can be utilized more efficiently when comparing spatial coverage (Van Heest, 2013). This can be applied to ERT with respect to the placement of electrodes. As mentioned previously, cross-hole ERT can require many vertical boreholes to gather a large special coverage with depth (Chambers et al. 2010), versus the placement of electrodes in horizontal boreholes could significantly reduce the number of boreholes required to gather the same spatial coverage

Studies like Danielsen and Dahlin (2010) have investigated horizontal borehole ERT to determine geological conditions that could be encountered by tunnel bore machines. Simyrdanis et al. (2015) studied surface-to-tunnel ERT and examined various targets with different electrode array types. From his work he determined that the pole-tripole array type was the most effective in characterizing targets in the subsurface using surface-to-tunnel ERT.

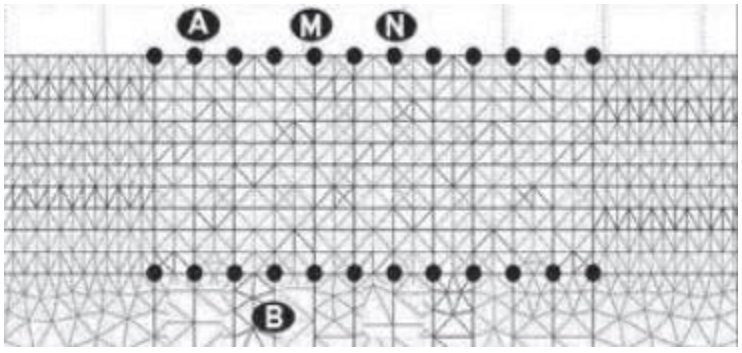

Figure 2-8: Surface-to-tunnel ERT using the pole-tripole array (Simyrdanis, 2015)

Power et al. (2015) discusses a novel surface-to-horizontal borehole (S2HB) configuration of electrodes for the monitoring of DNAPLs in two-dimensions. The S2HB ERT arrangement consists of electrodes located on the ground surface and in a horizontal borehole. This study compared surface ERT to S2HB ERT to demonstrate that S2HB ERT can provide a significant improvement to surface ERT monitoring, specifically when monitoring DNAPLs at depth. During this study, a field scale DNAPL remediation scenario was simulated using surface ERT and S2HB ERT to establish the potential for S2HB ERT. A laboratory experiment was then performed to further demonstrate the improvement from surface ERT to S2HB ERT. In conclusion, this work demonstrated the potential of improved DNAPL mapping by utilizing S2HB ERT, however it was limited to two dimensions. This is a particular limitation for DNAPL mapping due to the complex and highly heterogenous nature of DNAPL source zones.

2.3.6 ERT Data Processing

Forward Models

ERT investigations are becoming increasingly popular in geotechnical, hydrogeological, mining, and environmental settings (e.g., Al-Heety et al., 2021; Moreira et al., 2021; Mendoza et al., 2021). Surveys of these settings can be simulated using numerical models called forward models. Forward models allow for a wide variety of scenarios to be tested. Features such as the subsurface background and resistivities can be defined, as well as the corresponding geometries (Blanchy et al., 2020). Forward model simulations can therefore help determine appropriate ERT arrangements to be applied to a DNAPL site to characterize a desired area or target.

The forward modeling problem which determines the potential over a given subsurface structure can begin to be expressed by examining Equation 2.3 (i.e., $J = -\sigma \nabla \Phi$). This equation can be further expressed as a relationship between the current density and the current over an elemental volume ∇V surrounding a current source I_c located at (x_s, y_s, z_s) given by (Dey and Morrison, 1979):

$$\nabla J_c = \left(\frac{I}{\nabla V}\right) \partial(x - x_s) \partial(y - y_s) \partial(z - z_s) \qquad 2.11$$

where ∂ is the Dirac delta function. Equation 2.11 can then be rewritten as:

$$-\nabla \cdot [\, \sigma(x,y,z)\nabla\Phi(x,y,z)] = (\frac{I}{\nabla V})\partial(x-x_s)\partial(y-y_s)\partial(z-z_s) \qquad 2.12$$

This partial differential equation defines the subsurface potential distribution under isotropic conditions for a non-uniform 3D medium from a point current source. Forward modeling attempts to solve this equation and many techniques have been created to find a solution. Generally, finite difference and finite element methods are considered the most viable methods because they allow for modeling large, complex, and arbitrary subsurface resistivity conditions (Tsourlos, 1995). For these methods, the subsurface is generally characterized into a mesh and split into small volumes, in which the resistivity can be specified. The potential difference can then be calculated for nodes of the mesh (Dey and Morrison, 1979).

Inversion

Inversion involves determining the subsurface resistivity distribution that explains the apparent resistivity measurements to an acceptable degree. Traditionally, independent inversion, in which ERT data recorded at different times is inverted independently of any other information has been implemented (e.g., Tsourlos et al., 2003; Kim et al., 2009). A popular independent inversion method is the L_2-norm inversion scheme that involves minimizing the L_2-norm of the following objective function, *S*:

$$S = \Phi_d + \lambda\Phi_m = |D - G(X)|^2 + \lambda^2 |CX|^2 \qquad (2.13)$$

In this equation, Φ_d is the data misfit vector, Φ_m is a regularization function, λ is the Lagrangian multiplier that is used for the regularization term, *X* represents the subsurface model from the inversion procedure, *D* is the recorded ERT data, *G* is the forward operator, and *C* is the spatial second-derivative operator. The first term on the right side of the Equation (2.11) ensures convergence of the inverted model generated with respect to the recorded data. The second term is used to stabilize the inversion algorithm and produce smooth inverted models that satisfy the data (Constable et al., 1987). The solution to this

objective function in which the solution is minimized can be found using an iterative Gauss-Newton algorithm. The iterative normal equation produced is:

$$X_{i+1} = X_i + dX = X_i + (J^T J + \lambda C^T C)^{-1} J^T (D - G(X)) \quad (2.14)$$

Where *i* denotes the iteration number, *dX* is the perturbation to the updated model, and *J* is the Jacobian or sensitivity matrix (i.e., derivatives of the recorded data with respect to changes in the model parameters).

In recent years, other inversion approaches have been developed, particularly for time-lapse monitoring surveys containing multiple time-steps. Background difference inversion is for inversion on the differences between the background and subsequent data sets. The resistivity obtained by the inversion of background data serves as a priori model in the difference inversion (LaBrecque and Yang, 2001). Four-dimensional (4D) time-lapse inversion algorithms (e.g., Kim et al., 2009; Karaoulis et al., 2014a; Loke et al., 2014) have been developed in recent years that involve defining the entire subsurface model in a space-time domain and inverting the datasets from different times simultaneously. Regularizations are utilized for the space and time domains to reduce artefacting (Kim et al., 2009) and improve sensitivity in regions of changed resistivities (Karaoulis et al., 2011a). Inversion artifacts are false resistivity measurements that can masks real resistivity changes or suggest subsurface changes that didn't occur. They are created from noise in ERT measurements. Specifically, methods such as the 4D active time constraint (4D-ATC) method introduced by Karaoulis et al. (2011a), vary the time-domain Lagrangian proportionally between measurements at different times (i.e., areas with significant changes are assigned low time regularization values and areas without significant changes are assigned high time regularization values). The 4D-ATC approach has also been applied in many geophysical studies (e.g., Karaoulis et al., 2012; Karaoulis et al., 2011b; Karaoulis et al., 2014b).

ResIPy

In the field, ERT data is relatively straight forward to collect, but data processing can be a major challenge. Advanced modeling codes such as IP4DI are available but require an

extensive knowledge of geophysics and coding to be used effectively (Karaoulis, 2013). Other inversion codes exist such as Res2DInv, DCPro and ERTLab; however, these codes are commercial and costly.

ResIPy is an open source and user-friendly software that can be used to effectively process geophysical data (Blanchy et al., 2020). The ResIPy software is based on inversion codes R2, cR2, R3t, and cR3t. Capabilities of ResIPy include processing 2D and 3D datasets, processing data at multiple time-steps, and the input of complex topography (Boyd et al., 2019).

As shown in Figure 2-9, ResIPy utilizes a modern tabbed format to take the user through each step of geophysical data processing including data filtering, mesh generation, inversion, and visualization (Boyd et al., 2019). Visualization of the data can be seen in Figure 2-10 which depicts the high-quality images outputted by the software.

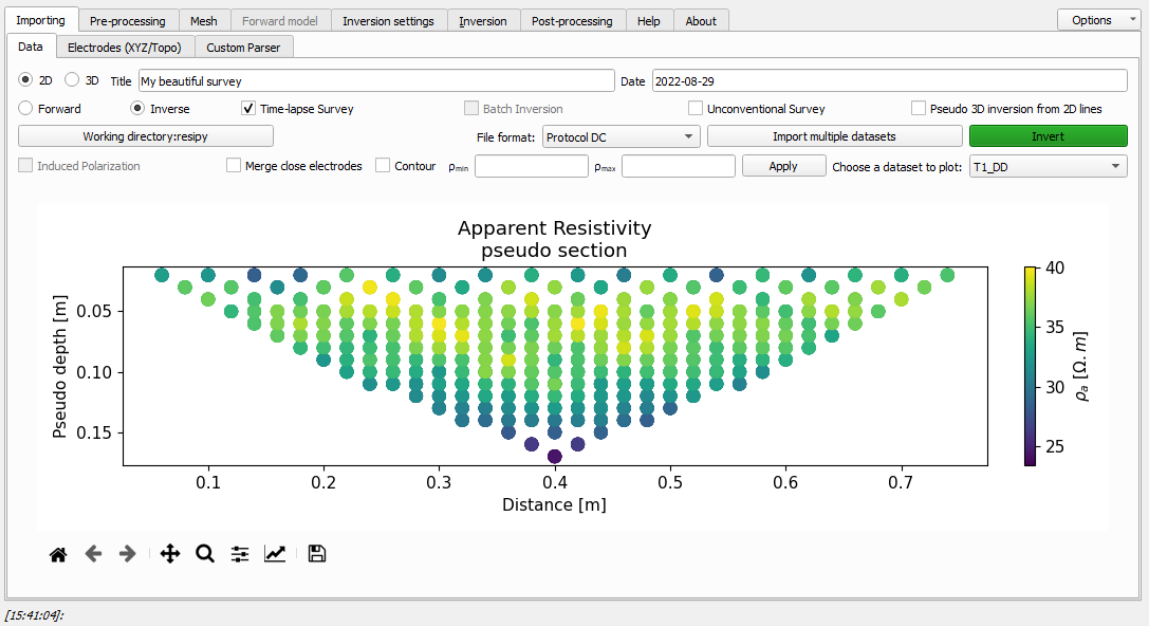

Figure 2-9: Data importing tab on the ResIPy Graphical Use Interphase.

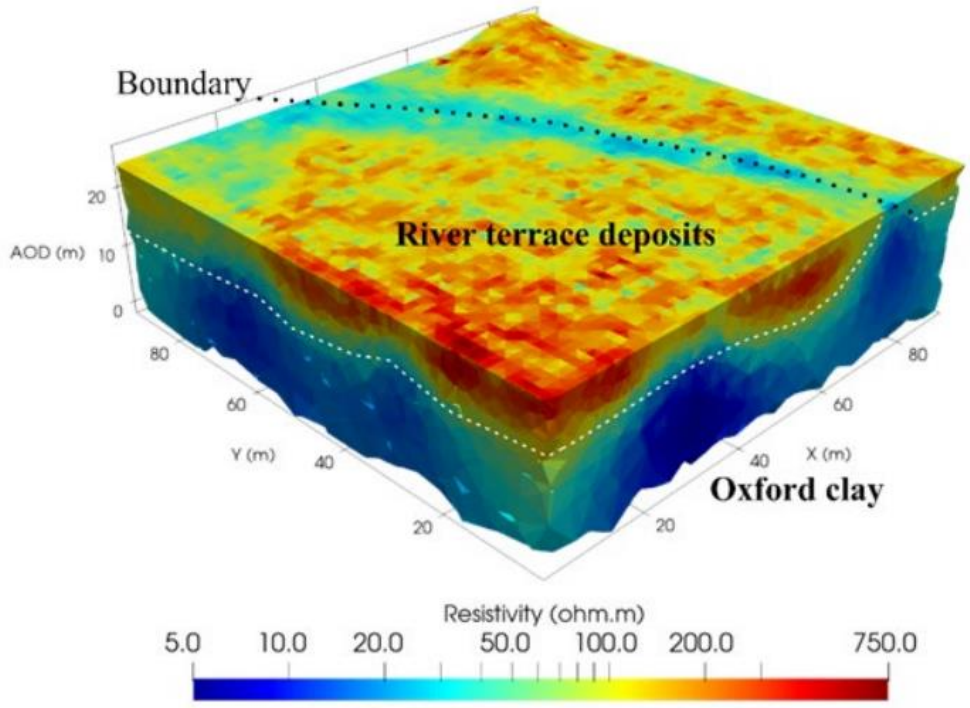

Figure 2-10: Inverted three-dimensional volume using ResIPy (Boyd et al., 2019).

ResIPy can generate synthetic data and process geophysical data using a variety of electrode arrangements for a desired amount of time-steps (Blanchy et al., 2020). This can be applied for simulating a wide variety of scenarios in which a DNAPL source zone is present in the subsurface, and for taking measurements at several times with various electrode configurations. ResIPy's synthetic data generation utilizes a meshing system in which the subsurface is broken down into small volumes specified by the size of the mesh. These volumes can be selected on the graphical user interphase with an interactive volume selector. The resistivity of the specific volumes selected can then be defined. This process can be repeated to create subsurface conditions over multiple time-steps and to simulate a wide variety of subsurface scenarios. Once the subsurface scenarios have been generated, the synthetic subsurface data can be gathered using the electrode sequence corresponding to the desired electrode arrangement.

After the subsurface data has been gathered for all desired time-steps, the results can be inverted. To invert the results, ResIPy requires importing of the gathered data for all desired time-steps (including the electrode locations), selection of the mesh size, and the selection

of numerous inversion settings including inversion type and maximum number of iterations (Boyd et al., 2019). After these steps have been completed, ResIPy can invert the subsurface data. During inversion, ResIPy will estimate the subsurface conditions, and determine the apparent resistivity of the estimated conditions. Iterations will occur by comparing the estimated and measured apparent resistivities until they are within a desired range of each other or until the maximum number of iterations defined has been reached (Blanchy et al., 2020).

2.4 References

Almpanis, A., Tsourlos, P., Vargemezis, G. and Papazachos, C. (2021), Application of crosshole electrical resistivity tomography measurements under the influence of horizontally slotted plastic cased boreholes. Near Surface Geophysics, 20: 46-63. https://doi.org/10.1002/nsg.12187

Al-Heety, A. J. R., Hassouneh, M., & Abdullah, F. M. (2021). Application of MASW and ERT methods for geotechnical site characterization: A case study for roads construction and infrastructure assessment in Abu Dhabi, UAE. *Journal of Applied Geophysics*, *193*. https://doi.org/10.1016/j.jappgeo.2021.104408

Basu, N. B., Suresh, P., Rao, C., Poyer, I. C., Nandy, S., Mallavarapu, M., Naidu, R., Davis, G. B., Patterson, B. M., Annable, M. D., & Hatfield, K. (2009). Integration of traditional and innovative characterization techniques for flux-based assessment of Dense Non-aqueous Phase Liquid (DNAPL) sites. *Journal of Contaminant Hydrology*, *105*(3–4), 161–172. https://doi.org/10.1016/j.jconhyd.2008.12.005

Bing, Z., & Greenhalgh, S. A. (2000). Cross-hole resistivity tomography using different electrode configurations. In *Geophysical Prospecting* (Vol. 48).

Binley, A., Hubbard, S., Huisman, J., Revil, A., Robinson, D., Singha, K., & Slater, L. (2015). The emergence of hydrogeophysics for improved understanding of subsurface processes over multiple scales _ Enhanced Reader. *Water Resources Reseach*, *51*.

Blanchy, G., Saneiyan, S., Boyd, J., McLachlan, P., & Binley, A. (2020). ResIPy, an intuitive open source software for complex geoelectrical inversion/modeling. *Computers and Geosciences*, *137*. https://doi.org/10.1016/j.cageo.2020.104423

Bortone, I., Erto, A., Nardo, A. di, Santonastaso, G. F., Chianese, S., & Musmarra, D. (2020). Pump-and-treat configurations with vertical and horizontal wells to remediate an aquifer contaminated by hexavalent chromium. *Journal of Contaminant Hydrology*, *235*. https://doi.org/10.1016/j.jconhyd.2020.103725

Boyd, J., Saneiyan, S., & Mclachlan, P. (2019). *3D Geoelectrical Problems With ResiPy, an Open Source Graphical User Interface for Geoelectrical Data Processing*. https://doi.org/10.13140/RG.2.2.35381.63205

Brewster, M., Annan, A., Greenhouse, J., Kueper, B., Olhoeft, G., Redman, J., & Sander, K. (1995). *Observed Migration of a Controlled DNAPL Release by Geophysical Methods*.

Chambers, J. E., Wilkinson, P. B., Wealthall, G. P., Loke, M. H., Dearden, R., Wilson, R., Allen, D., & Ogilvy, R. D. (2010a). Hydrogeophysical imaging of deposit heterogeneity and groundwater chemistry changes during DNAPL source zone bioremediation. *Journal of Contaminant Hydrology*, *118*(1–2), 43–61. https://doi.org/10.1016/j.jconhyd.2010.07.001

Constable, S., R. Parker, C. Constable. 1987. Occam's inversion: a practical algorithm for generating smooth models from electromagnetic sounding data. Geophysics, 52:289-300.

Cohen, R., & Mercer, J. (1993). DNAPL Site Evaluation. *GeoTrans, Inc.*

Dahlin, T., & Zhou, B. (2004). A numerical comparison of 2D resistivity imaging with 10 electrode arrays. *Geophysical Prospecting*, *52*(5), 379–398. https://doi.org/10.1111/j.1365-2478.2004.00423.x

Danielsen, B. E., & Dahlin, T. (2010). Numerical modeling of resolution and sensitivity of ERT in horizontal boreholes. *Journal of Applied Geophysics*, *70*(3), 245–254. https://doi.org/10.1016/j.jappgeo.2010.01.005

Deng, Y., Shi, X., Xu, H., Sun, Y., Wu, J., & Revil, A. (2017). Quantitative assessment of electrical resistivity tomography for monitoring DNAPLs migration – Comparison with high-resolution light transmission visualization in laboratory sandbox. *Journal of Hydrology*, *544*, 254–266. https://doi.org/10.1016/j.jhydrol.2016.11.036

Dey, A., and H.F. Morrison. 1979. Resistivity modeling for arbitrarily shaped three-dimensional structures. Geophysics, 44: 753-780.

Duan, H., Wang, Y., Xiao, Q., Wang, J., & Peng, D. (2022). Gas extraction technology and application of near horizontal high directional drilling. *Energy Reports*, *8*, 1326–1333. https://doi.org/10.1016/j.egyr.2022.02.051

Folch, A., del Val, L., Luquot, L., Martínez-Pérez, L., Bellmunt, F., le Lay, H., Rodellas, V., Ferrer, N., Palacios, A., Fernández, S., Marazuela, M. A., Diego-Feliu, M., Pool, M., Goyetche, T., Ledo, J., Pezard, P., Bour, O., Queralt, P., Marcuello, A., … Carrera, J. (2020). Combining fiber optic DTS, cross-hole ERT and time-lapse induction logging to characterize and monitor a coastal aquifer. *Journal of Hydrology*, *588*. https://doi.org/10.1016/j.jhydrol.2020.125050

Forquet, N., & French, H. K. (2012). Application of 2D surface ERT to on-site wastewater treatment survey. *Journal of Applied Geophysics*, *80*, 144–150. https://doi.org/10.1016/j.jappgeo.2012.02.002

Griffin, T., & Watson, K. (2002). *A Comparison of Field Techniques for Confirming Dense Nonaqueous Phase Liquids*.

Guo, Q., Shi, X., Kang, X., Hao, S., Liu, L., & Wu, J. (2021). Evaluation of the benefits of improved permeability estimation on high-resolution characterization of DNAPL distribution in aquifers with low-permeability lenses. *Journal of Hydrology*, *603*. https://doi.org/10.1016/j.jhydrol.2021.126955

Karaoglu, A. G., Copty, N. K., Akyol, N. H., Kilavuz, S. A., & Babaei, M. (2019). Experiments and sensitivity coefficients analysis for multiphase flow model calibration of enhanced DNAPL dissolution. *Journal of Contaminant Hydrology*, *225*. https://doi.org/10.1016/j.jconhyd.2019.103515

Karaoulis, M., A. Revil, D.D. Werkema, B.J. Minsley, W.F. Woodruff, and A. Kemna. 2011b. Time-lapse three-dimensional inversion of complex conductivity data using an active time constrained (ATC) approach. Geophysical Journal International, 187: 237-251.

Karaoulis, M., A. Revil, J. Zhang, and D.D. Werkema. 2012. Time-lapse joint inversion of crosswell DC resistivity and seismic data: A numerical investigation. Geophysics, 77(4): D141-D157.

Karaoulis, M., A. Revil, P. Tsourlos, D.D. Werkema, and B.J. Minsley. 2013. IP4DI: A software for time-lapse 2D/3D DC-resistivity and induced polarization tomography. Computers & Geosciences, 54(0): 164-170.

Karaoulis, M., A. Revil, B. Minsley, M. Todesco, J. Zhang, and D.D. Werkema. 2014b. Time-lapse gravity inversion with active time constraint. Geophysical JournalInternational, 196(2): 867-884.

Kavanaugh, M.C., P.S.C. Rao, L. Abriola, C. Newell, J. Cherry, T. Sale, G. Destouni, S. Shoemaker, R. Falta, R. Siegrist, D. Major, G. Teutsch, J. Mercer, and K. Udell. (2003). The DNAPL remediation challenge: is there a case for source depletion?. US Environmental Protection Agency, Washington DC.

Kim, J.H., M.J. Yi, S.G. Park, and J.G. Kim. 2009. 4-D inversion of DC resistivity monitoring data acquired over a dynamically changing earth model. Journal of Applied Geophysics, 68: 522-532.

Koohbor, B., Deparis, J., Leroy, P., Ataie-Ashtiani, B., Davarzani, H., & Colombano, S. (2022). DNAPL flow and complex electrical resistivity evolution in saturated porous media: A coupled numerical simulation. *Journal of Contaminant Hydrology*, *248*. https://doi.org/10.1016/j.jconhyd.2022.104003

Kram, M. L., Keller, A. A., Rossabi, J., & Everett, L. G. (2001). *DNAPL Characterization Methods and Approaches, Part 1: Performance Comparisons*.

Kueper, B., & Davies, K. (2009). *Asessment and Delineation of DNAPL Source Zones at Hazardous Waste Sites*.

Kueper, B. H., & Great Britain. Environment Agency. (2004). *An illustrated handbook of DNAPL transport and fate in the subsurface*. Environment Agency.

LaBrecque, D., and Yang, X. (2001), "Difference Inversion of ERT Data: a Fast Inversion Method for 3-D In Situ Monitoring," Journal of Environmental and Engineering Geophysics 6: 83-89.

Lan, H., & Moore, I. D. (2022). New design equation for maximum allowable mud pressure in sand during horizontal Directional drilling. *Tunnelling and Underground Space Technology*, *126*. https://doi.org/10.1016/j.tust.2022.104543

Loke, M. H. (2013). Tutorial : 2-D and 3-D electrical imaging surveys. www.geotomosoft.com

Loke, M. H., Chambers, J. E., Rucker, D. F., Kuras, O., & Wilkinson, P. B. (2013). Recent developments in the direct-current geoelectrical imaging method. *Journal of Applied Geophysics*, *95*, 135–156. https://doi.org/10.1016/j.jappgeo.2013.02.017

Lucius1, J. E., Olhoeft1, G. R., Hill1, P. L., & Duke2, S. K. (1992). *PROPERTIES AND HAZARDS OF 108 SELECTED SUBSTANCES-1992 EDITION*.

McMillan, L. A., Rivett, M. O., Wealthall, G. P., Zeeb, P., & Dumble, P. (2018). Monitoring well utility in a heterogeneous DNAPL source zone area: Insights from proximal multilevel sampler wells and sampling capture-zone modeling. *Journal of Contaminant Hydrology*, *210*, 15–30. https://doi.org/10.1016/j.jconhyd.2018.02.001

Mendoza, R., Rey, J., Martínez, J., Hidalgo, M. C., & Sandoval, S. (2021). Geophysical characterisation of geologic features with mining implications from ERT, TDEM and seismic reflection (Mining District of Linares-La Carolina, Spain). *Ore Geology Reviews*, *139*. https://doi.org/10.1016/j.oregeorev.2021.104581

Mohammed Nazifi, H., Gülen, L., Gürbüz, E., & Pekşen, E. (2022). Time-lapse electrical resistivity tomography (ERT) monitoring of used engine oil contamination in laboratory setting. *Journal of Applied Geophysics*, *197*. https://doi.org/10.1016/j.jappgeo.2022.104531

Moran, W., and G. Losonsky. 2008. Enhanced Delivery of Potassium Permanganate Using Horizontal Wells. In Proceedings of the Sixth International Conference on Remediation of Chlorinated and Recalcitrant Compounds, Monterey, California, USA, May 19-22, 2008.

Moreira, C. A., Rosolen, V., Furlan, L. M., Bovi, R. C., & Masquelin, H. (2021). Hydraulic conductivity and geophysics (ERT) to assess the aquifer recharge capacity of an inland wetland in the Brazilian Savanna. *Environmental Challenges*, *5*. https://doi.org/10.1016/j.envc.2021.100274

National Research Council (NRC). 2005. Contaminants in the Subsurface: Source Zone Assessment and Remediation. The National Academies Press, Washington D.C.

Ogilvy, R. D., Meldrum, P. I., Kuras, O., Wilkinson, P. B., Chambers, J. E., Sen, M., Pulido-Bosch, A., Gisbert, J., Jorreto, S., Frances, I., & Tsourlos, P. (2009). *Automated Monitoring of Coastal Aquifers with Electrical Resistivity Tomography*.

Okin, M., Carroll, S., Fisher, W., & St Germain, R. (2006). *Case study: confirmation of TarGOST laser-induced fluorescence DNAPL delineation with soil boring data* (Vol. 14, Issue 6).

Pan, Y., Zeng, X., Xu, H., Sun, Y., Wang, D., & Wu, J. (2020). Assessing human health risk of groundwater DNAPL contamination by quantifying the model structure uncertainty. *Journal of Hydrology, 584*. https://doi.org/10.1016/j.jhydrol.2020.124690

Pankow, J. F., & Cherry, J. A. (1996). *DENSE CHLORINATED SOLVENTS and other DNAPLs in Groundwater: History, Behavior, and Remediation*.

Pironi, P., Switzer, C., Rein, G., Fuentes, A., Gerhard, J. I., & Torero, J. L. (2009). Small-scale forward smouldering experiments for remediation of coal tar in inert media. *Proceedings of the Combustion Institute*, *32 II*, 1957–1964. https://doi.org/10.1016/j.proci.2008.06.184

Poulsen, M. M., & Kueper, B. H. (1992). *A Field Experiment To Study the Behavior of Tetrachloroethylene in Unsaturated Porous Media*. https://pubs.acs.org/sharingguidelines

Power, C., Gerhard, J. I., Karaoulis, M., Tsourlos, P., & Giannopoulos, A. (2014). Evaluating four-dimensional time-lapse electrical resistivity tomography for monitoring DNAPL source zone remediation. *Journal of Contaminant Hydrology*, *162–163*, 27–46. https://doi.org/10.1016/j.jconhyd.2014.04.004

Power, C., Gerhard, J. I., Tsourlos, P., Soupios, P., Simyrdanis, K., & Karaoulis, M. (2015). Improved time-lapse electrical resistivity tomography monitoring of dense non-aqueous phase liquids with surface-to-horizontal borehole arrays. *Journal of Applied Geophysics*, *112*, 1–13. https://doi.org/10.1016/j.jappgeo.2014.10.022

Revil, A., Karaoulis, M., Johnson, T., & Kemna, A. (2012). Review: Some low-frequency electrical methods for subsurface characterization and monitoring in hydrogeology. *Hydrogeology Journal*, *20*(4), 617–658. https://doi.org/10.1007/s10040-011-0819-x

Saenton, S., & Illangasekare, T. H. (2013). Effects of incomplete remediation of NAPL-contaminated aquifers: experimental and numerical modeling investigations. *Applied Water Science*, *3*(2), 401–414. https://doi.org/10.1007/s13201-013-0090-5

Simyrdanis, K., Tsourlos, P., Soupios, P., Tsokas, G., Kim, J. H., & Papadopoulos, N. (2015). Surface-to-tunnel electrical resistance tomography measurements. *Near Surface Geophysics*, *13*(4), 343–354. https://doi.org/10.3997/1873-0604.2015019

Soga, K., Page, J. W. E., & Illangasekare, T. H. (2004). A review of NAPL source zone remediation efficiency and the mass flux approach. *Journal of Hazardous Materials*, *110*(1–3), 13–27. https://doi.org/10.1016/j.jhazmat.2004.02.034

Stummer, P., H. Maurer, and A. Green. 2004. Experimental design: electrical resistivity data sets that provides optimum subsurface information. Geophysics, 69: 120-139.

Trento, L. M., Tsourlos, P., & Gerhard, J. I. (2021). Time-lapse electrical resistivity tomography mapping of DNAPL remediation at a STAR field site. *Journal of Applied Geophysics*, *184*. https://doi.org/10.1016/j.jappgeo.2020.104244

Tsourlos, P. (1995). *Modeling, Interpretation and Inversion of Multielectrode Resistivity Survey Data*.

Van Heest, G. 2013. Horizontal wells for groundwater remediation: How a technology that revolutionized the oil industry is used to remediate groundwater. The Magazine for Environmental Managers. Air and Waste Management Association. June 2013 Edition.

Vidonish, J. E., Zygourakis, K., Masiello, C. A., Sabadell, G., & Alvarez, P. J. J. (2016). Thermal Treatment of Hydrocarbon-Impacted Soils: A Review of Technology Innovation for Sustainable Remediation. *Engineering*, *2*(4), 426–437. https://doi.org/10.1016/J.ENG.2016.04.005

von Bülow, R., Klitzsch, N., & Wellmann, F. (2021). Strategies to overcome near surface disturbances while inverting time-lapse surface ERT data. *Journal of Applied Geophysics*, *195*. https://doi.org/10.1016/j.jappgeo.2021.104463

Wang, H., Lin, C. P., & Liu, H. C. (2020). Pitfalls and refinement of 2D cross-hole electrical resistivity tomography. *Journal of Applied Geophysics*, *181*. https://doi.org/10.1016/j.jappgeo.2020.104143

Yang, P., Guo, H., Wang, Z., & Zhao, E. (2022). Influence of distribution characteristics of residual DNAPL on mass transfer in porous media under ethanol co-solvent flushing. *Journal of Hydrology*, *610*. https://doi.org/10.1016/j.jhydrol.2022.127932

Zhang, C., Yoon, H., Werth, C. J., Valocchi, A. J., Basu, N. B., & Jawitz, J. W. (2008). Evaluation of simplified mass transfer models to simulate the impacts of source zone architecture on nonaqueous phase liquid dissolution in heterogeneous porous media. *Journal of Contaminant Hydrology*, *102*(1–2), 49–60. https://doi.org/10.1016/j.jconhyd.2008.05.007

Zhou, Q. Y., Shimada, J., & Sato, A. (2001). Three-dimensional spatial and temporal monitoring of soil water content using electrical resistivity tomography. *Water Resources Research*, *37*(2), 273–285. https://doi.org/10.1029/2000WR900284

Zou, C., & Zhang, S. (2022). Precise estimation of subsurface moisture content based on laboratory measurement and 3D GPR field survey. *Journal of Applied Geophysics*, 104752. https://doi.org/10.1016/j.jappgeo.2022.104752

Chapter 3

3 Three-Dimensional Surface-To-Horizontal Borehole Electrical Resistivity Tomography (S2HB ERT) Imaging of Dense Non-Aqueous Phase Liquids

3.1 Introduction

Sites contaminated by dense non-aqueous phase liquids (DNAPLs), including chlorinated solvents and coal tar, remains a major environmental challenge (Pankow et al., 1996). The migration and redistribution of DNAPL in the subsurface generates a highly complex and heterogeneous DNAPL zone that acts as a long-term source for contaminating groundwater and the environment over enormous areas (Karaoglu et al., 2019; Koohbor et al., 2022). To successfully remediate DNAPL-contaminated sites, accurate characterization of the subsurface is required to determine an appropriate remedial strategy (Soga et al., 2004). Furthermore, effective time-lapse monitoring is required to track the performance of the implemented remediation strategy (e.g., Chambers et al., 2010).

Most DNAPL investigations remain highly reliant on traditional methods such as monitoring wells, core sampling, and trial pits (e.g., Griffin and Watson, 2002; Kueper et al., 2004; McMillan et al., 2018). However, these methods can be laborious and costly, while also suffering from poor sampling density that provides only sparsely located point information. Furthermore, the invasiveness of these methods is particularly problematic as subsurface drilling can mobilize the contaminants through new flow pathways (Kueper et al., 2004). These limitations have motivated the longstanding desire to employ geophysical imaging techniques at contaminated field sites (e.g., Brewster et al., 1995). Geophysical techniques are non-invasive, cost-effective, and can provide rapid and continuous spatial and temporal information, thereby having the ability to image large volumes of the subsurface data over long time periods (e.g., Revil et al., 2012; Binley et al., 2015; Slater and Binley, 2021).

Of the many geophysical techniques, electrical resistivity tomography (ERT) is arguably the most widely applied, especially in the field (e.g., Loke et al., 2013; Deng et al., 2017; Zou et al., 2022). ERT measures the distribution of electrical resistivity in the subsurface,

which is in response to the variation of materials and processes, including soil type, porosity, water saturation, groundwater chemistry, and contaminants (e.g., Loke et al., 2013). The potential of ERT for mapping DNAPLs stems from the electrical contrast between insulating DNAPL and conductive groundwater that share the pore space in an aquifer (Lucius et al., 1992). However, due to the intricacy of DNAPL source zone architectures, accurate static (one-off) ERT imaging of DNAPLs remains challenging (e.g., Power et al., 2014; Cardarelli and Di Filippo, 2009), leading to greater usage in time-lapse mode for monitoring DNAPL changes over time (e.g., DNAPL mass reduction) (e.g., Dhu and Heinson, 2004; Deng et al., 2017; Trento et al., 2021).

Due to the intricacy of the DNAPL target, ongoing efforts to improve ERT imaging are welcome, including those related to instrumentation (e.g., Orlando and Renzi, 2015), data acquisition (e.g., Martorana et al., 2017), and inversion (e.g., Kim et al., 2014). For example, four-dimensional inversions have been developed (e.g., Karaoulis et al., 2013; Boyd et al., 2019) along with the implementation of deep-learning methods (e.g., Kang et al., 2020; 2021). Another avenue for enhancing ERT imaging involves the configuration of the electrodes. Surface ERT, where electrodes are only applied to the ground surface, is widely used due to its ease of deployment (e.g., Forquet and French, 2012; von Bülow et al., 2021; Mohammed Nazifi et al., 2022); however, surface ERT loses resolution with increasing depth. While some subsurface targets can still be reasonably imaged with lower resolution, the complexity of DNAPL makes deeper imaging problematic (e.g., Power et al., 2014; Folch et al., 2020; Wang et al., 2020). Electrodes have also been deployed in vertical boreholes, allowing cross-hole ERT (e.g., Wang et al., 2020; Almpanis et al., 2021b) and borehole-to-surface ERT (e.g., Tsourlos et al., 2011; Ochs et al., 2022). While these configurations have been effective, image sensitivity remains close to the boreholes, thereby requiring many boreholes (and significant effort and cost) to obtain adequate spatial coverage. Furthermore, the drilling of these boreholes can create new pathways and potentially remobilize DNAPL (Cohen and Mercer, 1993).

To overcome the limitations associated with surface ERT and cross-hole ERT, electrodes have more recently been deployed in horizontal arrays within the subsurface. ERT has been employed in tunnels for imaging geological conditions via tunnel-to-tunnel (e.g., van

Schoor and Binley, 2010; Danielsen and Dahlin, 2010) and surface-to-tunnel (e.g., Simyrdanis et al., 2015) configurations. Direct-push technology has also been used to implant (bury) electrodes along horizontal lines at depth (e.g., Kiflu et al., 2016). In terms of realistically deploying horizontal electrodes at DNAPL-contaminated sites, Power et al. (2015) suggested taking advantage of horizontal remediation wells that are being increasingly installed. Numerical and laboratory experiments were performed to demonstrate the potential of surface-to-horizontal borehole (S2HB) ERT to monitor DNAPL mass changes during remediation.

All studies demonstrated improved image resolution at depth by deploying electrodes in horizontal arrays; however, they were all performed in two-dimensions (2D) with either a single line of buried electrodes (e.g., implant electrodes; Kiflu et al., 2016) or two lines along the same cross-section (e.g., surface line directly overlying horizontal borehole line; Power et al., 2015). While some subsurface features and processes may be adequately resolved with 2D images with the assumption of uniformity in the third dimension, the high complexity and heterogeneity of DNAPL source zones requires three- dimensional (3D) imaging (Power et al., 2014). S2HB ERT in 3D exhibits strong potential to advance imaging performance for DNAPL investigations.

Considering conventional 3D configurations comprise a 2D surface grid of parallel lines, advancing S2HB ERT from 2D to 3D would suggest deploying horizontal borehole lines below every surface line. This would be highly laborious and cost-prohibitive and negate the intended benefit of 3D S2HB ERT. It is unknown whether adequate 3D imaging can still be obtained if a 2D surface grid is combined with a single horizontal borehole, and how this would compare to a more conventional configuration of 2D grids of both surface lines and underlying horizontal borehole lines.

The objective of this study is to evaluate the imaging performance of a novel 3D S2HB ERT configuration and how it will advance ERT mapping of DNAPLs. The most practical configuration for 3D S2HB ERT, where a 2D surface grid is combined with a single horizontal borehole, was extensively assessed. Numerical and laboratory tank experiments were conducted on various plastic targets in water and DNAPL migration through porous

media. The resolving ability of 3D S2HB ERT was evaluated with reference to 3D surface ERT. Comparative analysis of different configurations of 3D S2HB ERT were then assessed, with the 2D surface grid combined with a single borehole, three boreholes, and a matching grid of boreholes. This work advances the benefits of 2D S2HB ERT to introduce 3D S2HB ERT for the first time and demonstrate its improved performance of 3D DNAPL source zones.

3.2 Methodology

This section presents the methodology behind the 3D S2HB ERT numerical modeling and laboratory experiments completed. First, the various electrode configurations that are being investigated are described, along with the selection of specific target geometries that are used to examine the imaging performance of each configuration. The numerical software that comprises both the forward modeling and inversion schemes will be discussed, along with the design and completion of the laboratory experiments.

3.2.1 ERT Configurations

In this study, the initial 3D S2HB electrode configuration presented involves a 2D surface grid containing parallel lines of electrodes and a single line of electrodes in a horizontal borehole directly underlying the center of the surface grid (hereafter referred to as ‘S2HB-1BH’). For example, if 11 parallel lines exist on the surface (Lines 1 to 11), then the horizontal borehole line would be directly below the central Line 6 (see Figure 3-1). This configuration is first proposed as it would be the most practical to implement at a field site, with a single borehole ensuring ERT remains relatively non-invasive. Conventional 3D surface ERT comprises a 2D surface grid containing parallel lines of electrodes (Figure 3-1b) and will provide a reference to evaluate S2HB ERT performance.

The performance of 'S2HB-1BH’ ERT can also be compared to other 3D S2HB configurations. The most intensive S2HB configuration would consist of one horizontal borehole line directly below every surface line, as shown by the electrode layout (black circles) in Figure 3-1. This configuration, hereafter referred to as ‘S2HB-FULL’, would collect subsurface information over the largest domain; however, multiple horizontal borehole lines in parallel would be highly complex, laborious, and costly to install. Nevertheless, despite being impractical, it is included in this study as the ‘ideal’ imaging ability. A less intensive but more practical variation of 3D S2HB consists of three horizontal boreholes distributed equally below the surface electrode lines, hereafter referred to as ‘S2HB-3BH’ (Figure 3-1). While ‘S2HB-1BH’ ERT is compared to ‘S2HB-FULL’ and ‘S2HB-3BH’, its performance relative to conventional 3D surface ERT is the most significant.

3.2.2 Experimental Design

Experimental Size

The size of the experimental domain used in the study was based on the electrode spacings, number of electrodes, number of lines, and the depth between the surface and horizontal boreholes. Figure 3-1 presents a conceptual model of the experimental domain. Each survey line (borehole and surface) contained 21 electrodes with an inline spacing of 0.04 m. Eleven parallel lines were used on the surface for all ERT configurations, with an interline spacing of 0.04 m. While one borehole line (red circles) was used for S2HB-1BH, three lines (blue & red circles) and 11 lines (black, blue, and red circles) were deployed for S2HB-3BH and S2HB-FULL, respectively. The depth between surface and horizontal borehole lines is 0.24 m, which is six times the electrode spacing and lies within the imaging range proposed by Simyrdanis et al. (2015).

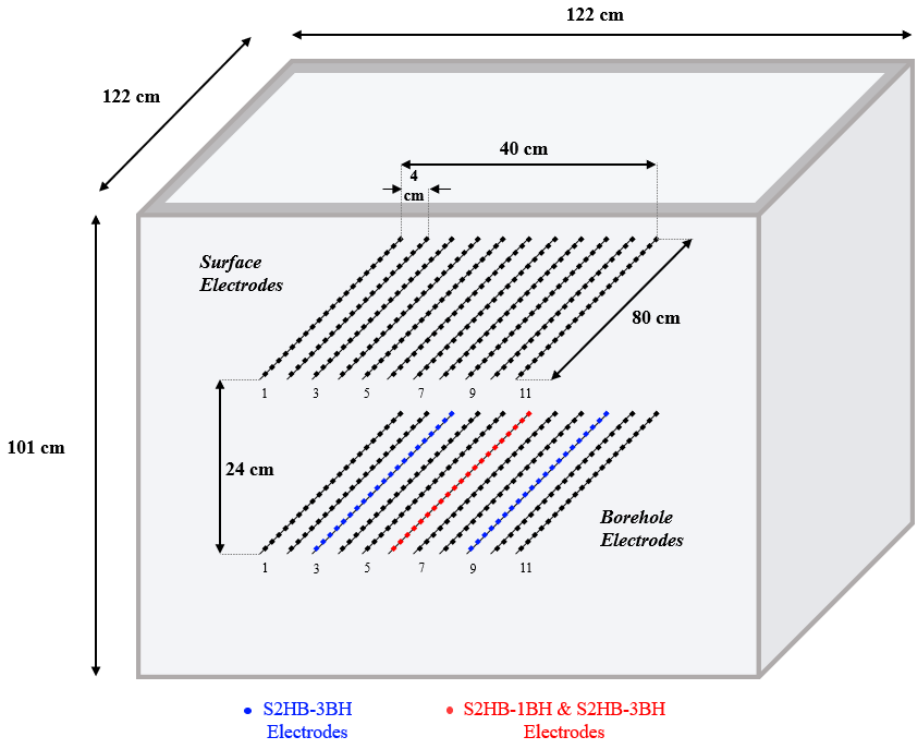

Figure 3-1: Conceptual model of the 3D experimental domain employed for this study. The outline and dimensions of the experimental tank are also included. Note that: (i) red circles indicate the single horizontal borehole in S2HB-1BH, (ii) blue circles indicate the additional two boreholes in S2HB-3BH, and (iii) black circles indicate all additional boreholes in S2HB-FULL.

Electrode Sequences

A number of electrode sequences are available for S2HB and surface configurations, including bipole-bipole, pole-tripole, multi-gradient and dipole-dipole (e.g., Bing and Greenhalgh, 2000; Dahlin and Zhou, 2004). Pole-tripole was utilized for S2HB configurations after comparative analysis of various sequences indicated optimal resolving ability for a range of target geometries (e.g., Goes and Meekes, 2004; Power et al., 2015; Simyrdanis et al., 2015). The dipole-dipole sequence is one of the most effective and widely used in ERT surveying (e.g., Power et al., 2018) and was used for the surface ERT configuration in this study. Table 3-1 presents the details of the various electrode sequences used in this study.

Table 3-1: Summary of electrode sequences and measurements

Configuration	Sequence	Surface Lines	Borehole Lines	Total Elec.	Total Meas.
S2HB-1BH	PT	11	1	252	6413
Surface	DD	11	0	231	2926
S2HB-3BH	PT	11	3	294	6413
S2HB-FULL	PT	11	11	462	6413

Sensitivity of Configuration

The sensitivity patterns play an important role in the resolving capability of an electrode configuration in the inversion of the data. These patterns are often used to predetermine the imaging ability of electrode sequences and have been used in comparative analyses of different sequences (e.g., Dahlin and Zhou, 2004). The 3D sensitivity patterns within the experimental domain for each S2HB and surface ERT configuration were generated in the geoelectrical modeling package ResIPy (Blanchy et al., 2021), and are shown in Figure 3-

2. The ‘S2HB-1BH’ exhibits increased sensitivity at depth due to the deployment of horizontal borehole electrodes. While high sensitivity occurs directly around the borehole, the sensitivity decreases with increasing lateral distance from the borehole (i.e., lowest sensitivity in the corners). Additional boreholes provide increased lateral sensitivity, with highest 3D sensitivity occurring when all boreholes are deployed in ‘S2HB-FULL’. As expected, surface ERT provides the lowest sensitivity.

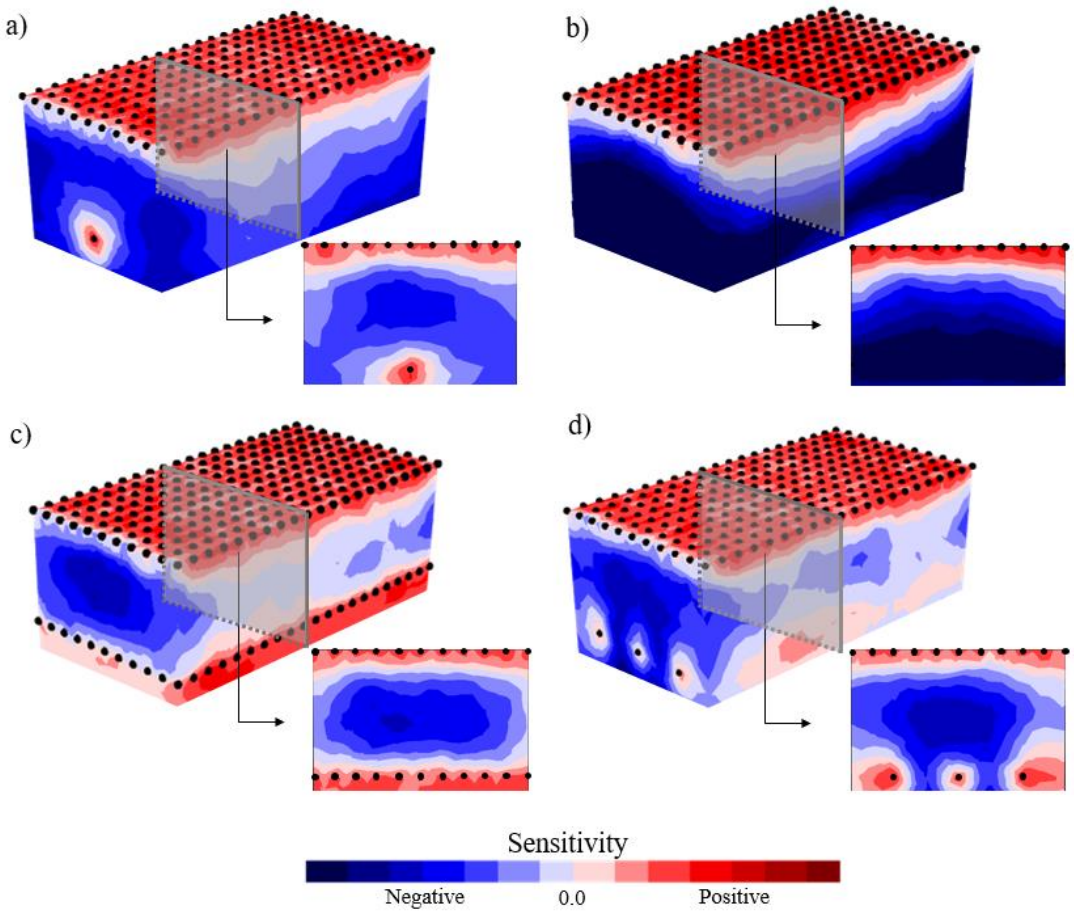

Figure 3-2: 3D volumes and 2D cross-sectional images indicating the electrode placement of each configuration and their sensitivity patterns: (a) S2HB-1BH, (b) surface, (c) S2HB-FULL, and (d) S2HB-3BH. Note that the red and blue represent the regions with the highest and lowest sensitivity, respectively.

Target Design

The 3D targets within the experimental domain were designed to investigate the relative imaging performance of the 3D S2HB configurations. The target geometry was based on the sensitivity pattern of S2HB-1BH, as it is expected to have the lowest 3D sensitivity of all S2HB configurations (see Figure 3-2) and is the main focus of this study. Figure 3-3 presents a simplified sensitivity image of the high sensitivity (red) and low sensitivity (blue) areas associated with S2HB-1BH (i.e., inverted triangle). A target geometry that is fully encapsulated by the most sensitive area is in the shape of a 'T', as shown in Figure 3-3a. This shape, hereafter referred as 'Standard-T', is expected to be well characterized by all S2HB configurations, since the vertical portion of the shape is positioned directly over the central single horizontal borehole. While this deeper vertical portion is expected to be poorly resolved by surface ERT, the shallower horizontal portion should be more amenable.

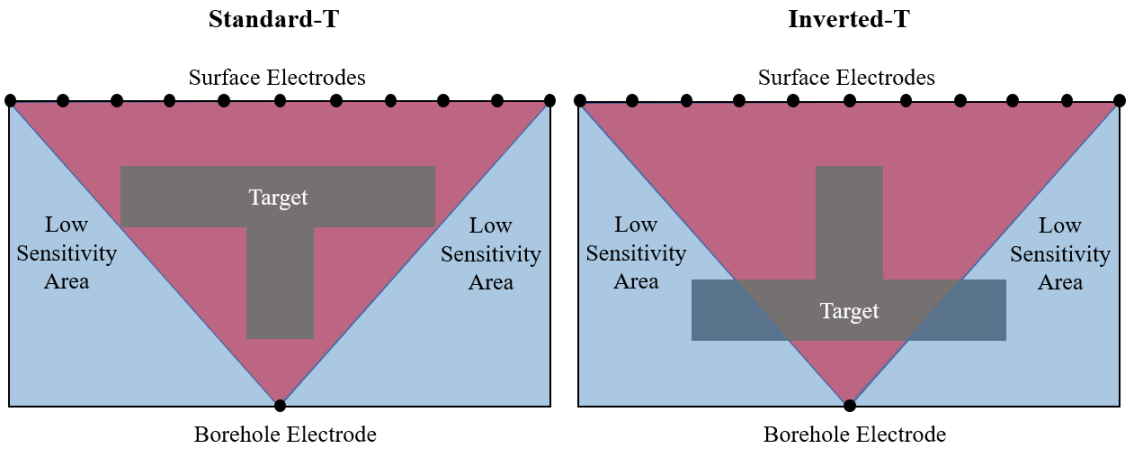

Figure 3-3: Simplified schematic highlighting the expected areas of low sensitivity for the S2HB-1BH. Also shown are the two targets used for this study: (a) 'Standard-T', and (b) 'Inverted T'.

An inverted 'T', hereafter referred to as 'Inverted-T', exhibits the same target volumes but provides an ideal geometry to compare the performance of each configuration. Now that the horizontal portion is at deeper, its lateral sides reside outside the triangular sensitivity area of S2HB-1BH, as shown in Figure 3-3b. The addition of two boreholes in S2HB-3BH

extends the base of the sensitivity area (i.e., triangle to trapezoid) to now capture most of the target. As S2HB-FULL deploys all borehole lines, it encompasses all of the target. Therefore, comparative performance of the configurations with limited, but more practical, borehole numbers – S2HB-1BH and S2HB-3BH – and all boreholes – S2HB-FULL – can be completed to determine the lateral extent of the horizontal borehole sensitivity. Furthermore, Inverted-T provides a more challenging target for surface ERT, specifically the deeper horizontal portion.

The Standard-T and Inverted-T targets in Figure 3-3 will be separated into two portions to provide multiple sub-targets for assessing static (i.e., one-off) imaging. Time-lapse monitoring can also be performed with three time-steps: (T1) uniform background with zero target, (T2) background and bottom portion, and (T3) background, bottom portion, and top portion (i.e., full targets in Figure 3-3).

3.2.3 Experimental Approaches

Numerical Modeling

In this study, the geoelectrical software program ResIPy (Blanchy et al., 2021) is used to perform: (i) forward modeling of synthetic model scenarios, and (ii) inversion of synthetic and experimental data. ResIPy is a user-friendly, open-source package that comprises a range of forward modeling and inversion capabilities that exhibited the versatility to handle forward modeling and inversion of the various electrode configurations and subsurface targets discussed. It was selected following extensive testing with numerous geoelectrical packages, including IP4DI (Karaoulis et al., 2013), DCPro (Kim et al., 2010) and Res3D (Loke et al., 2021).

The forward model is first used to simulate the S2HB-1BH and surface ERT surveys of the 3D experimental domain (Figure 3-1) containing the 3D Inverted-T target (Figure 3-3a). The model domain (Figure 3-1) is discretized into smaller specified finite elements, with a half-space (tetra) mesh selected with a top growth factor of 8, and a bottom growth factor of 100. The electrical resistivity value of each element within the model background is 40 ohm-m, which is similar to the resistivity of groundwater. This background represents

time-step T1. The 3D volume of the Inverted-T sub-targets (T2 and T3) are positioned at the specified location, with all associated elements exhibiting a very high resistivity value of $1x10^{-15}$ ohm-m to represent DNAPL. ERT surveying of each model domain (T1, T2 and T3) is then simulated using the S2HB-1BH and surface electrode configurations. Table 3-2 presents a summary of the numerical model experiments completed.

The construction of subsurface images from the surveyed data is a nonlinear inverse problem with the goal of recovering the model (electrical resistivity) that reproduces the surveyed raw data. The synthetic survey data is inverted with ResIPy, an iterative least-squares smoothness-constrained inversion program (Blanchy et al., 2021). Normal regularization is utilized, with a maximum number of five iterations.

Table 3-2: Summary of all numerical models and experiments completed

Experiment Type	**Target Arrangement**	**Electrode Configuration**			
		S2HB-1BH	**Surface**	**S2HB-3BH**	**S2HB-FULL**
Numerical	Inverted T (24cm depth)	✔	✔	✔	✔
Experiment (Water/Plastic)	Standard T (24cm depth)	✔	✔		✔
	Inverted T (24cm depth)	✔	✔	✔	✔
	Inverted T (32cm depth)	✔	✔		
Experiment (Sand/NAPL)	Inverted T (24cm depth)	✔	✔		

Laboratory Tank Experiments

A suite of laboratory experiments was conducted within a sub-volume of a large plastic tank (1.2 m x 1.2 m x 1.0 m), with the same dimensions and geometry of the model domain and targets used in the numerical simulations. The first set of experiments involves: (i)

moderately conductive water as the background, and (ii) highly resistive plastic as the DNAPL targets. A PVC frame was constructed to hold the various electrode lines in place, while incorporating flexibility for vertical and lateral adjustments of all lines. A plastic mesh sheet was also constructed and placed inside the tank to provide a platform for the placement of the plastic targets.

It was possible to complete experiments with both the Standard-T and Inverted-T targets due to the efficiency and simplicity of experimental setup and clean-up. As with the numerical simulations, each experiment consisted of three time-steps. The first time-step (T1) for both Standard-T and Inverted-T targets consisted of only water (including the PVC frame and mesh platform). The second time-step included the addition of plastic containers in the shape of the sub-target (T2), specifically the portion that sits on the platform (i.e., vertical portion of Standard-T and horizontal portion of Inverted-T). The third timestep involved the full target (T3), with the horizontal portion added to Standard-T and the vertical portion added to Inverted-T. Figure 3-4 presents photographs of the water and plastic experiments during set-up and measurements.

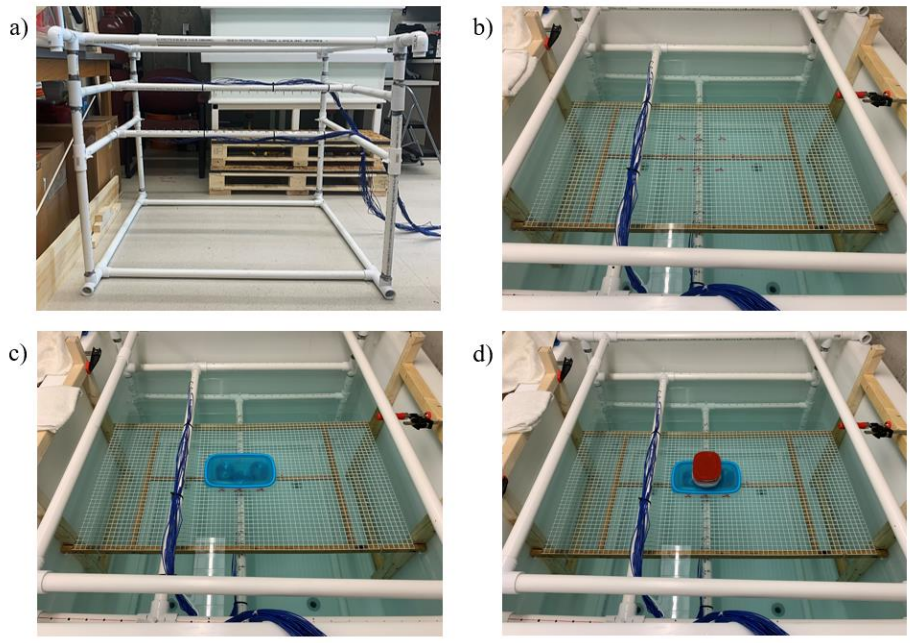

Figure 3-4: Photographs showing the setup and example measurements of the Inverted-T water and plastic experiments: (a) PVC frame for housing electrode lines, (b) plastic mesh platform in time-step T1, (c) water and plastic during measurement of T2, (d) water and plastic during measurement of T3.

Figure 3-5 illustrates the experimental set-up, showing the front, side, and top views of the targets and electrode lines. It is noted that the S2HB-1BH, surface, and S2HB-FULL configurations were employed for the Standard-T experiments, while all four configurations (including S2HB-3BH) were employed for the Inverted-T experiments (see Table 3-2).

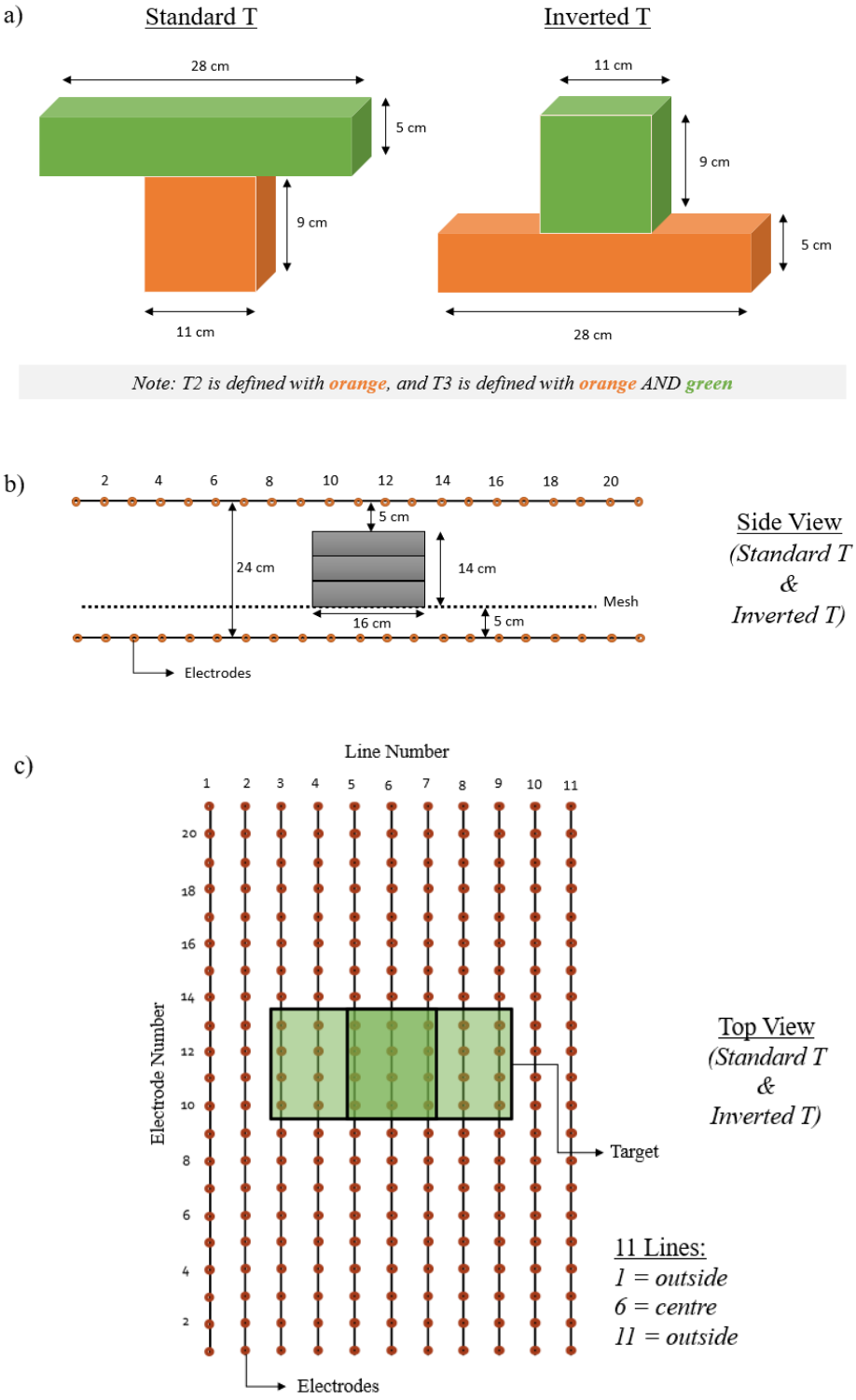

Figure 3-5: Illustration of the Inverted-T 'water and plastic' experimental set-up: (a) 3D volume of time-step T2 and T3 (note that T1 is just the background water), (b) side view and (c) top view showing the Standard-T and Inverted-T target and the electrode lines.

A laboratory experiment containing saturated sand as the background and NAPL progressively filling the Inverted-T target volume was then conducted. Six electrode lines were used on the surface; they provided the same lateral extent as the previous 11 lines but skipped every second line (i.e., Lines 2, 4, 6, 8, and 10 were skipped), with interline spacing now 0.08 m. A single horizontal borehole line was used at the same depth of 0.24 m. Only the Inverted-T target was tested due to the complexity and time-consuming nature of this experiment. Furthermore, only the S2HB-1BH and surface ERT configurations were used for the following two reasons. Firstly, the overall objective was to confirm that 3D S2HB ERT provided superior imaging to 3D surface ERT, with the 3D S2HB-1BH configuration being the most realistic and practical to employ. Secondly, the nature of NAPL migration over time means that time-lapse changes are constantly occurring and the time to record all ERT measurements should be minimized to maintain data quality with no unwanted changes occurring during the measurement time. While S2HB-3BH and S2HB-FULL have the same measurements as S2HB-1BH, it was not possible to record all of them between time-steps.

The experimental tank was first filled with fine-grained sand to the elevation of the horizontal borehole (i.e., 0.7 m from the bottom of the tank), with 0.02 m lifts and adequate compaction. The horizontal borehole line of electrodes was then installed and carefully backfilled with 0.05 m of fine sand to the bottom of the Inverted-T target. The target volume was backfilled with coarse sand and surrounded by fine sand to ensure NAPL preferentially migration within the target volume. Aluminum sheeting in the shape of the target was used to allow simultaneous backfilling of the coarse sand and fine sand. NAPL injection was provided via two screened horizontal wells placed in the bottom of the target volume and one point injection well in the middle of the vertical portion of the Inverted-T target. Once sand placement was completed, it was fully saturated with water flowing through four ports at the base of the tank. Photographs showing the preparation of the experiment is shown in Figure 3-6.

NAPL migration was separated into five time-steps, based on approximately equal volumes of NAPL injection. The porosity of the coarse sand was measured to be 0.40, and the total

volume NAPL required to fill the target was calculated to be 1500 mL. The first time-step (T1) consisted of the background sand media and groundwater (i.e., 0 mL NAPL). The second to fifth time-steps injected specific volumes of NAPL to progressively displace the groundwater out of the Inverted-T shape, before full NAPL saturation. NAPL volumes of 420 mL, 420 mL, 360 mL, and 300 mL were injected in time-steps T2, T3, T4, and T5 respectively. Canola oil with a density of 900 kg/m^3 was used as a non-toxic NAPL surrogate. The oil was dyed with Oil-Blue N to enhance its visualization, particularly during post-experiment excavation. It was then placed in large syringes and injected at a flow rate of 10 mL/min using a syringe pump.

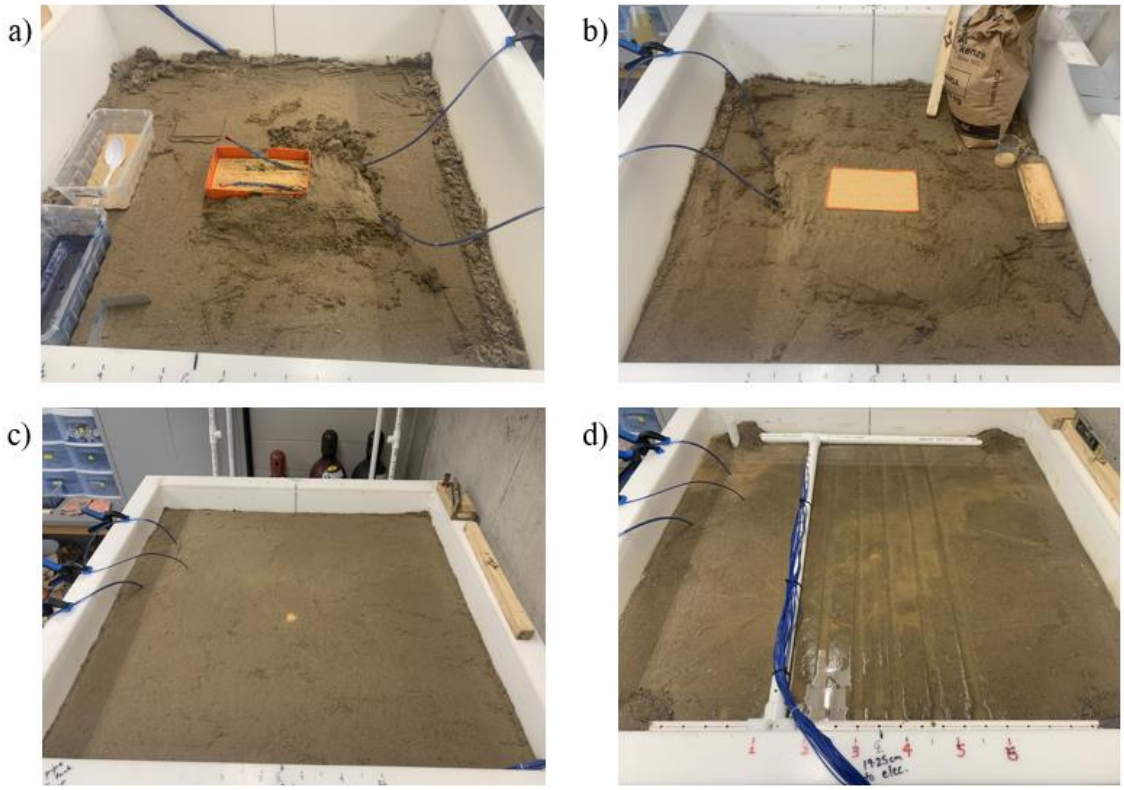

Figure 3-6: Photographs showing the setup and example measurements of the Inverted-T sand and NAPL experiments: (a) installation of the horizontal remediation wells within the base of the horizontal portion of the Inverted-T, (b) packing of fine sand (brown) and coarse sand (orange) at the top of the horizontal portion, (c) completed backfilling of the experimental tank, (d) S2HB ERT measurements along Line 1 of time-step T5.

In all laboratory experiments, a multi-channel Syscal Pro Switch 48 resistivity meter (IRIS Instruments, France) was used to record the measurements of apparent resistivity. This instrument allows for high productivity measurements with a precision of 0.2% and threshold voltage of 1μV. The system features an internal switching board for 48 electrodes, and an internal 250W power source. The acquisition time for resistivity measurements was 0.5 seconds, while strong ground coupling (ground resistance: <1 kilo-ohm) was attained at all electrodes. All raw data were then inverted and visualized with ResIPy.

3.3 Results & Discussion

As 3D S2HB-1BH ERT is the most practical and realistic electrode configuration to implement at a field site, its imaging performance relative to 3D surface ERT is the main focus of this study. The results of the (i) numerical modeling, (ii) water and plastic experiments, and (iii) sand and NAPL experiments on the Inverted-T target are presented and discussed. A sensitivity analysis section is then presented which further investigates S2HB-1BH ERT when the depth of the borehole (i.e., distance between surface and borehole) is increased. Then S2HB-1BH is compared to configurations with the less realistic but more sensitive three borehole S2HB-3BH and all borehole S2HB-FULL. Both the Inverted-T and Standard-T target are used for this comparison.

3.3.1 Comparative Performance: 3D S2HB-1BH vs 3D Surface

Numerical Modeling

Figure 3-7 presents the imaging results of the Inverted-T target using 3D S2HB-1BH ERT and 3D surface ERT. Figure 3-7a presents cross-sectional slices through the center of the 3D inverted resistivity domains (i.e., *x*-distance of 0.4 m) from surface ERT and S2HB-1BH at each of the three time-steps (T1 to T3). It is important to note that these 2D cross-sectional slices are taken perpendicular to the direction of the measurements, meaning that they can be only generated with 3D inversion, stressing the importance of 3D ERT. It is evident that S2HB-1BH is much more effective at resolving the target, particularly at depth. While surface ERT was unable to resolve T2 (i.e., deeper horizontal portion of Inverted-T), S2HB-1BH was able to adequately resolve it. For T3 (i.e., full target), surface ERT is now able to resolve the shallower vertical portion of the Inverted-T, with S2HB-1BH once again resolving the extent of the target.

Time-lapse monitoring of the changes associated with the evolving target can be shown as percent difference images; for example, T1 can be subtracted from T2 (i.e., T2-T1) to only show the change between T1 and T2 (i.e., deeper horizontal portion). Difference images from time-lapse monitoring can be highly valuable as static ERT imaging, sometimes in any configuration, may not always accurately depict subsurface targets in a one-off scenario. Some field sites and subsurface conditions can be highly heterogeneous, making

it highly difficult to only resolve the intended target; however, difference imaging of changes over time, where the constant heterogeneous background is removed, makes evolving targets more amenable to imaging (e.g., Chambers et al., 2004; Power et al., 2014).

Figure 3-7b presents cross-sectional slices of the T2-T1 and T3-T1 difference images, while full 3D isovolumes at 75% difference are shown in Figures 3-8c to 3-8e to present the complete ERT-imaged target. It is evident that S2HB-1BH ERT also exhibits superior time-lapse monitoring performance relative to surface ERT, even though surface ERT is traditionally aided in time-lapse mode (e.g., Almpanis et al., 2021b). As shown in the cross-sectional images and 3D isovolumes for T2-T1, where the change is associated with the bottom portion of the target, surface ERT is unable to resolve anything. This is because the difference is occurring at a depth that is too great for surface ERT. In contrast, S2HB-1BH adequately resolves the T2-T1 difference, though it is acknowledged that some overestimation of the vertical extent is evident. For T3-T1, surface ERT nicely captures the top portion of the target but remains unable to resolve the vertical and lateral extent of the rest of the target at depth. However, S2HB-1BH clearly resolves the full difference, which is the Inverted-T minus the background, as shown in the various observational views of the 3D isovolumes.

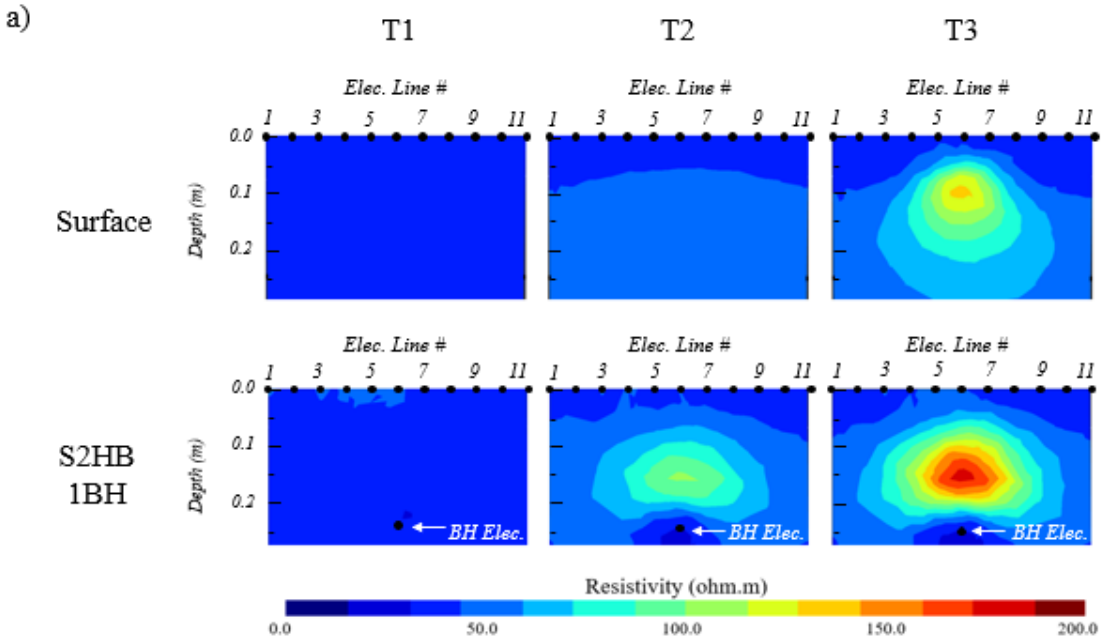
a)
T1
T2
T3
Surface
S2HB
1BH
Elec. Line #
Depth (m)
BH Elec.
Resistivity (ohm.m)
0.0
50.0
100.0
150.0
200.0

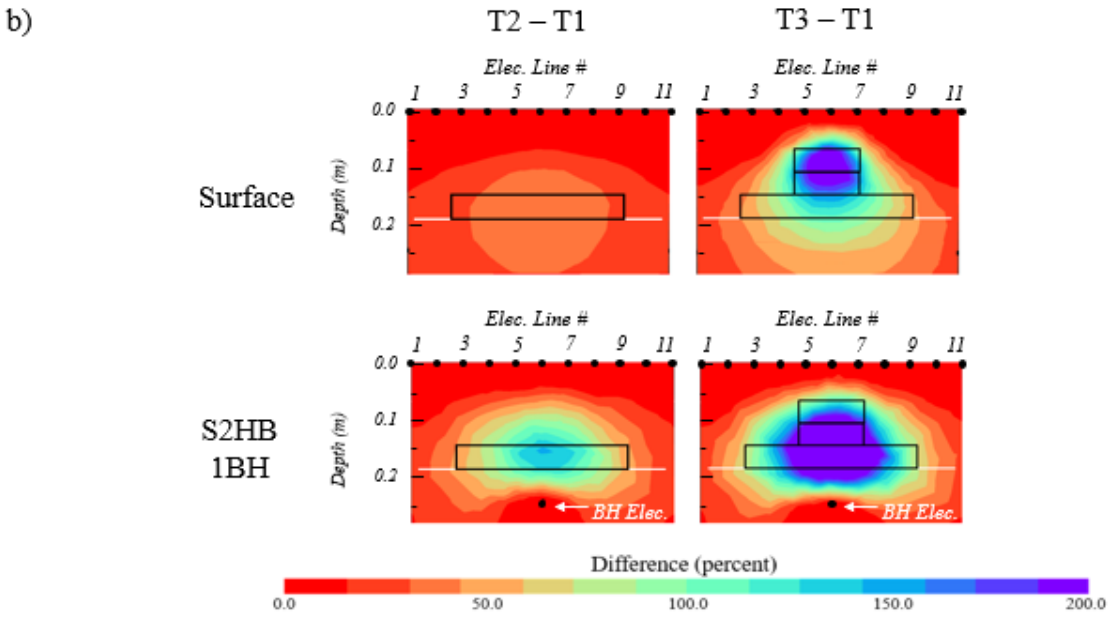
b)
T2 – T1
T3 – T1
Surface
S2HB
1BH
Elec. Line #
Depth (m)
BH Elec.
Difference (percent)
0.0
50.0
100.0
150.0
200.0

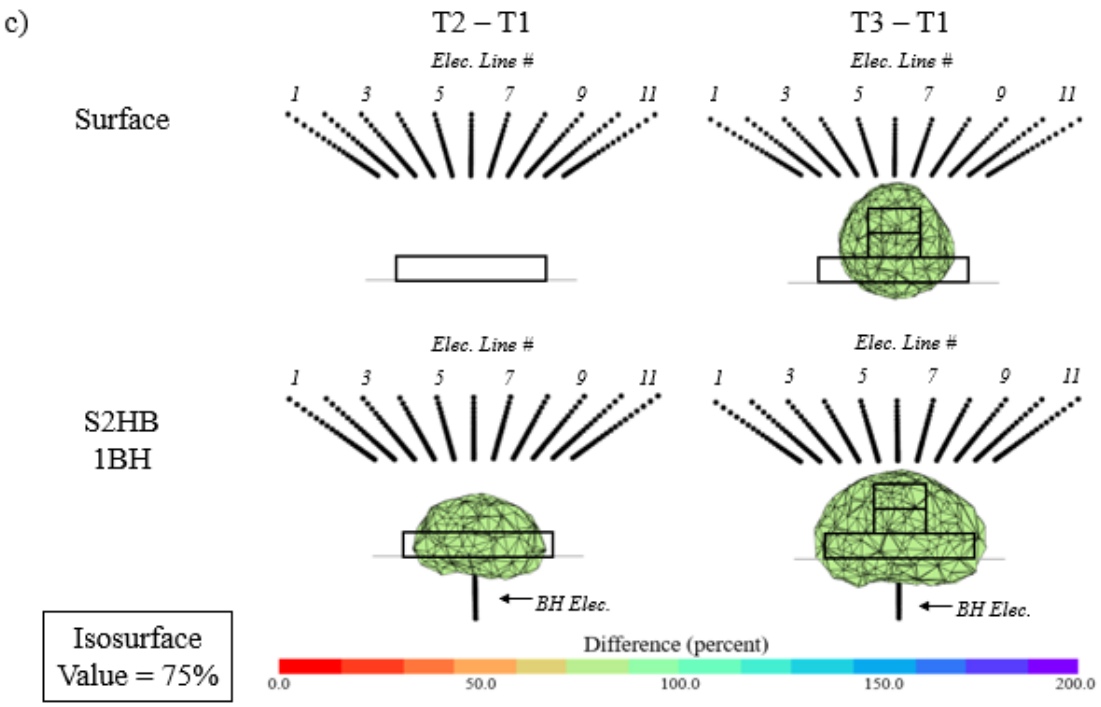
c)
T2 – T1
T3 – T1
Elec. Line #
1 3 5 7 9 11
Surface
S2HB
1BH
BH Elec.
Isosurface
Value = 75%
Difference (percent)
0.0 50.0 100.0 150.0 200.0

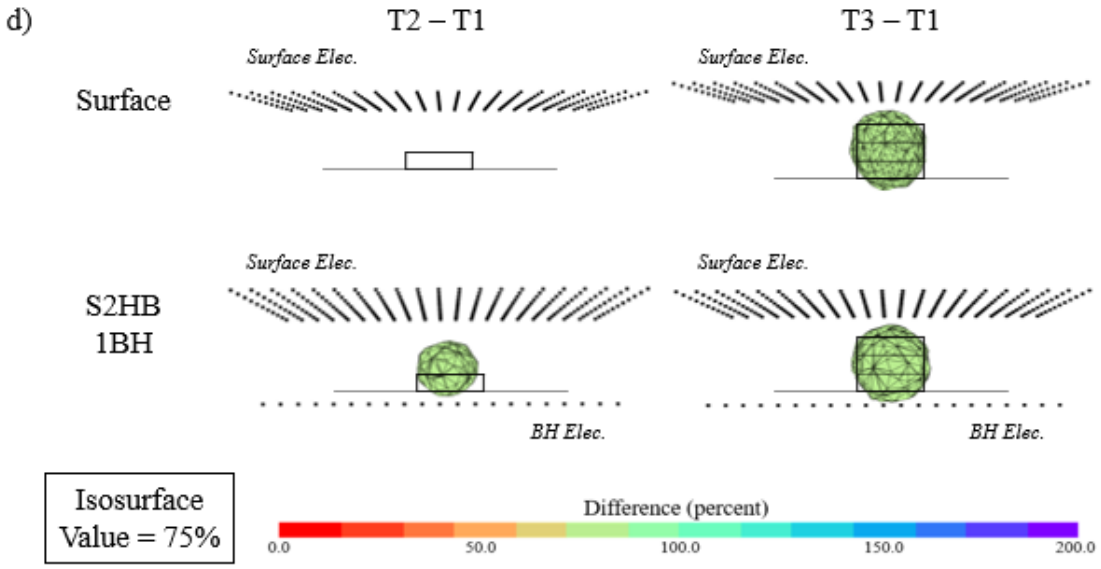
d)
T2 – T1
T3 – T1
Surface Elec.
Surface
S2HB
1BH
BH Elec.
Isosurface
Value = 75%
Difference (percent)
0.0 50.0 100.0 150.0 200.0

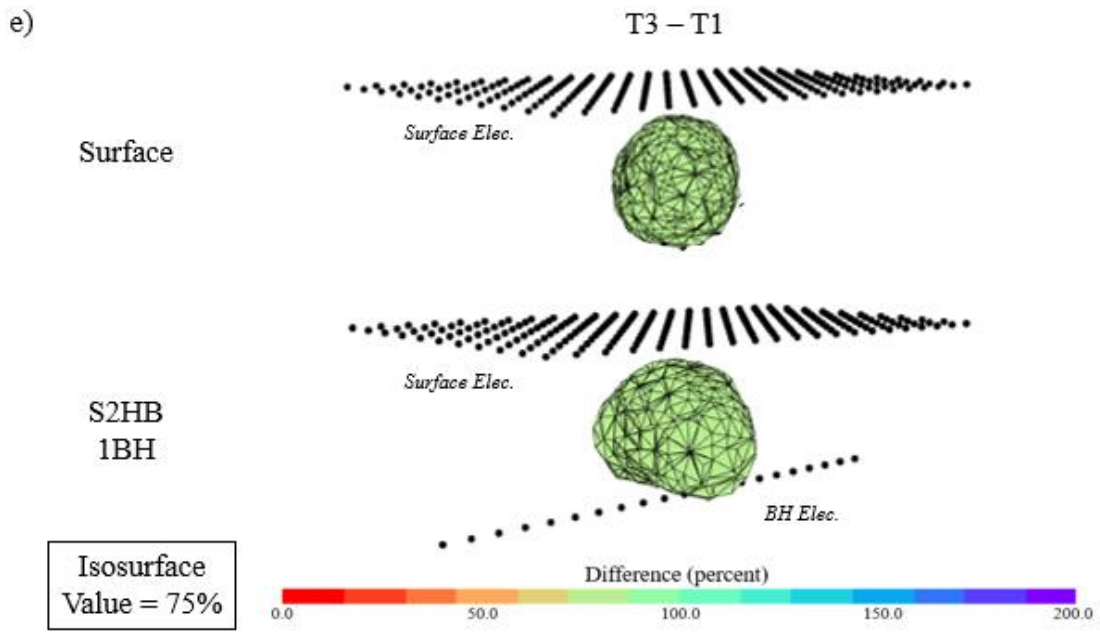

Figure 3-7: Numerical model results from surface ERT and S2HB-1BH ERT of the Inverted-T target: (a) cross-sectional slices of the inverted 3D resistivity domain at time-steps T1, T2 and T3, (b) cross-sectional slices of the difference (%) images between T1 and T2, and T1 and T3, (c) front view of the 3D isovolume differences (75%), (d) side view of the 3D isovolume differences (75%), and (e) oblique view of 3D isovolume differences (75%).

Laboratory Experiments: Water and Plastic

This section presents the results of the water and plastic experiments, where plastic boxes are progressively added to complete the Inverted-T target. The cross-sectional images for T1, T2 and T3, and their corresponding differences, are presented in Figures 3-8a and 3-8b, with 3D isovolumes of the complete target shown in Figures 3-8c to 3-8e. The results again depict a significant improvement with S2HB-1BH ERT in comparison to surface ERT, even in this more realistic laboratory environment. When the first plastic box is added on top of the supporting plastic mesh platform (T2), it is evident from the cross-sectional and isovolume resistivity difference images that surface ERT is unable to resolve this change. S2HB-1BH can accurately detect the center of the change and reasonably capture its vertical extent. While lateral change is captured, its full extent is underestimated. For the complete Inverted-T target in T3, surface ERT is now able to capture the uppermost portion of the target, while still unable to resolve its entire depth. S2HB-1BH performs well though it is acknowledged that some underestimation exists in the lateral extent of the bottom portion and overestimation in the vertical portion, with the ERT-measured shape of the Inverted-T target resembling a trapezoid.

a)

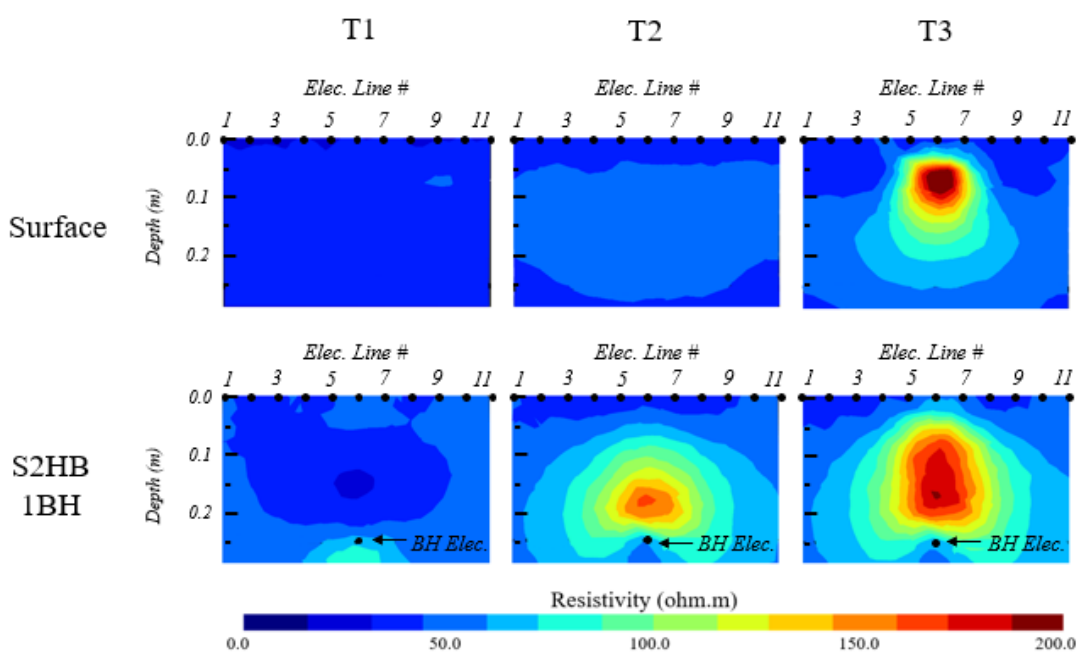
T1
T2
T3
Elec. Line #
1 3 5 7 9 11
Depth (m)
0.0
0.1
0.2
Surface
S2HB
1BH
BH Elec.
Resistivity (ohm.m)
0.0
50.0
100.0
150.0
200.0

b)

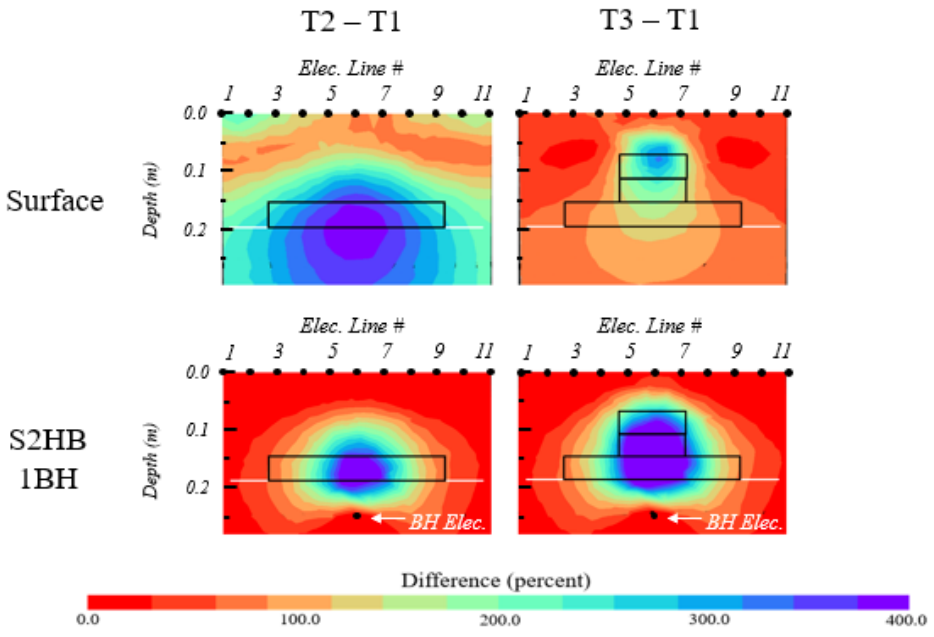
T2 – T1
T3 – T1
Elec. Line #
1 3 5 7 9 11
Depth (m)
0.0
0.1
0.2
Surface
S2HB
1BH
BH Elec.
Difference (percent)
0.0
100.0
200.0
300.0
400.0

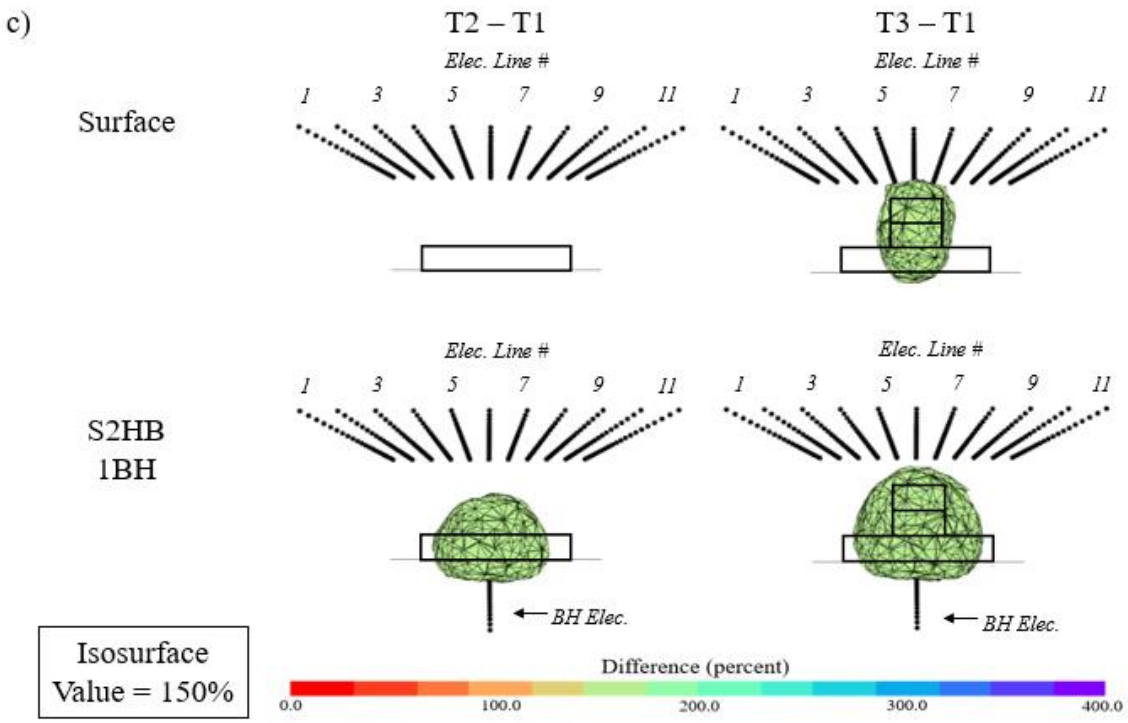
c)
T2 – T1
T3 – T1
Elec. Line #
1 3 5 7 9 11
Surface
S2HB
1BH
BH Elec.
Isosurface
Value = 150%
Difference (percent)
0.0 100.0 200.0 300.0 400.0

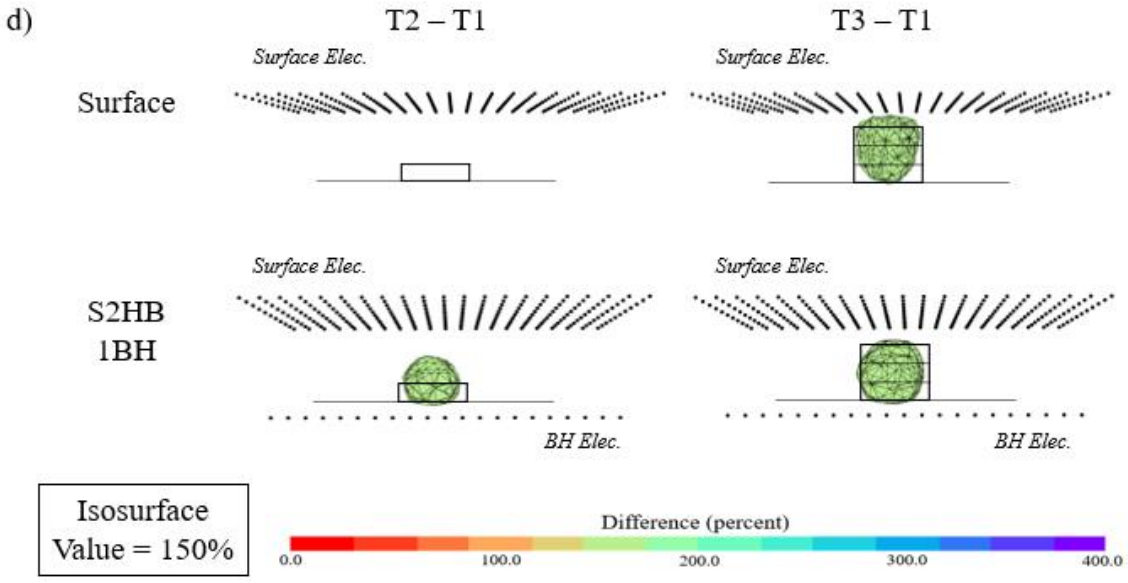
d)
T2 – T1
T3 – T1
Surface Elec.
Surface
S2HB
1BH
BH Elec.
Isosurface
Value = 150%
Difference (percent)
0.0 100.0 200.0 300.0 400.0

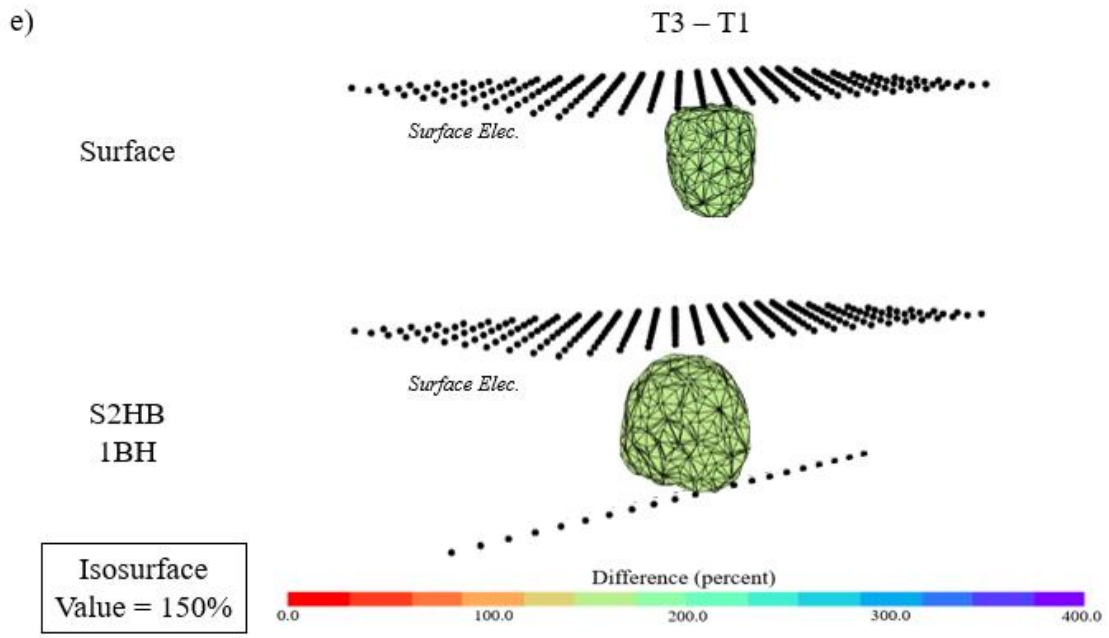

Figure 3-8: Water and plastic laboratory experiment results from surface ERT and S2HB-1BH ERT of the Inverted-T target: (a) cross-sectional slices of the inverted 3D resistivity domain at time-steps T1, T2 and T3, (b) cross-sectional slices of the difference (%) images between T1 and T2, and T1 and T3, (c) front view of the 3D isovolume differences (75%), (d) side view of the 3D isovolume differences (75%), and (e) oblique view of 3D isovolume differences (75%).

Laboratory Experiments: Sand and NAPL

Figure 3-9 presents the results of the sand and NAPL experiment containing five time-step images. It is again evident that S2HB-1BH ERT provides significant improvement in imaging each time-step and associated differences in comparison to surface ERT. In time-steps T2 and T3, with 420 mL and 840 mL of NAPL residing within the target volume, respectively, surface ERT struggles to generate any reasonable image of the target or differences from T1 (i.e., 0 mL NAPL). It is only in T4 and T5, where 1200 mL and 1500 mL reside within the target zone, respectively, that surface ERT is able to capture the NAPL as it migrates upwards into the shallower vertical portion. Even then, it significantly underestimates the magnitude of the target.

In contrast, S2HB-1BH ERT can resolve NAPL throughout all time-steps, and it can reasonably capture the target. It is evident that underestimation exists to the right of the bottom portion, and at the uppermost part of the top portion of the expected target. However, it was evident from the post-experiment excavation that occurred immediately after T5, that NAPL did not fully migrate to these locations. The excavation results can be seen in Figure 3-10. The experiment was designed to completely fill up the Inverted-T shape, with the horizontal injection wells at the bottom expected to evenly distribute the NAPL along the bottom and then gradually fill-up the target volume. However, post-excavation indicated that the final part of the wells got unintentionally blocked by sand, and NAPL was only injected from the leftmost part of the wells, as seen in Figure 3-10. Therefore, the NAPL was able to migrate upwards through the vertical portion of the target without needing to first saturate the entire bottom portion. Furthermore, due to the now localized injection in the bottom left, the injection pressure forced some of the NAPL into the underlying fine sand, which was confirmed during excavation. This unexpected loss of NAPL from the target area meant that the bottom right and top of the target did not have sufficient NAPL volume to eventually saturate fully.

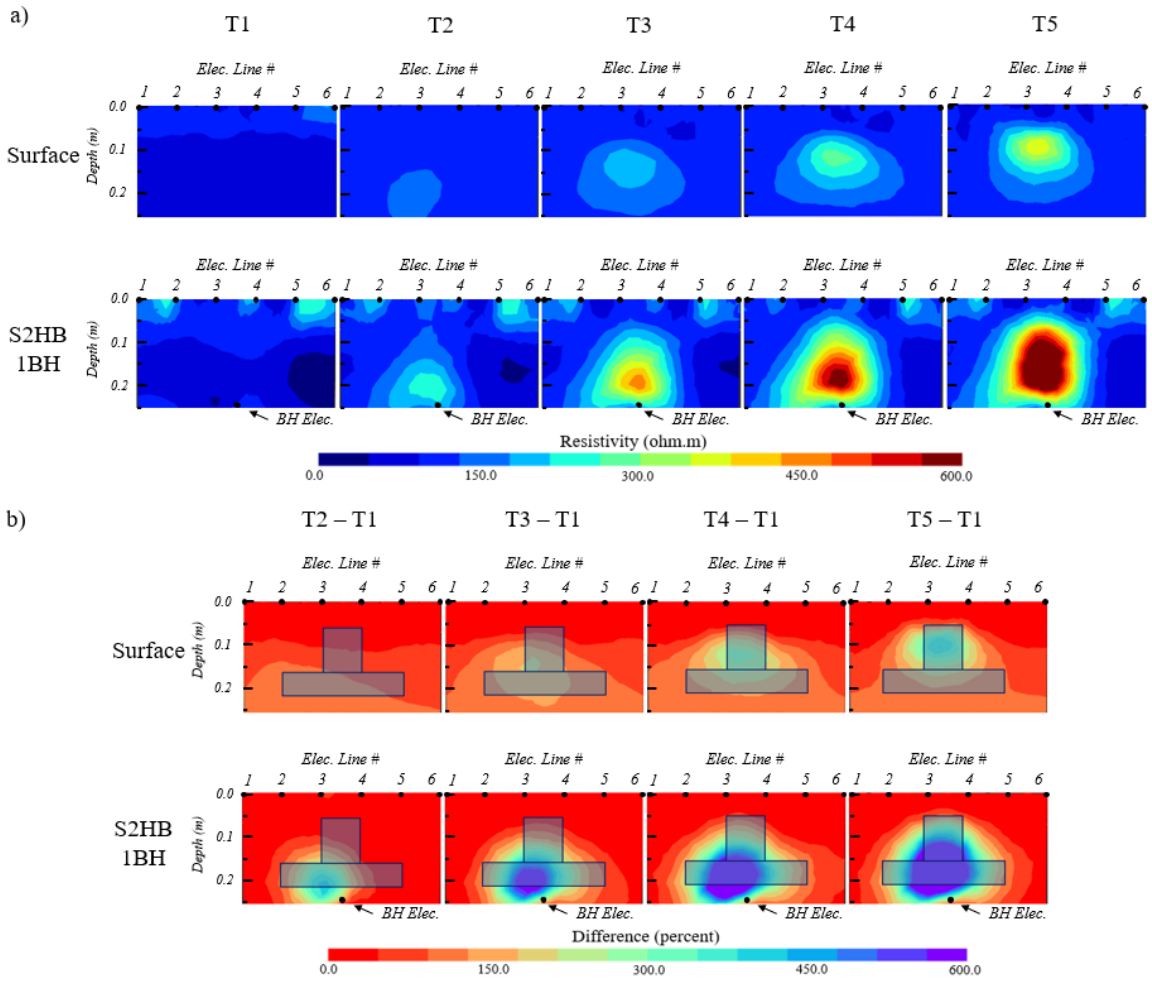
a)
T1
T2
T3
T4
T5
Elec. Line #
Surface
S2HB
1BH
Depth (m)
BH Elec.
Resistivity (ohm.m)
0.0
150.0
300.0
450.0
600.0
b)
T2 – T1
T3 – T1
T4 – T1
T5 – T1
Difference (percent)

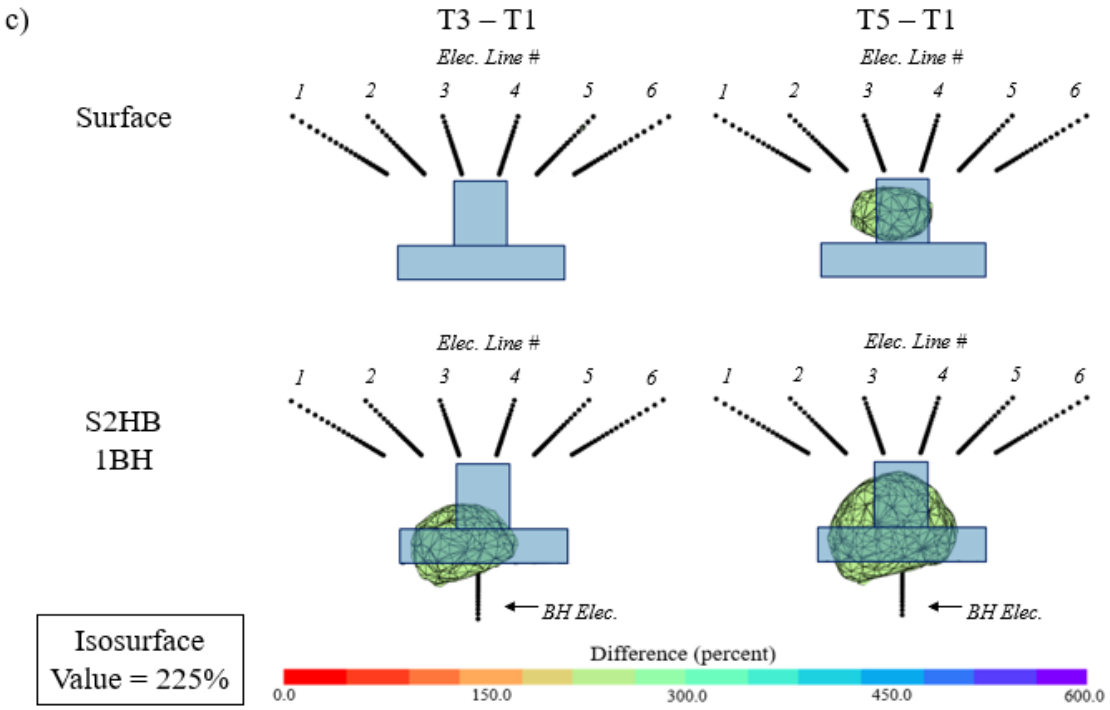
c)
T3 – T1
T5 – T1
Elec. Line #
1
2
3
4
5
6
Surface
S2HB
1BH
BH Elec.
Isosurface
Value = 225%
Difference (percent)
0.0
150.0
300.0
450.0
600.0

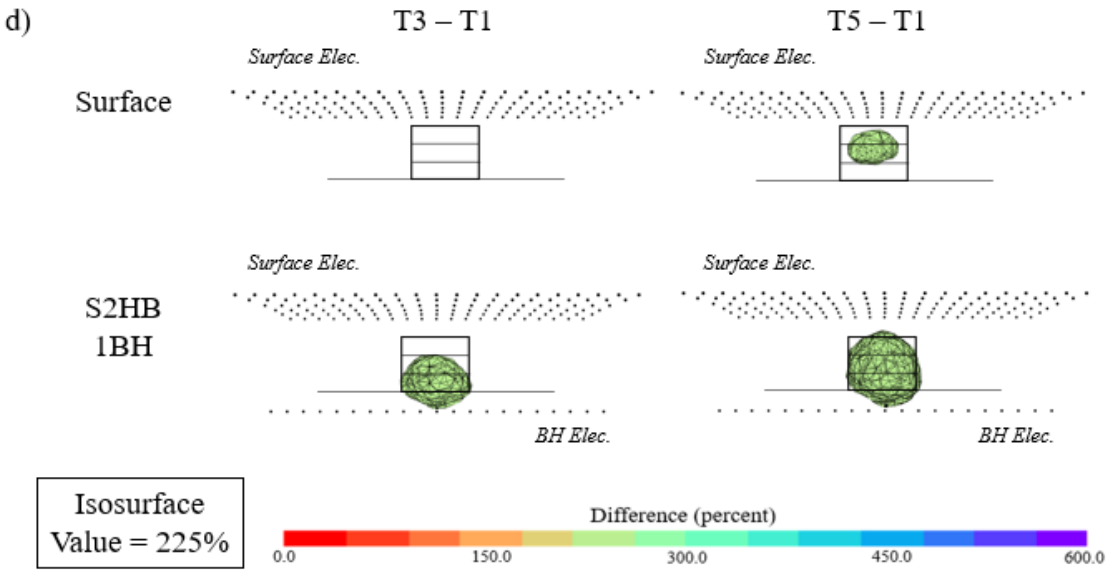
d)
T3 – T1
T5 – T1
Surface Elec.
Surface
S2HB
1BH
BH Elec.
Isosurface
Value = 225%
Difference (percent)
0.0
150.0
300.0
450.0
600.0

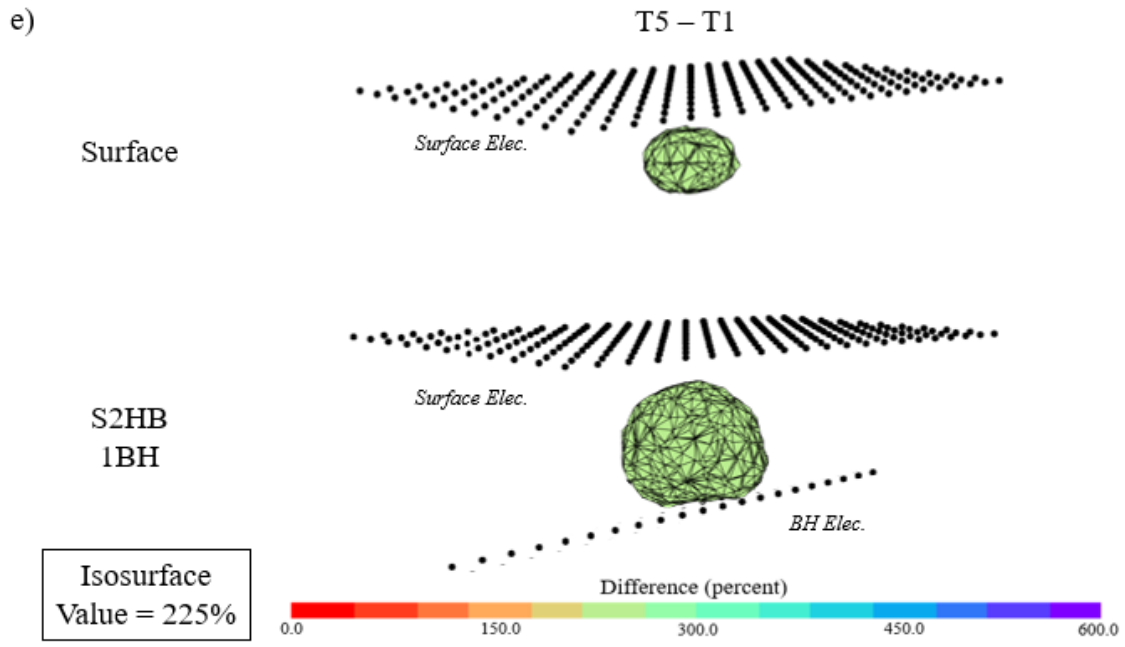

Figure 3-9: Sand and NAPL laboratory experiment results from surface ERT and S2HB-1BH ERT of the Inverted-T target: (a) cross-sectional slices of the inverted 3D resistivity domain at time-steps T1, T2 and T3, (b) cross-sectional slices of the difference (%) images between T1 and T2, and T1 and T3, (c) front view of the 3D isovolume differences (75%), (d) side view of the 3D isovolume differences (75%), and (e) oblique view of 3D isovolume differences (75%).

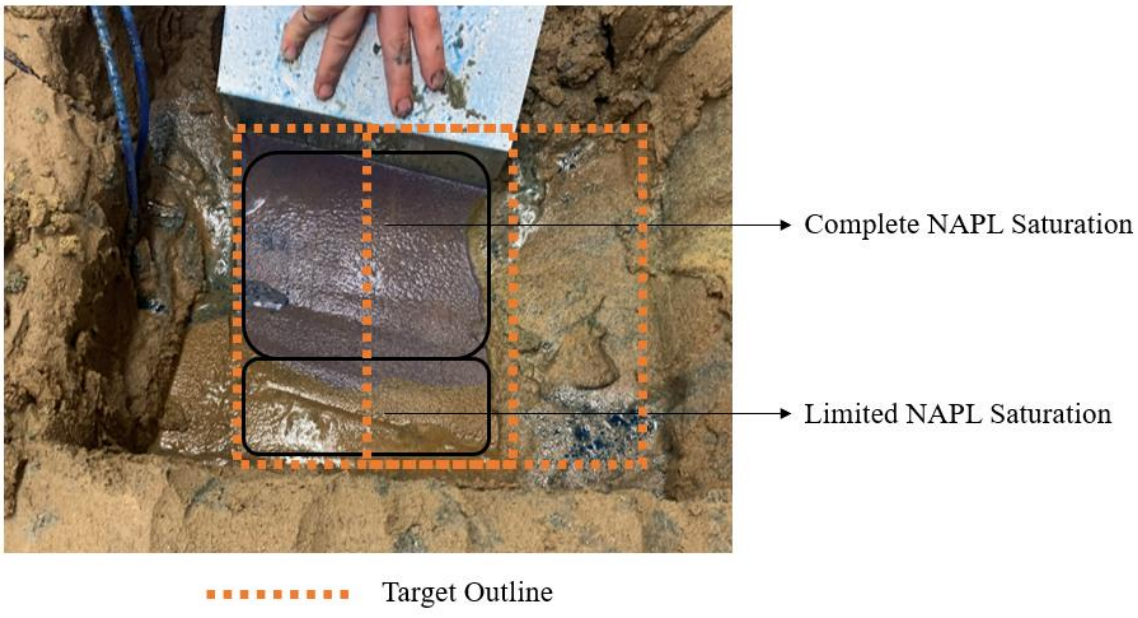

Figure 3-10: Excavation results indicating areas with complete and limited NAPL saturation

Quantitative Analysis: S2HB-1BH vs Surface ERT

In general, ERT results are interpreted qualitatively from the range of images; however, supplementary quantitative information of the data is always welcome, particularly in studies where results from different approaches (e.g., electrode configurations or sequences) are being compared. In this study, quantitative analysis was performed on the resistivity percent difference data. The ERT-measured differences within the 3D target volume are compared with the actual differences using mean average error. Other error calculations such as RMSE were considered, however they can give a relatively high weight to large errors providing an unfair comparison. This analysis was performed on the difference images of the numerical, water and plastic, and sand and NAPL experiments.

Figure 3-11 presents the mean average error for the final difference images from S2HB-1BH ERT and surface ERT from each experiment (e.g., T3-T1 in numerical, and water and plastic; T5-T1 in sand and NAPL). It is evident that the mean average error was much lower for S2HB-1BH ERT than surface ERT in all experiments. Generally, the mean average error for surface ERT was 1.7 to 2.4 times greater than S2HB-1BH ERT. These quantitative values support the qualitative results that suggest that the S2HB-1BH ERT provides improved imaging performance over surface ERT.

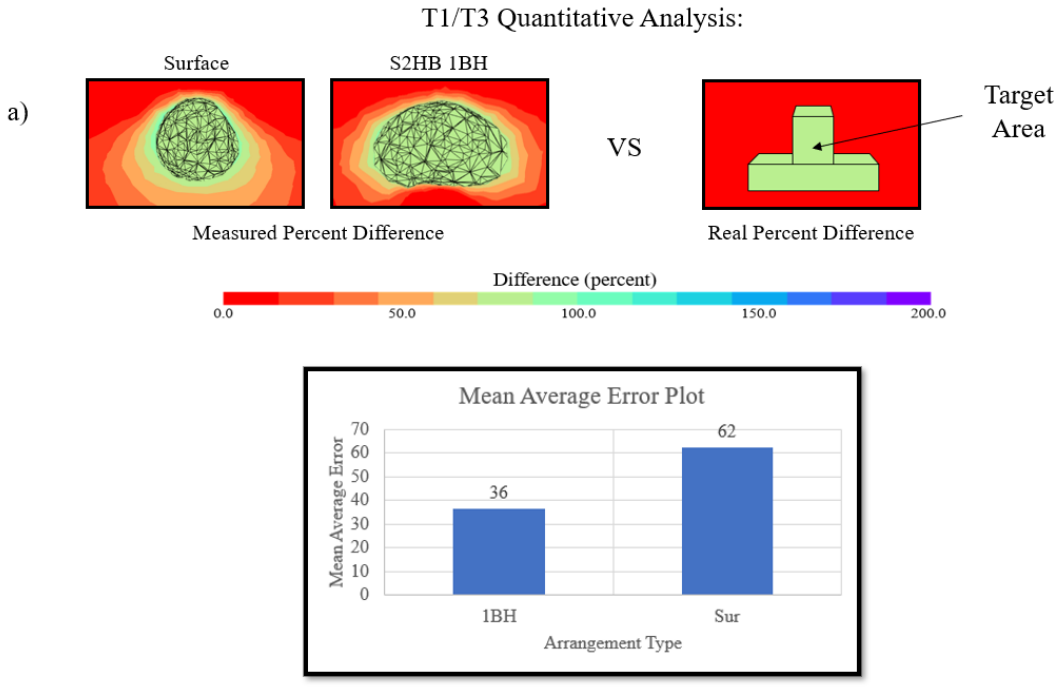

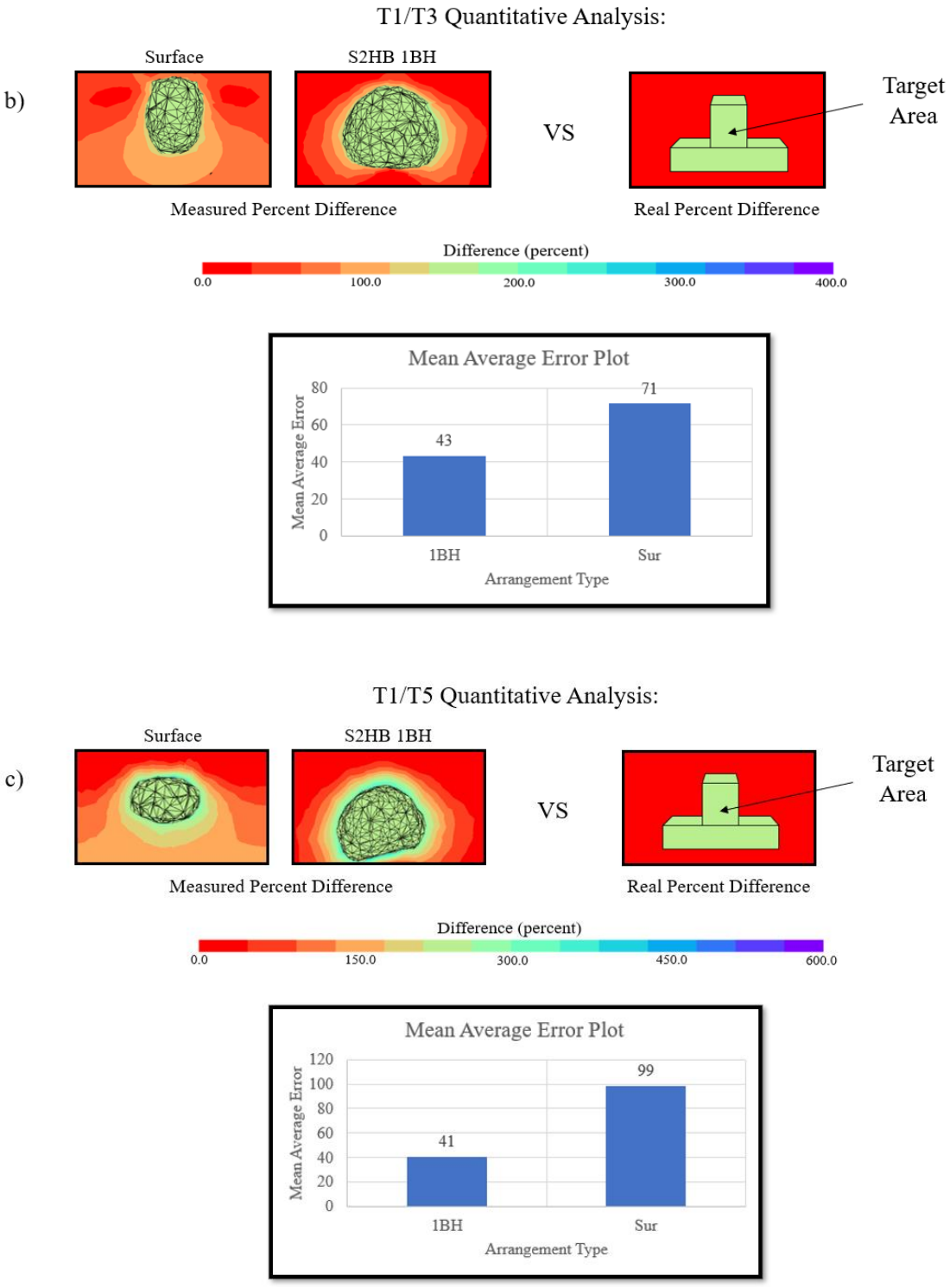

Figure 3-11: Quantitative analysis of mean average error for the ERT-measured percent difference versus the actual percent difference: (a) numerical model results for T3-T1, (b) water and plastic results for T3-T1, and (c) sand & NAPL results for T5-T1.

3.3.2 Sensitivity Analysis of 3D S2HB ERT

Depth of Horizontal Boreholes

The 3D S2HB-1BH and surface ERT imaging of the Inverted-T target in the water and plastic experiments (Figure 3-8) were repeated with the borehole depth increasing from 0.24 m to 0.32 m. In this experiment, the target also increased in depth to maintain the same 5 cm distance from the bottom of the target to the underlying borehole. This provides a realistic scenario at a field site, where the DNAPL source zone is deep and the horizontal borehole is installed as close to the bottom of the source zone as possible, even if the distance to the surface is much larger, which would normally rule out the application of ERT.

Figure 3-12 presents the inverted resistivity results in the form of cross-sectional images and 3D isovolumes. Surface ERT is now completely unable to resolve the Inverted-T target during any time-step. In contrast, S2HB-1BH ERT provides adequate characterization of each time-step and the differences between them. It is acknowledged that the targets are not as well-resolved and pronounced as when the borehole was at 24 cm depth (see Figure 3-8), which is due to the increased distance between surface and borehole. While adequate resolving ability was still attained, it is suggested that for even deeper DNAPL targets, another horizontal borehole line could be added directly above the target to act similar to a surface line. This will be investigated in future work.

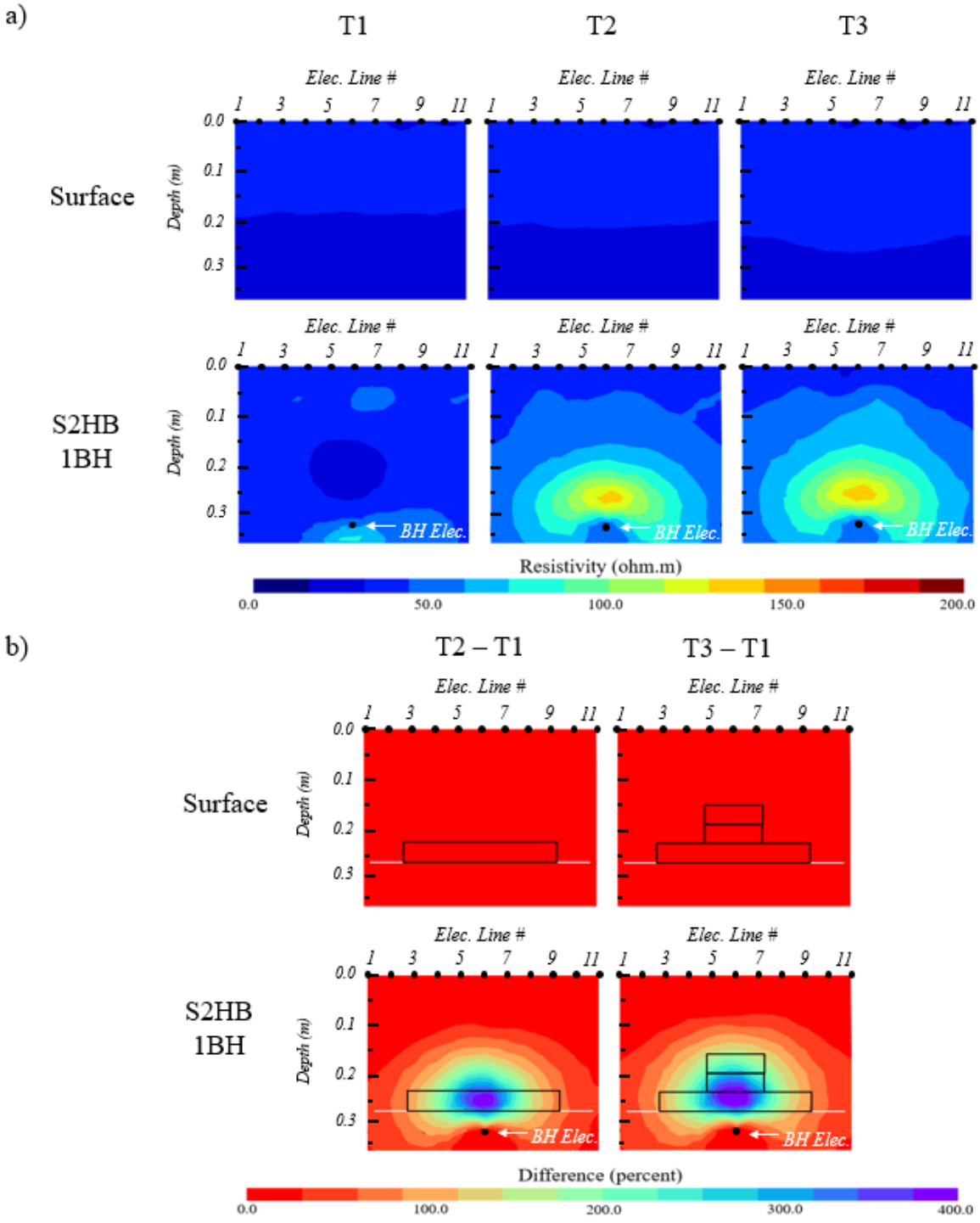
a)
T1
T2
T3
Surface
S2HB
1BH
Elec. Line #
Depth (m)
BH Elec.
Resistivity (ohm.m)
0.0
50.0
100.0
150.0
200.0
b)
T2 – T1
T3 – T1
Difference (percent)
0.0
100.0
200.0
300.0
400.0

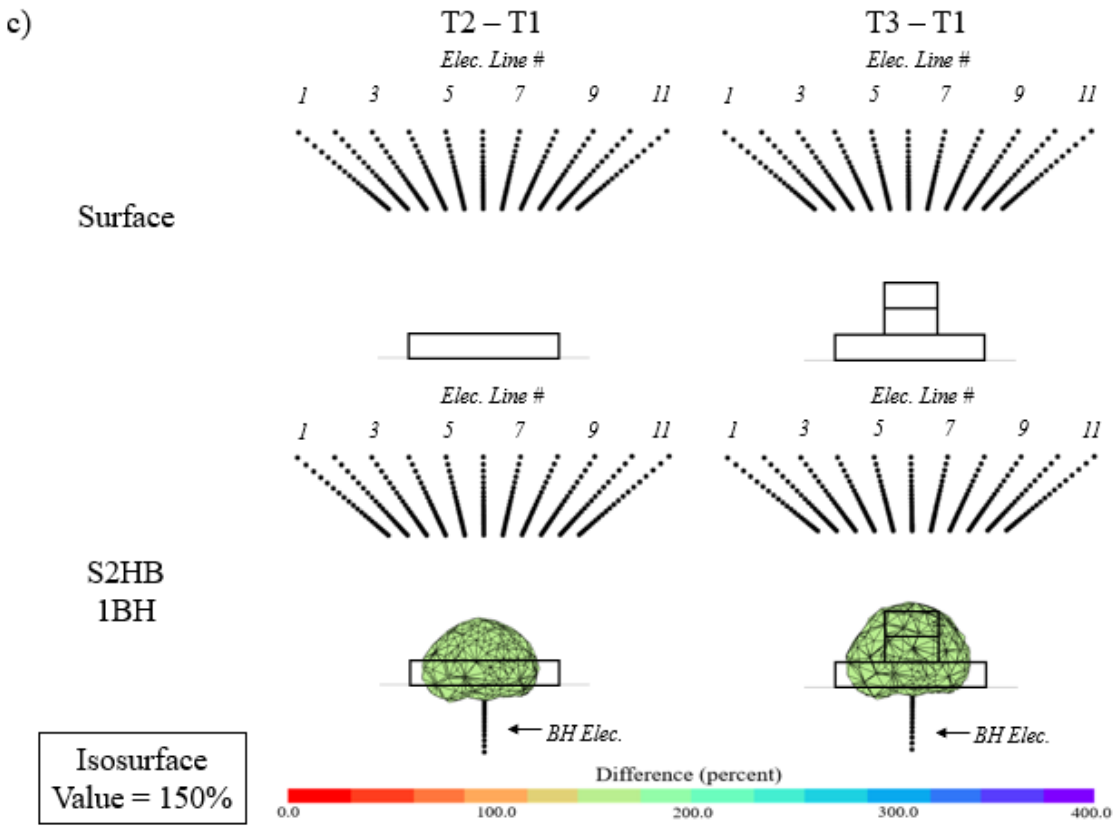
c)
T2 – T1
T3 – T1
Elec. Line #
1 3 5 7 9 11
Surface
S2HB
1BH
BH Elec.
Isosurface
Value = 150%
Difference (percent)
0.0 100.0 200.0 300.0 400.0

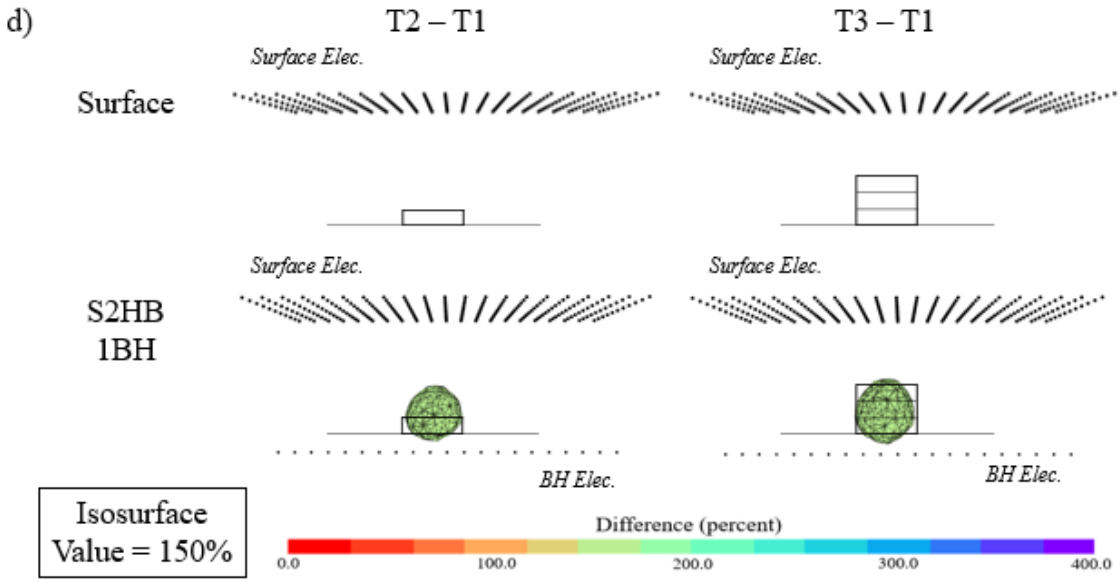
d)
T2 – T1
T3 – T1
Surface Elec.
Surface
S2HB
1BH
BH Elec.
Isosurface
Value = 150%
Difference (percent)
0.0 100.0 200.0 300.0 400.0

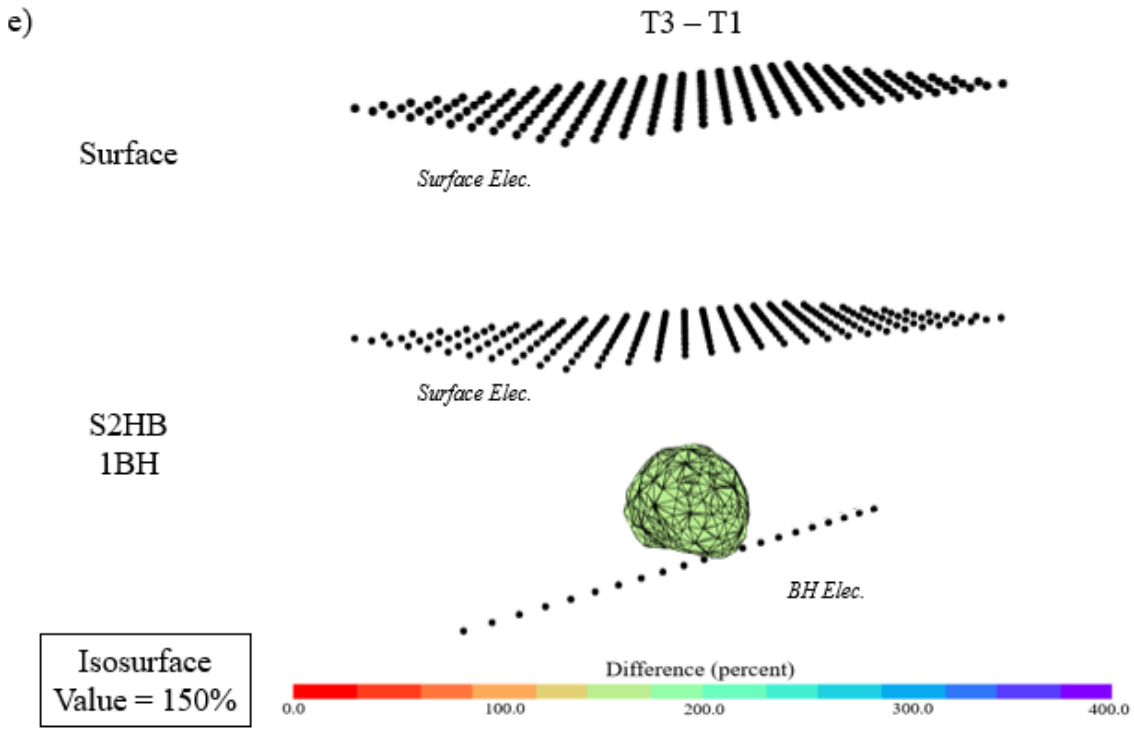

Figure 3-12: Water and plastic experiment results from surface ERT and S2HB-1BH ERT when the borehole has been increased from 0.24 m to 0.32 m: (a) cross-sectional slices of the inverted 3D resistivity domain at time-steps T1, T2 and T3, (b) cross-sectional slices of the difference (%) images between T1 and T2, and T1 and T3, (c) front view of the 3D isovolume differences (75%), (d) side view of the 3D isovolume differences (75%), and (e) oblique view of 3D isovolume differences (75%).

Number of Horizontal Boreholes

Inverted-T Target

This focus of this section is to evaluate the imaging performance of S2HB-1BH if additional horizontal borehole lines were deployed. Figure 3-13 presents the results of S2HB-1BH, S2HB-3BH and S2HB-FULL for imaging the Inverted-T target in the water and plastic experiment. It should be noted that results from numerical simulations of this experiment are provided in Appendix A.

The results indicate that S2HB ERT improves as the number of borehole lines increases from one borehole to three boreholes, and then to 'full' boreholes with a horizontal borehole underlying every surface line. This is most evident in the second time-step (T2) resistivity, difference, and 3D isovolume images, where S2HB-1BH can identify the center of the target but underestimates its magnitude and extent compared to S2HB-3BH and S2HB-FULL. In the final time-step containing the complete Inverted-T target (T3), S2HB-1BH can again detect its general location and shape but underestimates its overall extent, which is most evident in the 3D isovolumes in Figure 3-13c. In contrast, S2HB-3BH and S2HB-FULL provide improved characterization of the extent and magnitude of the target.

While the S2HB-1BH did not perform as highly as S2HB-3BH and S2HB-FULL, it still provides reasonable characterization of the target. Therefore, it is a trade-off between the more realistic and practical deployment of a single horizontal borehole with adequate resolving ability, or improved resolving ability but with impractical numbers of boreholes needed, specifically in the case of S2HB-FULL. It is evident that S2HB-3BH provided very similar results to S2HB-FULL, suggesting that a full array of boreholes is not needed and that three, or even two, boreholes may provide the additional image performance required for some sites. Future work will assess the deployment of more than one borehole, and their optimal location and measurement sequence.

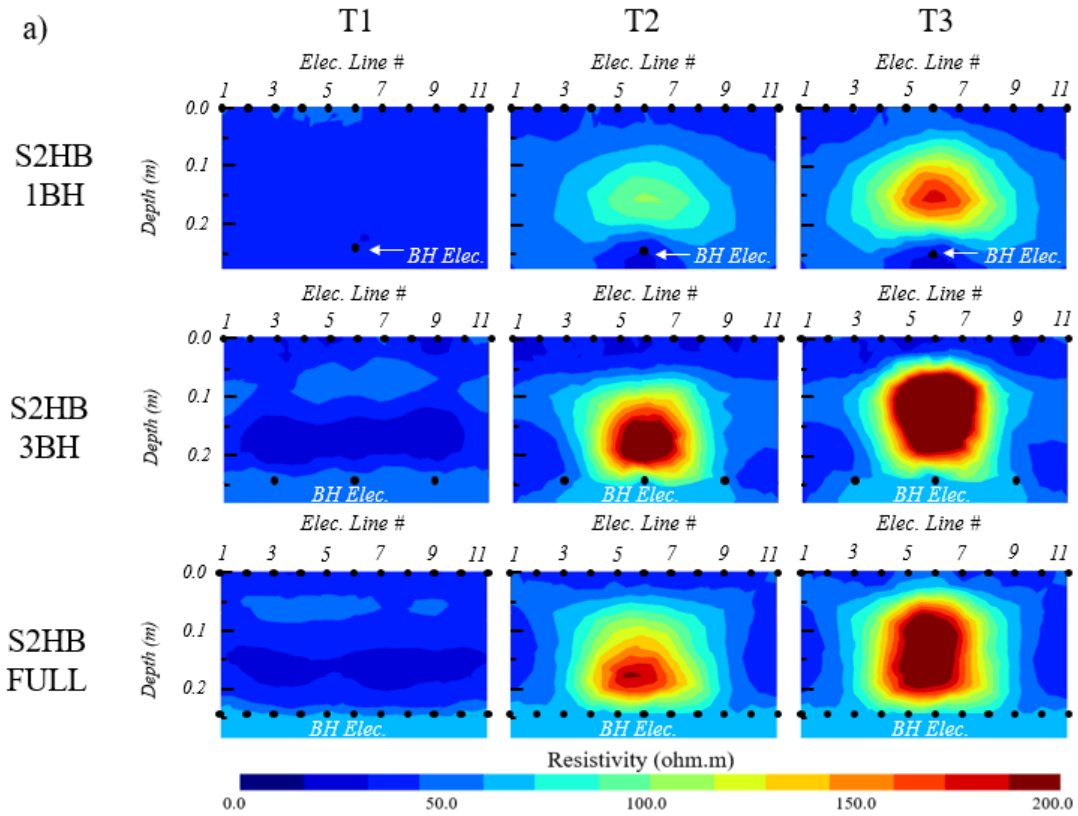
a)
T1
T2
T3
S2HB 1BH
S2HB 3BH
S2HB FULL
Elec. Line #
Depth (m)
BH Elec.
Resistivity (ohm.m)
0.0
50.0
100.0
150.0
200.0

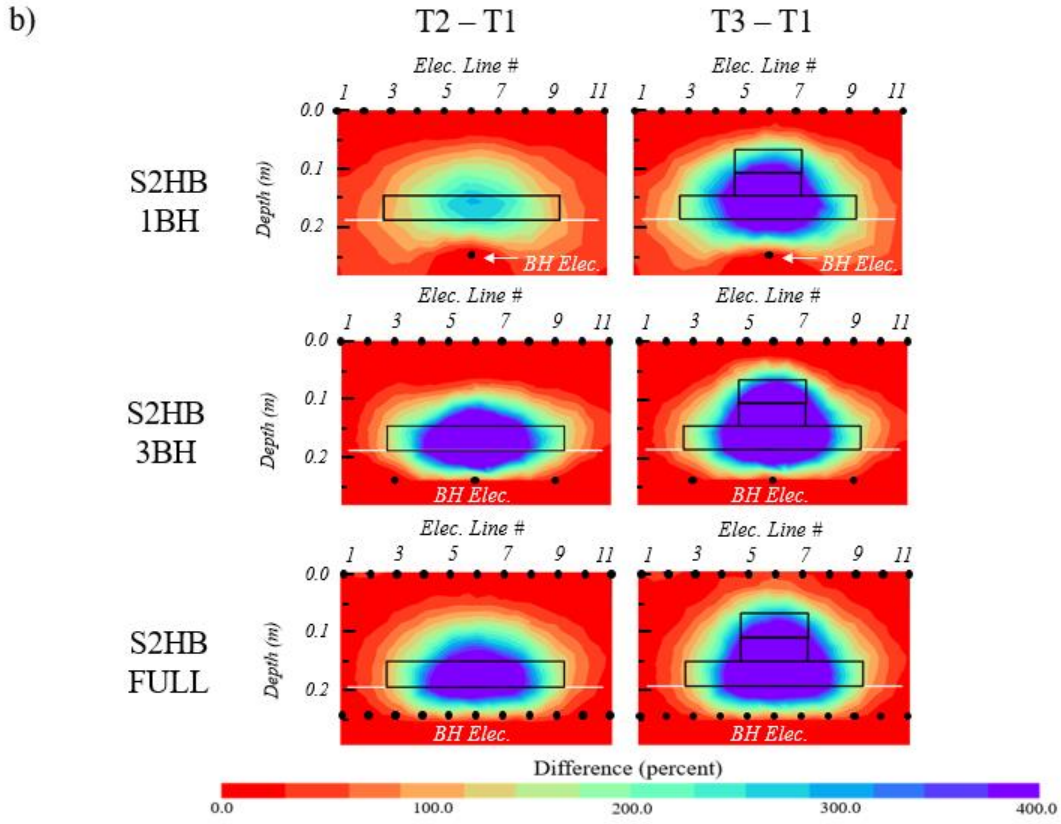
b)
T2 – T1
T3 – T1
S2HB 1BH
S2HB 3BH
S2HB FULL
Elec. Line #
Depth (m)
BH Elec.
Difference (percent)
0.0
100.0
200.0
300.0
400.0

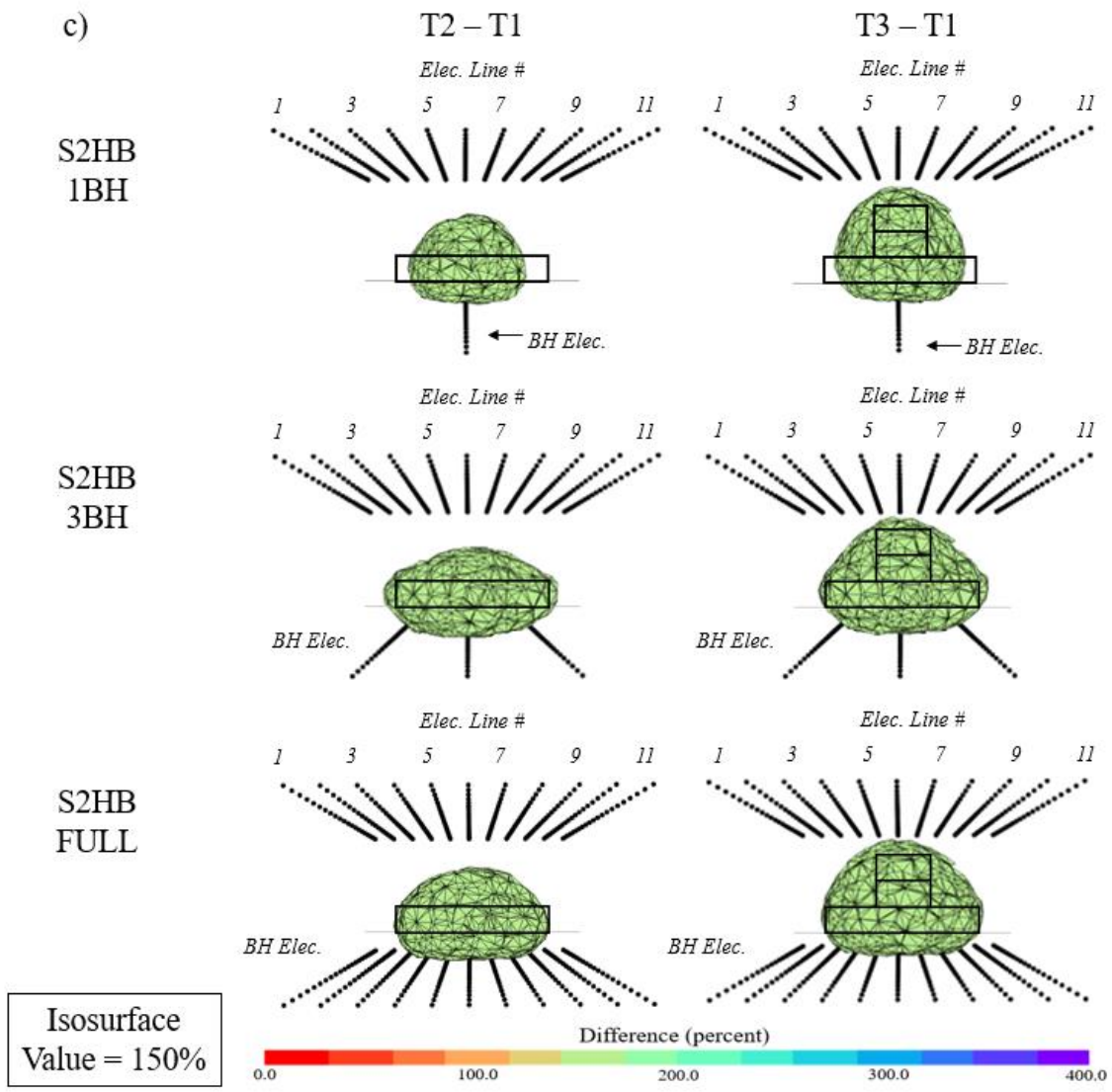
c)
T2 – T1
T3 – T1
S2HB 1BH
S2HB 3BH
S2HB FULL
Elec. Line #
1 3 5 7 9 11
BH Elec.
Isosurface Value = 150%
Difference (percent)
0.0
100.0
200.0
300.0
400.0

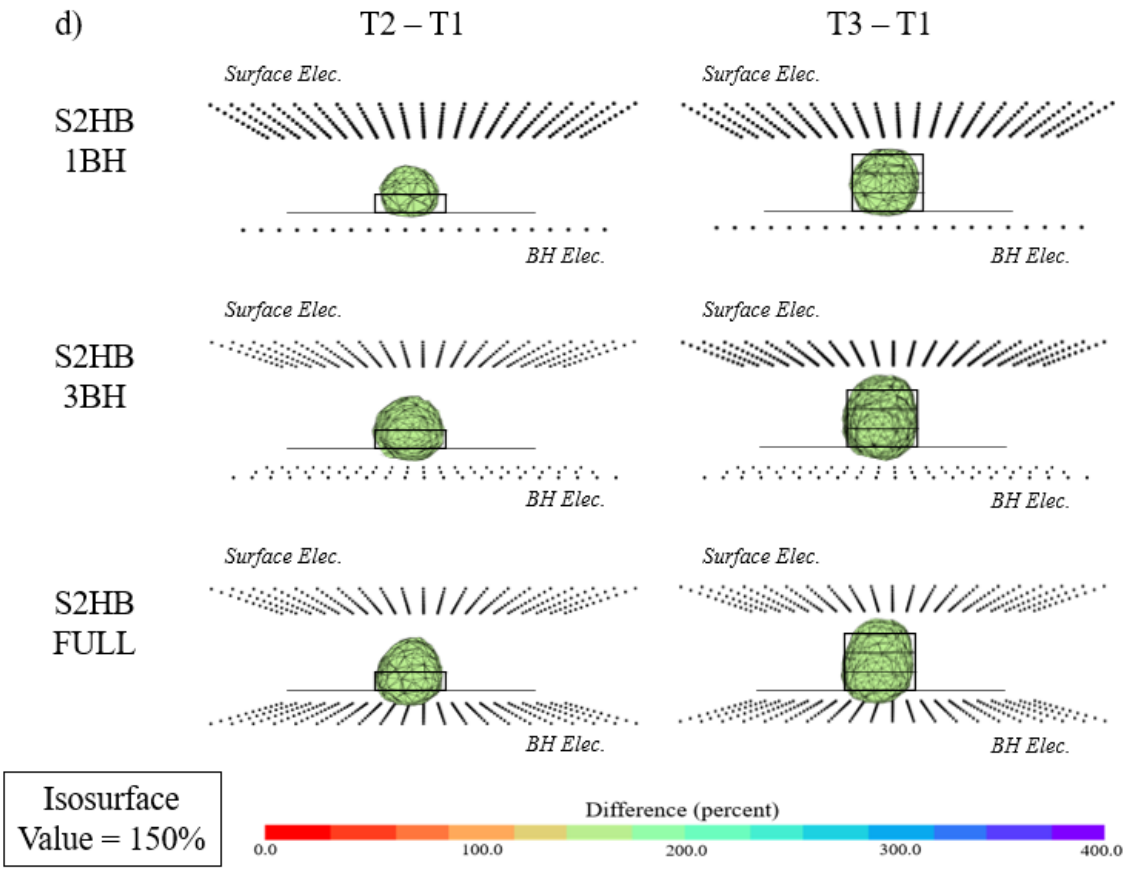
d)
T2 – T1
T3 – T1
S2HB 1BH
S2HB 3BH
S2HB FULL
Surface Elec.
BH Elec.
Isosurface Value = 150%
Difference (percent)
0.0
100.0
200.0
300.0
400.0

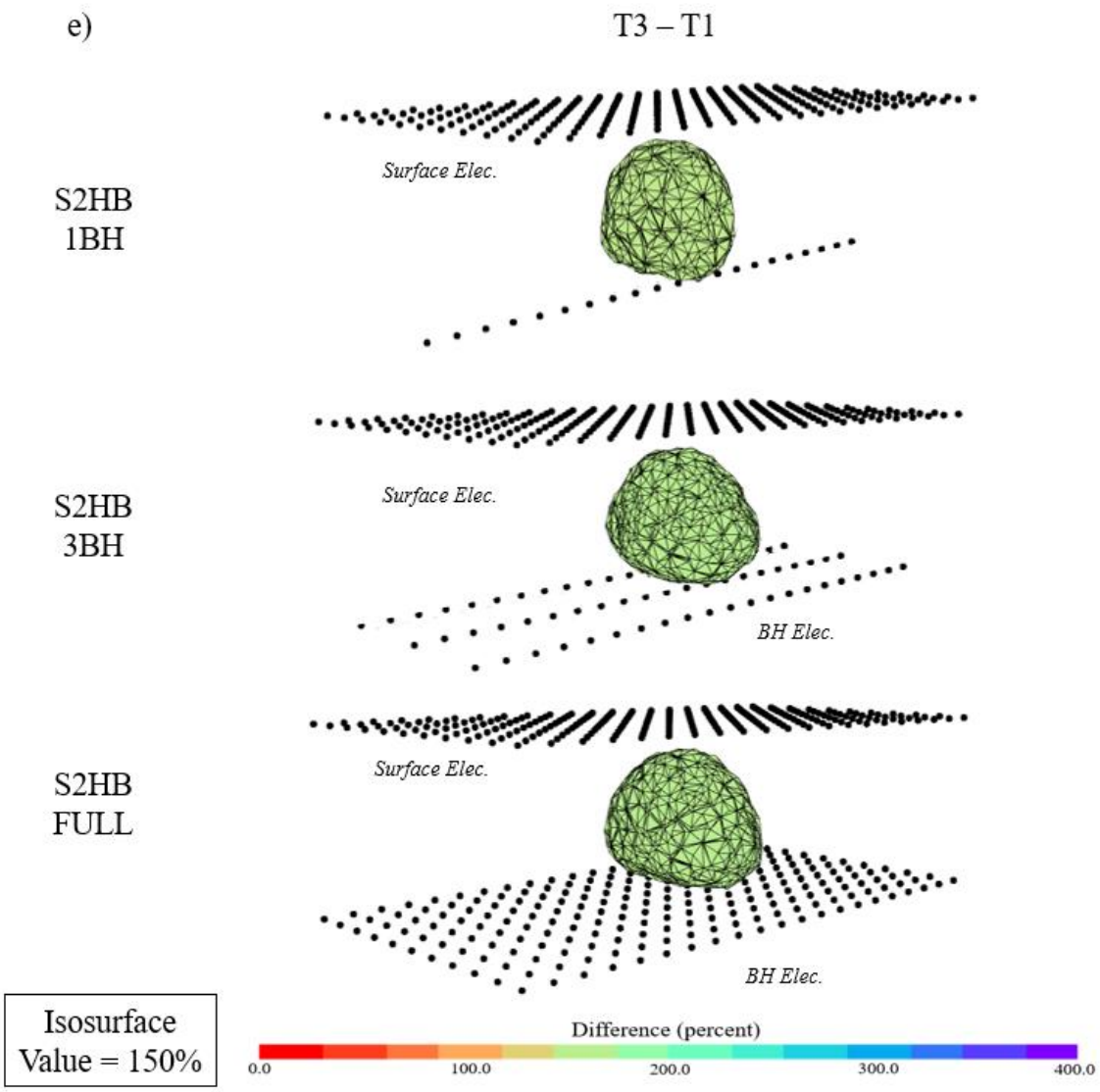

Figure 3-13: Water and plastic experiment results from S2HB-1BH, S2HB-3BH and S2HB-FULL imaging of Inverted-T: (a) cross-sectional slices of the inverted 3D resistivity domain at time-steps T1, T2 and T3, (b) cross-sectional slices of the difference (%) images between T1 and T2, and T1 and T3, (c) front view of the 3D isovolume differences (75%), (d) side view of the 3D isovolume differences (75%), and (e) oblique view of 3D isovolume differences (75%).

Standard-T Target

This section further assesses the performance of S2HB-1BH relative to S2HB-FULL on the Standard-T target in water and plastic experiments. Due to this target geometry, with the horizontal portion being shallower, surface ERT is also included to assess whether any S2HB configuration still has superior performance even on shallower targets.

Figure 3-14 presents the respective resistivity, difference, and 3D isovolume images at the three time-steps. It is evident that S2HB-1BH provides similar images to S2HB-FULL of this target, with both providing superior results to surface ERT. For example, during time-step T2, S2HB-1BH and S2HB-FULL were able to resolve the bottom portion of the target with similar accuracy, whereas surface ERT was unable to resolve it. In T3, surface ERT was now able to resolve the top horizontal portion of the target with similar ability to S2HB-1BH and S2HB-FULL; however, it remains inadequate for resolving the complete Standard-T target.

Due to the geometry of this target and the respective sensitivity of each configuration, the results match expectations. While S2HB-FULL exhibits the most sensitivity over the entire experimental domain, S2HB-1BH has its most sensitive areas where the Standard-T target is located (see Figure 3-2). Therefore, S2HB-1BH was able to provide similar images. The shallow high sensitivity areas of surface ERT coincide with the now shallow horizontal portion of the target, which it is able to resolve. However, the limited depth resolution is still evident as it completely underestimates, or even misses, the lower portion of the target.

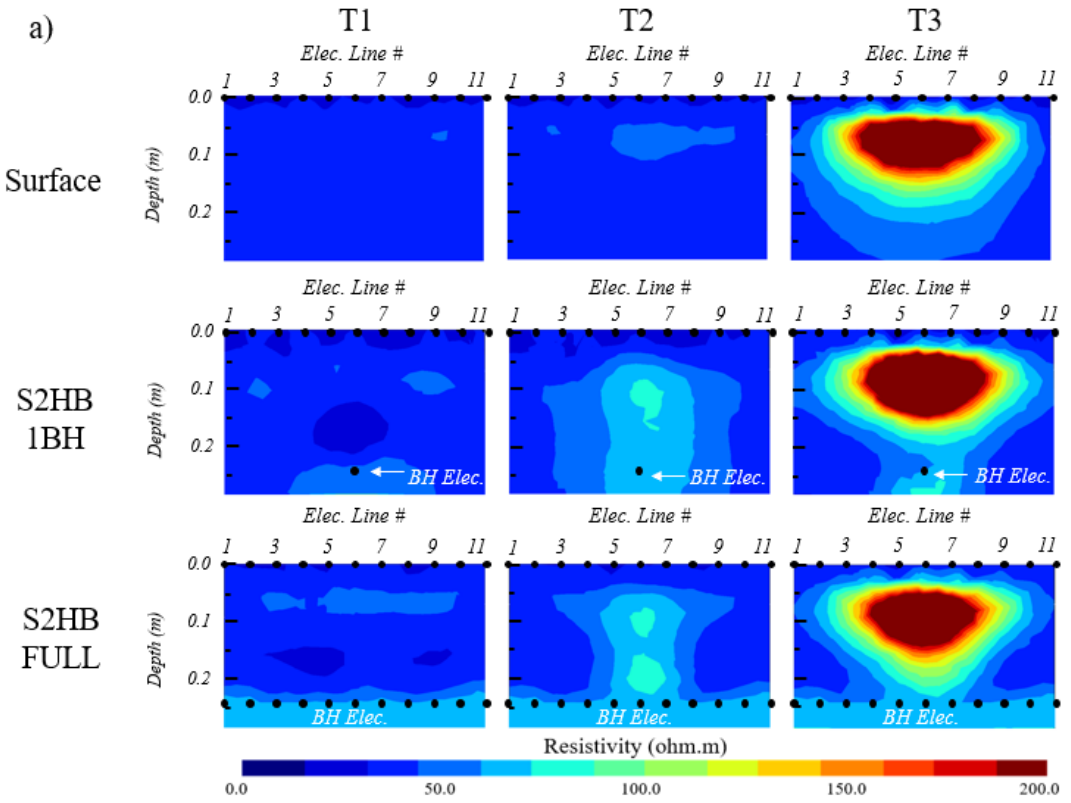
a)
T1
T2
T3
Elec. Line #
1 3 5 7 9 11
Surface
S2HB 1BH
S2HB FULL
Depth (m)
0.0
0.1
0.2
BH Elec.
Resistivity (ohm.m)
0.0
50.0
100.0
150.0
200.0

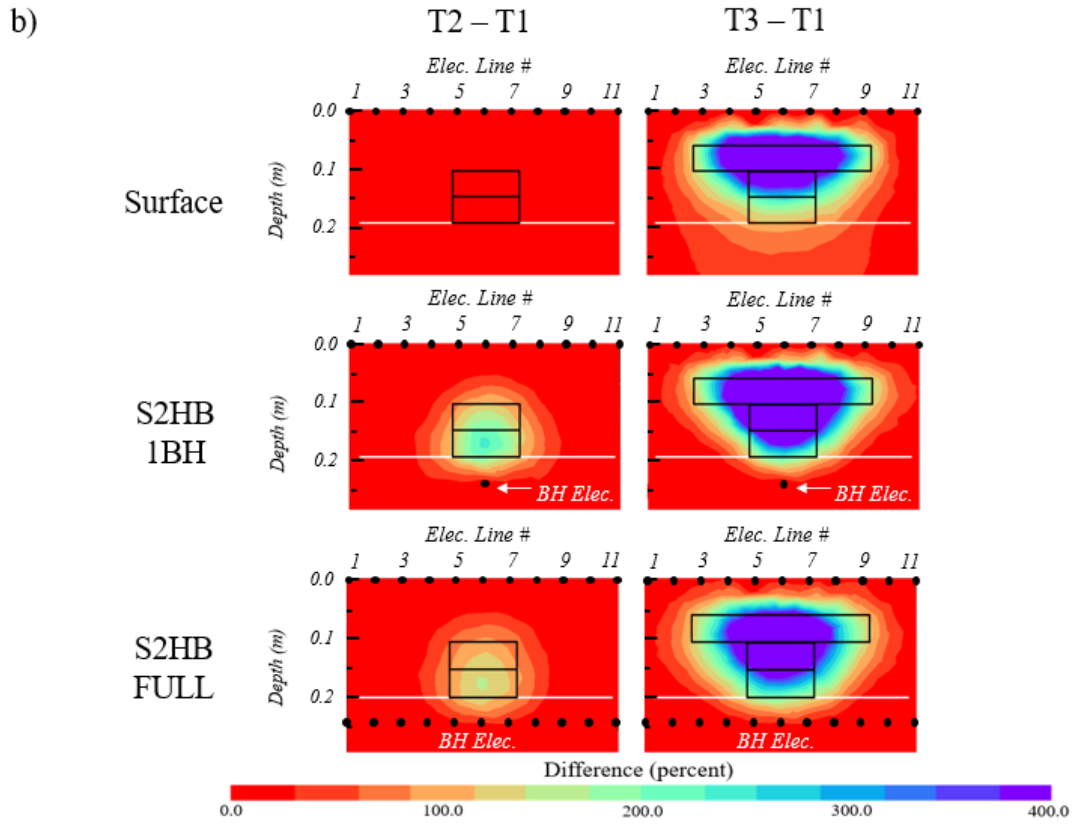
b)
T2 – T1
T3 – T1
Elec. Line #
1 3 5 7 9 11
Surface
S2HB 1BH
S2HB FULL
Depth (m)
0.0
0.1
0.2
BH Elec.
Difference (percent)
0.0
100.0
200.0
300.0
400.0

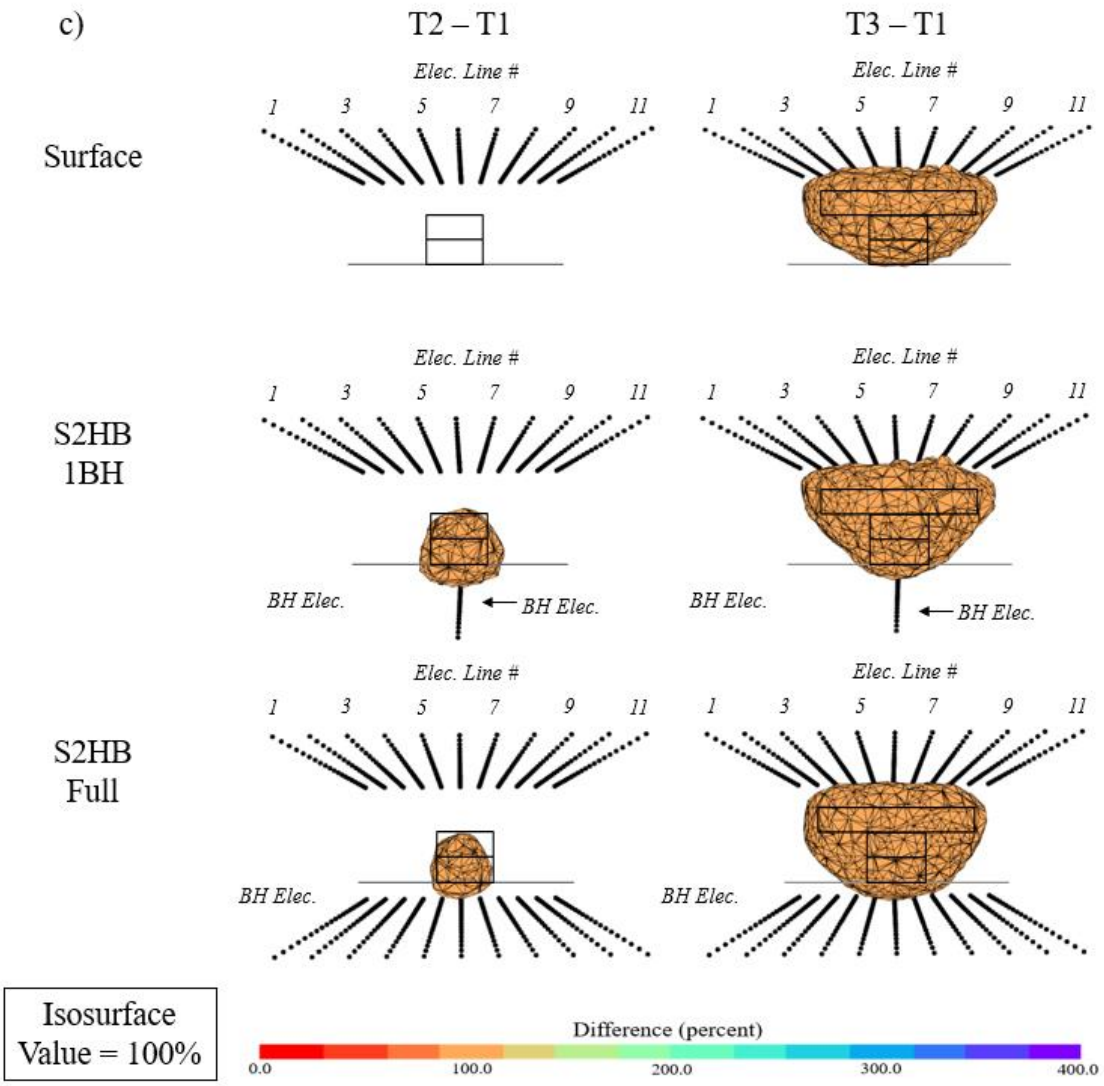
c)
T2 – T1
T3 – T1
Surface
S2HB
1BH
S2HB
Full
Elec. Line #
1
3
5
7
9
11
BH Elec.
Isosurface
Value = 100%
Difference (percent)
0.0
100.0
200.0
300.0
400.0

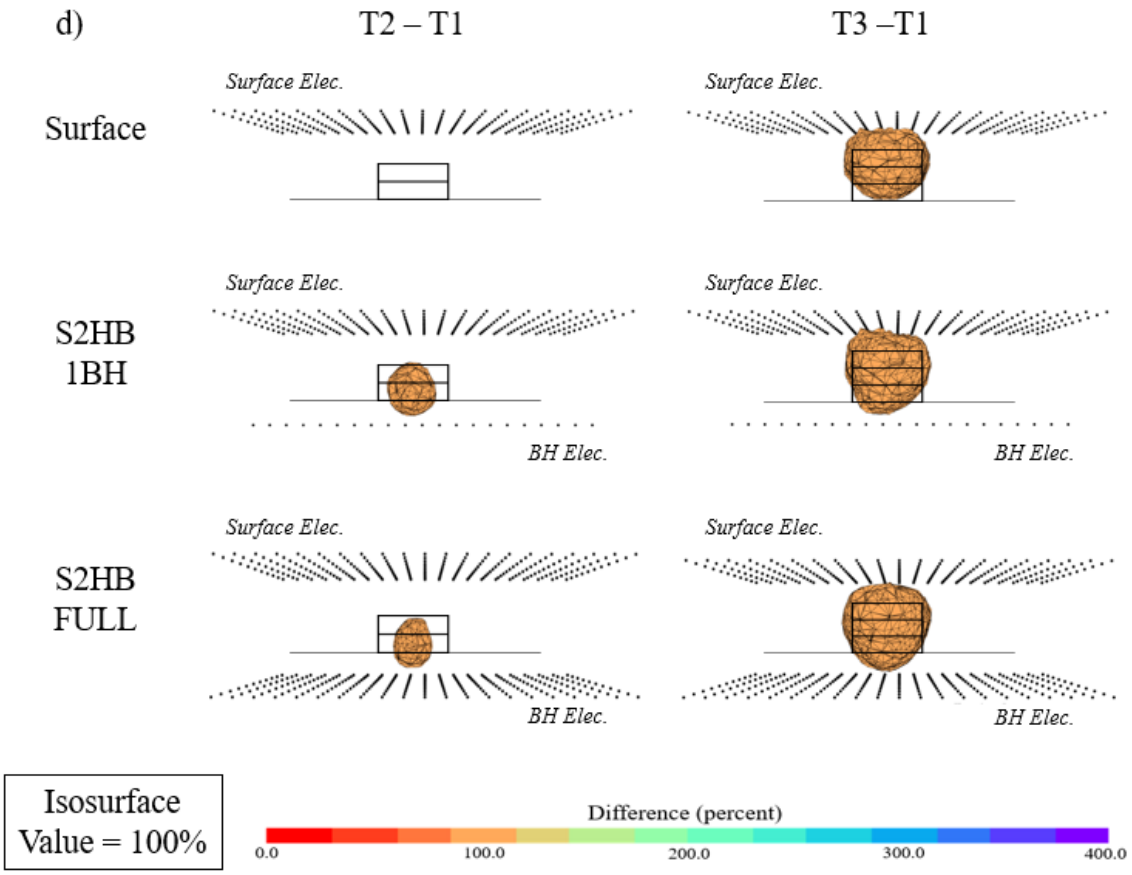
d)
T2 – T1
T3 –T1
Surface
S2HB
1BH
S2HB
FULL
Surface Elec.
BH Elec.
Isosurface
Value = 100%
Difference (percent)
0.0
100.0
200.0
300.0
400.0

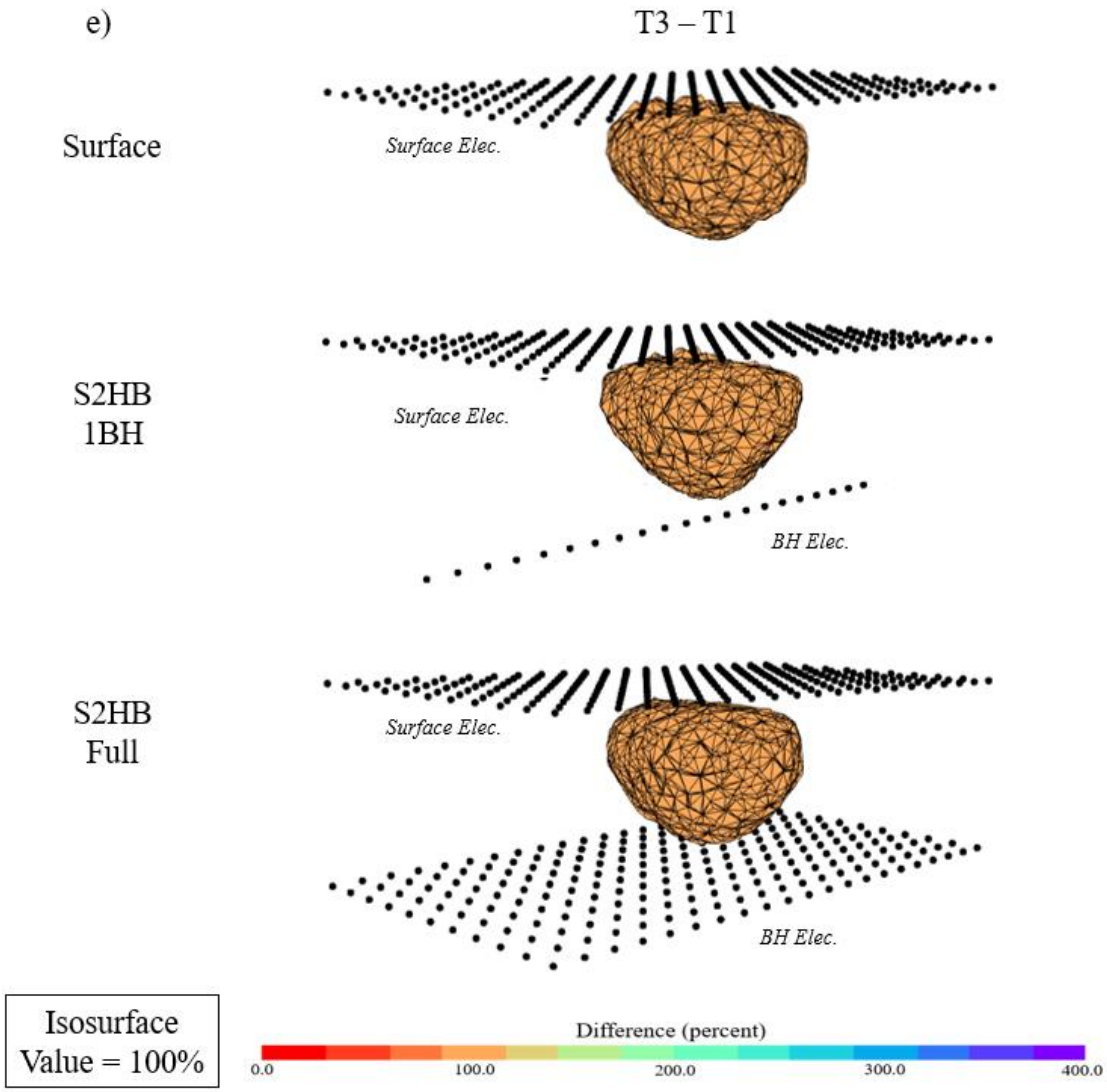

Figure 3-14: Water and plastic experiment results from S2HB-1BH and S2HB-FULL imaging of Standard-T: (a) cross-sectional slices of the inverted 3D resistivity domain at time-steps T1, T2 and T3, (b) cross-sectional slices of the difference (%) images between T1 and T2, and T1 and T3, (c) front view of the 3D isovolume differences (75%), (d) side view of the 3D isovolume differences (75%), and (e) oblique view of 3D isovolume differences (75%).

3.4 Conclusions

In this study, the potential of 3D surface-to-horizontal borehole (S2HB) ERT was evaluated for improved imaging of sites contaminated by DNAPLs. Traditional ERT imaging deploys electrodes along the surface, and while it is more convenient and requires less effort, it may not always accurately represent the subsurface features and processes due to its decreasing resolution with depth. This is particularly problematic for imaging DNAPL source zones as they are characterized by highly complex and heterogeneous distributions and can be located at large depths. S2HB ERT has exhibited significant potential for improved image resolution at depth with the deployment of a horizontal borehole line of electrodes below the target; however, it has only been used in 2D. Three-dimensional imaging is required to characterize DNAPL source zones at field sites.

A suite of numerical simulations and laboratory tank experiments were conducted to investigate 3D S2HB ERT performance relative to surface ERT on different 3D resistive targets within more conductive backgrounds. Different electrode configurations for 3D S2HB ERT were proposed, with the respective implementation of one borehole, three boreholes and all boreholes. As a single horizontal borehole is more realistic and practical to implement at field sites, the main 3D S2HB ERT configuration proposed in this study consists of a 2D surface grid of electrodes overlying one borehole (i.e., S2HB-1BH ERT). S2HB-1BH ERT imaging of a subsurface T-shaped target (i.e., Inverted-T) was first assessed relative to traditional surface ERT. The target was separated into sub-targets, thereby providing multiple targets to image and allow time-lapse monitoring of changes between sub-targets.

Results of all simulations and experiments demonstrate highly superior imaging of targets and changes with S2HB-1BH ERT relative to surface ERT, particularly at depth. Further analysis of S2HB-1BH ERT was performed with (i) increasing depth of borehole, and (ii) addition of more horizontal boreholes. Results demonstrate that increasing the depth to the horizontal borehole from six times the electrode spacing (0.24 m) to eight times (0.32 m) diminished the performance of S2HB-1BH, but it was still able to moderately resolve the target while surface ERT was now unable to resolve any portion of the target. Comparative analysis of S2HB-1BH with S2HB configurations utilizing three boreholes (S2HB-3BH)

and the same number of boreholes as surface lines (S2HB-FULL) demonstrated that while imaging slightly improved with increasing borehole numbers, S2HB-1BH still provided highly comparable results to S2HB-3BH and S2HB-FULL.

Due to both its performance and more practical implementation, this study suggests that 3D S2HB-1BH ERT can bring superior characterization and monitoring capabilities to DNAPL field sites. While the focus of this study was on DNAPL investigations, the findings of this study are applicable to a range of contaminants, features and processes within the subsurface.

3.5 References

Bing, Z., & Greenhalgh, S. A. (2000). Cross-hole resistivity tomography using different electrode configurations. In *Geophysical Prospecting* (Vol. 48).

Binley, A., Hubbard, S., Huisman, J., Revil, A., Robinson, D., Singha, K., & Slater, L. (2015). The emergence of hydrogeophysics for improved understanding of subsurface processes over multiple scales _ Enhanced Reader. *Water Resources Reseach, 51*.

Blanchy, G., Saneiyan, S., Boyd, J., McLachlan, P., & Binley, A. (2020). ResIPy, an intuitive open source software for complex geoelectrical inversion/modeling. *Computers and Geosciences*, *137*. https://doi.org/10.1016/j.cageo.2020.104423

Boyd, J., Saneiyan, S., & Mclachlan, P. (2019). *3D Geoelectrical Problems With ResiPy, an Open Source Graphical User Interface for Geoelectrical Data Processing*. https://doi.org/10.13140/RG.2.2.35381.63205

Brewster, M., Annan, A., Greenhouse, J., Kueper, B., Olhoeft, G., Redman, J., & Sander, K. (1995). *Observed Migration of a Controlled DNAPL Release by Geophysical Methods*.

Cardarelli, E., & di Filippo, G. (2009). Electrical resistivity and induced polarization tomography in identifying the plume of chlorinated hydrocarbons in sedimentary formation: A case study in Rho (Milan - Italy). *Waste Management and Research*, *27*(6), 595–602. https://doi.org/10.1177/0734242X09102524

Chambers, J. E., Wilkinson, P. B., Wealthall, G. P., Loke, M. H., Dearden, R., Wilson, R., Allen, D., & Ogilvy, R. D. (2010a). Hydrogeophysical imaging of deposit heterogeneity and groundwater chemistry changes during DNAPL source zone bioremediation. *Journal of Contaminant Hydrology*, *118*(1–2), 43–61. https://doi.org/10.1016/j.jconhyd.2010.07.001

Cohen, R., & Mercer, J. (1993). DNAPL Site Evaluation. *GeoTrans, Inc.*

Danielsen, B. E., & Dahlin, T. (2010). Numerical modeling of resolution and sensitivity of ERT in horizontal boreholes. *Journal of Applied Geophysics*, *70*(3), 245–254. https://doi.org/10.1016/j.jappgeo.2010.01.005

Deng, Y., Shi, X., Xu, H., Sun, Y., Wu, J., & Revil, A. (2017). Quantitative assessment of electrical resistivity tomography for monitoring DNAPLs migration – Comparison with high-resolution light transmission visualization in laboratory sandbox. *Journal of Hydrology*, *544*, 254–266. https://doi.org/10.1016/j.jhydrol.2016.11.036

Dhu, T., & Heinson, G. (2004). Numerical and laboratory investigations of electrical resistance tomography for environmental monitoring. *Exploration Geophysics*, *35*(1), 33–40. https://doi.org/10.1071/EG04033

Folch, A., del Val, L., Luquot, L., Martínez-Pérez, L., Bellmunt, F., le Lay, H., Rodellas, V., Ferrer, N., Palacios, A., Fernández, S., Marazuela, M. A., Diego-Feliu, M., Pool, M., Goyetche, T., Ledo, J., Pezard, P., Bour, O., Queralt, P., Marcuello, A., … Carrera, J. (2020). Combining fiber optic DTS, cross-hole ERT and time-lapse induction logging to characterize and monitor a coastal aquifer. *Journal of Hydrology*, *588*. https://doi.org/10.1016/j.jhydrol.2020.125050

Forquet, N., & French, H. K. (2012). Application of 2D surface ERT to on-site wastewater treatment survey. *Journal of Applied Geophysics*, *80*, 144–150. https://doi.org/10.1016/j.jappgeo.2012.02.002

Goes, B. J. M., & Meekes, J. A. C. (2004). An effective electrode configuration for the detection of DNAPLs with electrical resistivity tomography. *Journal of Environmental and Engineering Geophysics*, *9*(3), 127–141. https://doi.org/10.4133/JEEG9.3.127

Griffin, T., & Watson, K. (2002). *A Comparison of Field Techniques for Confirming Dense Nonaqueous Phase Liquids*.

Kang, X., Kokkinaki, A., Kitanidis, P. K., Shi, X., Revil, A., Lee, J., Soueid Ahmed, A., & Wu, J. (2020). Improved Characterization of DNAPL Source Zones via Sequential

Hydrogeophysical Inversion of Hydraulic-Head, Self-Potential and Partitioning Tracer Data. *Water Resources Research*, *56*(8). https://doi.org/10.1029/2020WR027627

Kang, X., Kokkinaki, A., Power, C., Kitanidis, P. K., Shi, X., Duan, L., Liu, T., & Wu, J. (2021). Integrating deep learning-based data assimilation and hydrogeophysical data for improved monitoring of DNAPL source zones during remediation. *Journal of Hydrology*, *601*. https://doi.org/10.1016/j.jhydrol.2021.126655

Karaoglu, A. G., Copty, N. K., Akyol, N. H., Kilavuz, S. A., & Babaei, M. (2019). Experiments and sensitivity coefficients analysis for multiphase flow model calibration of enhanced DNAPL dissolution. *Journal of Contaminant Hydrology*, *225*. https://doi.org/10.1016/j.jconhyd.2019.103515

Karaoulis, M., Revil, A., Tsourlos, P., Werkema, D. D., & Minsley, B. J. (2013). IP4DI: A software for time-lapse 2D/3D DC-resistivity and induced polarization tomography. *Computers and Geosciences*, *54*, 164–170. https://doi.org/10.1016/j.cageo.2013.01.008

Kiflu, H., Kruse, S., Loke, M. H., Wilkinson, P. B., & Harro, D. (2016). Improving resistivity survey resolution at sites with limited spatial extent using buried electrode arrays. *Journal of Applied Geophysics*, *135*, 338–355. https://doi.org/10.1016/j.jappgeo.2016.10.011

Kim, J.H., M.J. Yi, S.G. Park, and J.G. Kim. 2009. 4-D inversion of DC resistivity monitoring data acquired over a dynamically changing earth model. Journal of Applied Geophysics, 68: 522-532.

Kim, J.H., R. Supper, P. Tsourlos, and M.J. Yi. 2013. Four-dimensional inversion of resistivity monitoring data through Lp norm minimizations. Geophysical Journal International, 195(3): 1640-1656.

Koohbor, B., Deparis, J., Leroy, P., Ataie-Ashtiani, B., Davarzani, H., & Colombano, S. (2022). DNAPL flow and complex electrical resistivity evolution in saturated porous media: A coupled numerical simulation. *Journal of Contaminant Hydrology*, *248*. https://doi.org/10.1016/j.jconhyd.2022.104003

Kueper, B. H., & Great Britain. Environment Agency. (2004). *An illustrated handbook of DNAPL transport and fate in the subsurface*. Environment Agency.

Loke, M. H., Chambers, J. E., Rucker, D. F., Kuras, O., & Wilkinson, P. B. (2013). Recent developments in the direct-current geoelectrical imaging method. *Journal of Applied Geophysics*, *95*, 135–156. https://doi.org/10.1016/j.jappgeo.2013.02.017

Loke, Meng & Wilkinson, P.B. & Kuras, Oliver. (2021). The Use of a Semi-Structured Finite-Element Mesh in 3-D Resistivity Inversion. 1-5. 10.3997/2214-4609.202177021.

Lucius1, J. E., Olhoeft1, G. R., Hill1, P. L., & Duke2, S. K. (1992). *PROPERTIES AND HAZARDS OF 108 SELECTED SUBSTANCES-1992 EDITION*.

Martorana, R., Capizzi, P., D'Alessandro, A., & Luzio, D. (2017). Comparison of different sets of array configurations for multichannel 2D ERT acquisition. *Journal of Applied Geophysics*, *137*, 34–48. https://doi.org/10.1016/j.jappgeo.2016.12.012

McMillan, L. A., Rivett, M. O., Wealthall, G. P., Zeeb, P., & Dumble, P. (2018). Monitoring well utility in a heterogeneous DNAPL source zone area: Insights from proximal multilevel sampler wells and sampling capture-zone modeling. *Journal of Contaminant Hydrology*, *210*, 15–30. https://doi.org/10.1016/j.jconhyd.2018.02.001

Mohammed Nazifi, H., Gülen, L., Gürbüz, E., & Pekşen, E. (2022). Time-lapse electrical resistivity tomography (ERT) monitoring of used engine oil contamination in laboratory setting. *Journal of Applied Geophysics*, *197*. https://doi.org/10.1016/j.jappgeo.2022.104531

Ochs, J., Klitzsch, N., & Wagner, F. M. (2022). Mitigation of installation-related effects for small-scale borehole-to-surface ERT. *Journal of Applied Geophysics*, *197*. https://doi.org/10.1016/j.jappgeo.2022.104530

Orlando, L., & Renzi, B. (2015). Electrical permittivity and resistivity time lapses of multiphase DNAPLs in a lab test. *Water Resources Research*, *51*(1), 377–389. https://doi.org/10.1002/2014WR015291

Pankow, J. F., & Cherry, J. A. (1996). *DENSE CHLORINATED SOLVENTS and other DNAPLs in Groundwater: History, Behavior, and Remediation*.

Power, C., Gerhard, J. I., Karaoulis, M., Tsourlos, P., & Giannopoulos, A. (2014). Evaluating four-dimensional time-lapse electrical resistivity tomography for monitoring DNAPL source zone remediation. *Journal of Contaminant Hydrology*, *162–163*, 27–46. https://doi.org/10.1016/j.jconhyd.2014.04.004

Power, C., Gerhard, J. I., Tsourlos, P., Soupios, P., Simyrdanis, K., & Karaoulis, M. (2015). Improved time-lapse electrical resistivity tomography monitoring of dense non-aqueous phase liquids with surface-to-horizontal borehole arrays. *Journal of Applied Geophysics*, *112*, 1–13. https://doi.org/10.1016/j.jappgeo.2014.10.022

Power, C., Tsourlos, P., Ramasamy, M., Nivorlis, A., & Mkandawire, M. (2018). Combined DC resistivity and induced polarization (DC-IP) for mapping the internal composition of a mine waste rock pile in Nova Scotia, Canada. *Journal of Applied Geophysics*, *150*, 40–51. https://doi.org/10.1016/j.jappgeo.2018.01.009

Revil, A., Karaoulis, M., Johnson, T., & Kemna, A. (2012). Review: Some low-frequency electrical methods for subsurface characterization and monitoring in hydrogeology. *Hydrogeology Journal*, *20*(4), 617–658. https://doi.org/10.1007/s10040-011-0819-x

Simyrdanis, K., Tsourlos, P., Soupios, P., Tsokas, G., Kim, J. H., & Papadopoulos, N. (2015). Surface-to-tunnel electrical resistance tomography measurements. *Near Surface Geophysics*, *13*(4), 343–354. https://doi.org/10.3997/1873-0604.2015019

Slater, L., & Binley, A. (2021). Advancing hydrological process understanding from long-term resistivity monitoring systems. In *Wiley Interdisciplinary Reviews: Water* (Vol. 8, Issue 3). John Wiley and Sons Inc. https://doi.org/10.1002/wat2.1513

Soga, K., Page, J. W. E., & Illangasekare, T. H. (2004). A review of NAPL source zone remediation efficiency and the mass flux approach. *Journal of Hazardous Materials*, *110*(1–3), 13–27. https://doi.org/10.1016/j.jhazmat.2004.02.034

Trento, L. M., Tsourlos, P., & Gerhard, J. I. (2021). Time-lapse electrical resistivity tomography mapping of DNAPL remediation at a STAR field site. *Journal of Applied Geophysics*, *184*. https://doi.org/10.1016/j.jappgeo.2020.104244

Tsourlos, P. (1995). *Modeling, Interpretation and Inversion of Multielectrode Resistivity Survey Data*.

van Schoor, M., & Binley, A. (2010). *In-mine (tunnel-to-tunnel) electrical resistance 1 tomography in South African platinum mines*

von Bülow, R., Klitzsch, N., & Wellmann, F. (2021). Strategies to overcome near surface disturbances while inverting time-lapse surface ERT data. *Journal of Applied Geophysics*, *195*. https://doi.org/10.1016/j.jappgeo.2021.104463

Wang, H., Lin, C. P., & Liu, H. C. (2020). Pitfalls and refinement of 2D cross-hole electrical resistivity tomography. *Journal of Applied Geophysics*, *181*. https://doi.org/10.1016/j.jappgeo.2020.104143

Zou, C., & Zhang, S. (2022). Precise estimation of subsurface moisture content based on laboratory measurement and 3D GPR field survey. *Journal of Applied Geophysics*, 104752. https://doi.org/10.1016/j.jappgeo.2022.104752

Chapter 4

4 Conclusion

4.1 Summary

The remediation of sites contaminated with DNAPLs remains a major environmental issue (Yang et al., 2022). DNAPL source zones can act as a long-term source of groundwater contamination causing adverse effects to the ecosystem (Kueper et al., 2004). Successfully remediation of DNAPL sites requires accurate characterization of the subsurface to determine appropriate remediation strategies (Guo et al., 2021).

ERT is a non-destructive subsurface characterization technique that has become increasingly widespread (e.g., Binley et al., 2015; Deng et al., 2017; Trento et al., 2021; Zou et al., 2022;). However, ERT studies generally employ surface electrode configurations (e.g., Dahlin and Zhou, 2004; Loke et al., 2013) which are limited due to loss of resolution with depth (Folch et al., 2020; Wang et al., 2020). Additional studies have been completed using horizontal borehole and tunnel ERT (e.g., Danielsen and Dahlin., 2010; Simyrdanis et al., 2015; Power et al., 2015). These studies have demonstrated the potential of applying electrodes in horizontal boreholes to improve target characterization with depth. However, these studies were only completed in two dimensions.

The goal of this thesis was to study the potential of 3D S2HB ERT for the purpose of characterizing DNAPL source zones. Many S2HB ERT simulations and experiments were completed that utilized different electrode configurations and target shapes to demonstrate the improved characterization of 3D S2HB ERT.

To achieve this research goal, two sub-objectives were addressed. The first was to demonstrate the potential of the 3D S2HB 1BH configuration in comparison to conventional 3D surface ERT. The S2HB 1BH configuration was chosen for this objective because it is the most practical S2HB configuration to implement on a site. The results of these configurations were analyzed and compared using numerical models, water and plastic experiments, and sand and NAPL experiments for an Inverted-T target. These

results indicated improved characterization of the target extents vertically and laterally with depth for the S2HB 1BH configuration in comparison to conventional 3D surface ERT.

The second objective was to perform a sensitivity analysis of numerous 3D S2HB configurations. This included additional analysis of the S2HB 1BH configuration and analysis of the S2HB FULL and S2HB 3BH configurations. These experiments were comprised of Standard-T and Inverted-T targets at various depths and were completed using water and plastic. Analysis of these experiments suggested that the target characterization improved as the number of borehole electrode lines increased. The results also suggested that a reduced number of borehole electrode lines were required to characterize the subsurface to the same quality as the S2HB Full configuration depending on the target shape. This was demonstrated in the Inverted-T experiment by the S2HB 3BH and S2HB Full results having very similar target characterization. This was also demonstrated for the Standard-T experiment in which the S2HB 1BH and S2HB FULL results had very similar target characterization. Furthermore, the results demonstrated that the S2HB 1BH configuration could provide comparable results to the S2HB Full and S2HB 3BH configurations even for targets located in the low sensitivity area of the S2HB 1BH configuration. The results also demonstrated that when the target depth is increased to a depth unable for conventional 3D surface ERT to resolve entirely, the S2HB 1BH configuration can still characterize the target to a reasonable extent.

4.2 Recommendations

The following recommendations are suggested for advancing 3D S2HB ERT in to contaminated sites:

- Apply S2HB ERT to a pilot test in the field. Currently, S2HB ERT in three-dimensions has only been applied at a laboratory scale. It is necessary to demonstrate DNAPL source zone characterization potential of 3D S2HB ERT at a field scale to advance the technology to DNAPL sites.

- Design an optimal method for installing electrodes into horizontal boreholes at a field scale. It is generally straight forward to install horizontal borehole electrodes in an

experiment tank and apply electrodes to the ground surface in the field, however there is no established method of installing horizontal borehole electrodes in the field at depths that are not easily accessible.

- Apply S2HB ERT to contaminants beyond DNAPLs. Contaminants such as acid mine drainage and road salts can cause extensive environmental damage if not managed properly. S2HB ERT could be applied to such contaminants to help develop remediation strategies.

4.3 References

Binley, A., Hubbard, S., Huisman, J., Revil, A., Robinson, D., Singha, K., & Slater, L. (2015). The emergence of hydrogeophysics for improved understanding of subsurface processes over multiple scales _ Enhanced Reader. *Water Resources Reseach*, *51*.

Dahlin, T., & Zhou, B. (2004). A numerical comparison of 2D resistivity imaging with 10 electrode arrays. *Geophysical Prospecting*, *52*(5), 379–398. https://doi.org/10.1111/j.1365-2478.2004.00423.x

Danielsen, B. E., & Dahlin, T. (2010). Numerical modeling of resolution and sensitivity of ERT in horizontal boreholes. *Journal of Applied Geophysics*, *70*(3), 245–254. https://doi.org/10.1016/j.jappgeo.2010.01.005

Deng, Y., Shi, X., Xu, H., Sun, Y., Wu, J., & Revil, A. (2017). Quantitative assessment of electrical resistivity tomography for monitoring DNAPLs migration – Comparison with high-resolution light transmission visualization in laboratory sandbox. *Journal of Hydrology*, *544*, 254–266. https://doi.org/10.1016/j.jhydrol.2016.11.036

Folch, A., del Val, L., Luquot, L., Martínez-Pérez, L., Bellmunt, F., le Lay, H., Rodellas, V., Ferrer, N., Palacios, A., Fernández, S., Marazuela, M. A., Diego-Feliu, M., Pool, M., Goyetche, T., Ledo, J., Pezard, P., Bour, O., Queralt, P., Marcuello, A., … Carrera, J. (2020). Combining fiber optic DTS, cross-hole ERT and time-lapse induction logging to characterize and monitor a coastal aquifer. *Journal of Hydrology*, *588*. https://doi.org/10.1016/j.jhydrol.2020.125050

Guo, Q., Shi, X., Kang, X., Hao, S., Liu, L., & Wu, J. (2021). Evaluation of the benefits of improved permeability estimation on high-resolution characterization of DNAPL distribution in aquifers with low-permeability lenses. *Journal of Hydrology*, *603*. https://doi.org/10.1016/j.jhydrol.2021.126955

Kueper, B. H., & Great Britain. Environment Agency. (2004). *An illustrated handbook of DNAPL transport and fate in the subsurface*. Environment Agency.

Loke, M. H., Chambers, J. E., Rucker, D. F., Kuras, O., & Wilkinson, P. B. (2013). Recent developments in the direct-current geoelectrical imaging method. *Journal of Applied Geophysics*, *95*, 135–156. https://doi.org/10.1016/j.jappgeo.2013.02.017

Power, C., Gerhard, J. I., Tsourlos, P., Soupios, P., Simyrdanis, K., & Karaoulis, M. (2015). Improved time-lapse electrical resistivity tomography monitoring of dense non-aqueous phase liquids with surface-to-horizontal borehole arrays. *Journal of Applied Geophysics*, *112*, 1–13. https://doi.org/10.1016/j.jappgeo.2014.10.022

Simyrdanis, K., Tsourlos, P., Soupios, P., Tsokas, G., Kim, J. H., & Papadopoulos, N. (2015). Surface-to-tunnel electrical resistance tomography measurements. *Near Surface Geophysics*, *13*(4), 343–354. https://doi.org/10.3997/1873-0604.2015019

Trento, L. M., Tsourlos, P., & Gerhard, J. I. (2021). Time-lapse electrical resistivity tomography mapping of DNAPL remediation at a STAR field site. *Journal of Applied Geophysics*, *184*. https://doi.org/10.1016/j.jappgeo.2020.104244

Wang, H., Lin, C. P., & Liu, H. C. (2020). Pitfalls and refinement of 2D cross-hole electrical resistivity tomography. *Journal of Applied Geophysics*, *181*. https://doi.org/10.1016/j.jappgeo.2020.104143

Yang, P., Guo, H., Wang, Z., & Zhao, E. (2022). Influence of distribution characteristics of residual DNAPL on mass transfer in porous media under ethanol co-solvent flushing. *Journal of Hydrology, 610*. https://doi.org/10.1016/j.jhydrol.2022.127932

Zou, C., & Zhang, S. (2022). Precise estimation of subsurface moisture content based on laboratory measurement and 3D GPR field survey. *Journal of Applied Geophysics*, 104752. https://doi.org/10.1016/j.jappgeo.2022.104752

Appendix A: Additional Numerical Modeling

Appendix A presents additional numerical modeling results from the Inverted-T shaped target using the S2HB-FULL, S2HB-3BH, and S2HB-1BH ERT configurations.

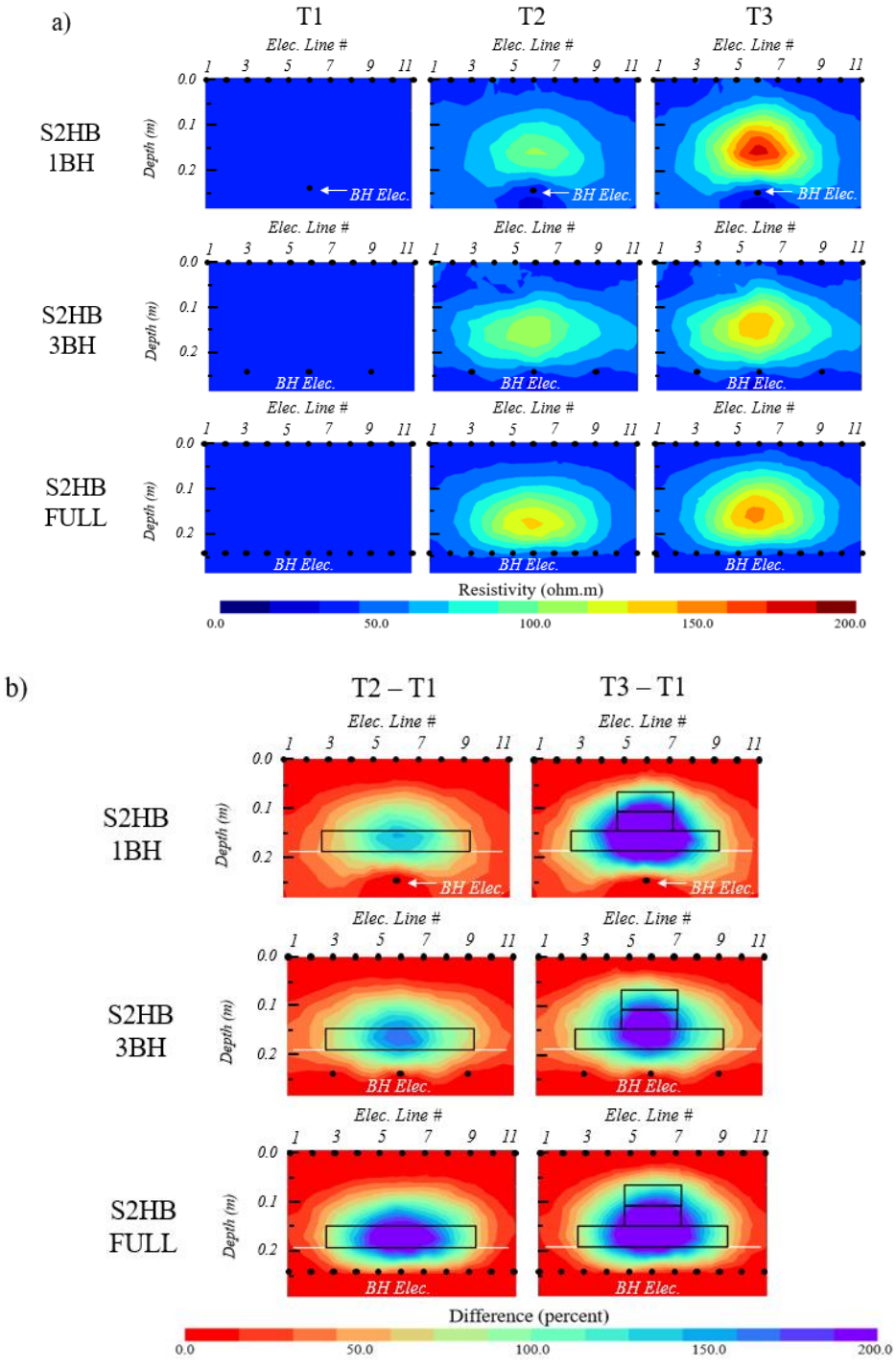

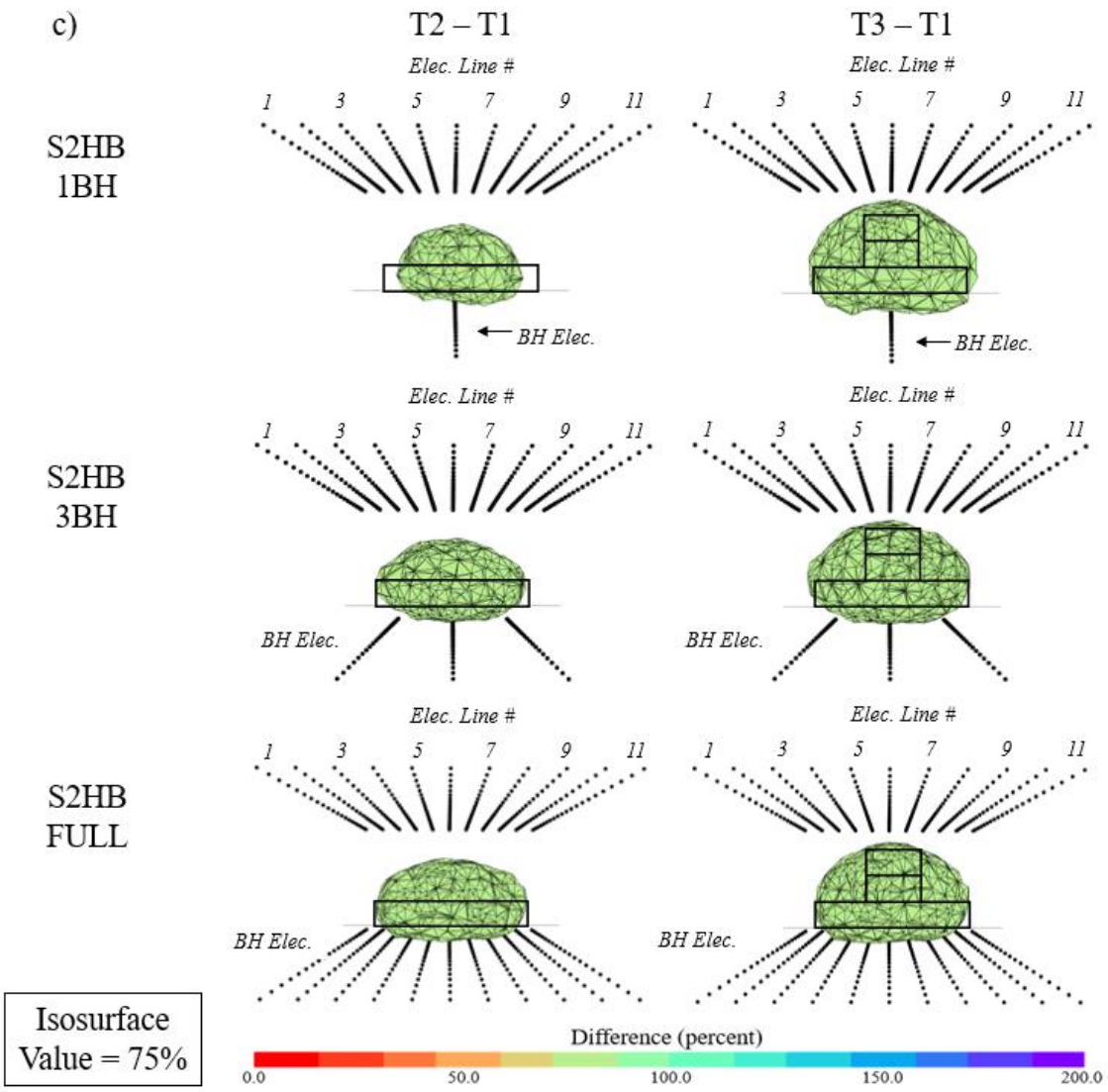
c)
T2 – T1
T3 – T1
Elec. Line #
1 3 5 7 9 11
S2HB
1BH
BH Elec.
S2HB
3BH
S2HB
FULL
Isosurface
Value = 75%
Difference (percent)
0.0
50.0
100.0
150.0
200.0

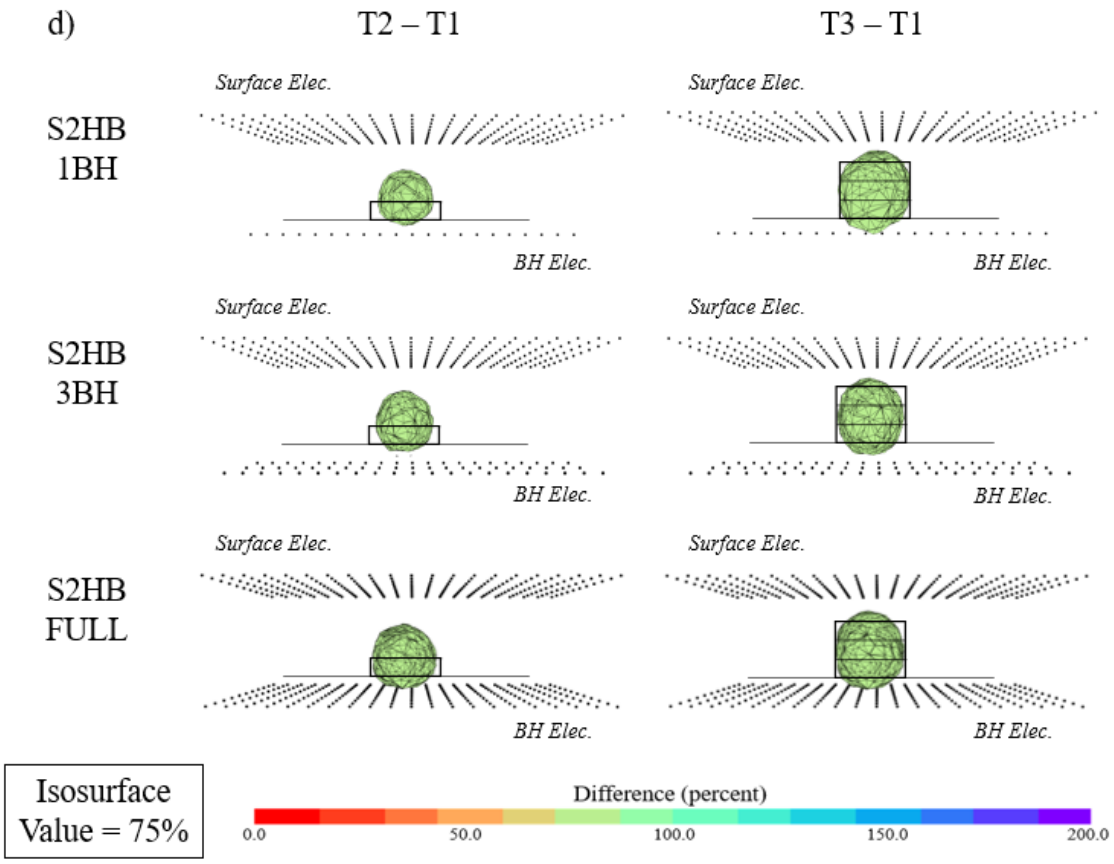
d)
T2 – T1
T3 – T1
S2HB 1BH
S2HB 3BH
S2HB FULL
Surface Elec.
BH Elec.
Isosurface Value = 75%
Difference (percent)
0.0
50.0
100.0
150.0
200.0

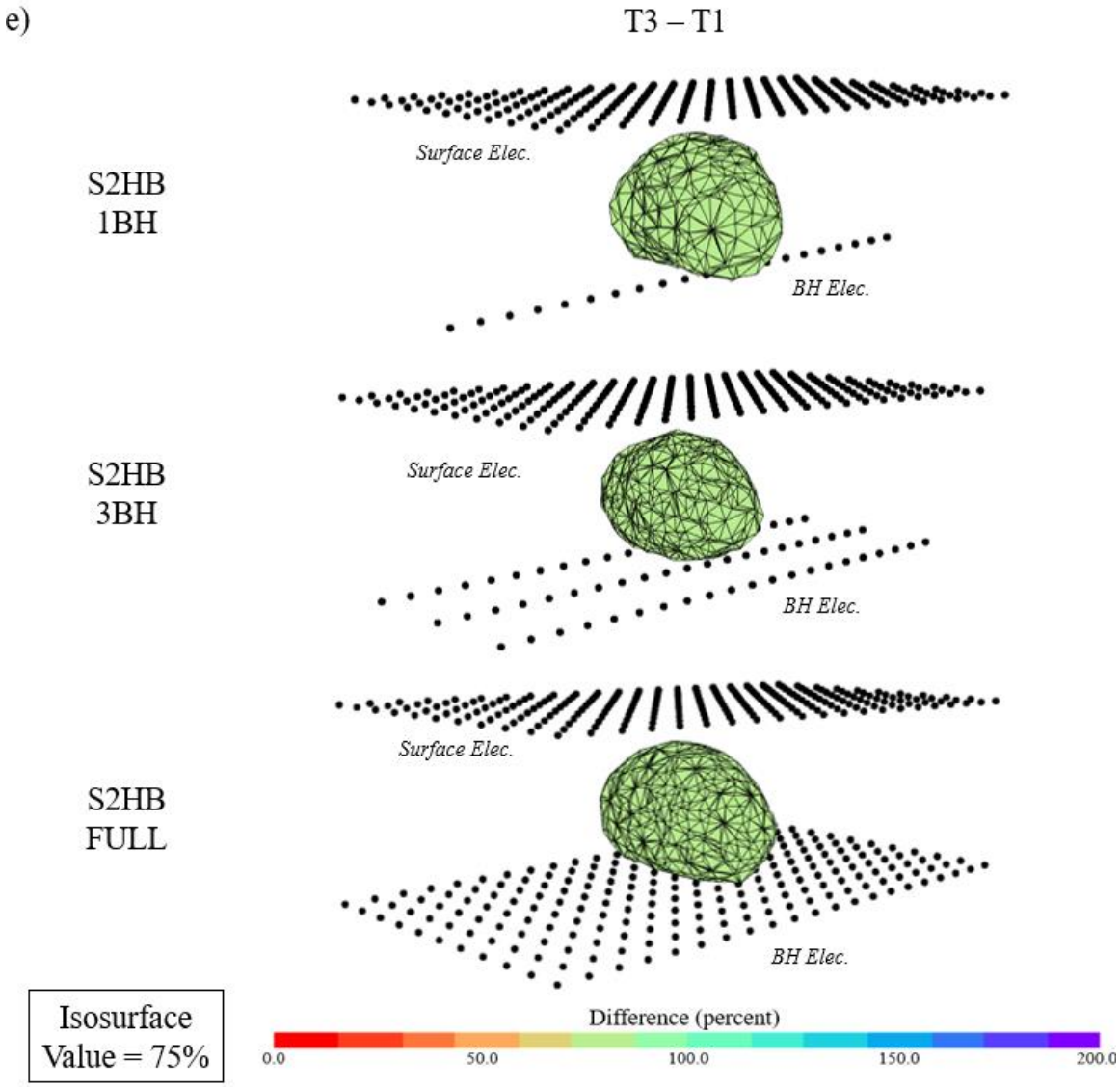

Figure A-1: Numerical model results from S2HB-1BH, S2HB-3BH and S2HB-FULL imaging of Inverted-T: (a) cross-sectional slices of the inverted 3D resistivity domain at time-steps T1, T2 and T3, (b) cross-sectional slices of the difference (%) images between T1 and T2, and T1 and T3, (c) front view of the 3D isovolume differences (75%), (d) side view of the 3D isovolume differences (75%), and (e) oblique view of 3D isovolume differences (75%).

Curriculum Vitae

Name:	Maxwell Servos
Post-secondary Education and Degrees:	The University of Western Ontario London, Ontario, Canada 2015-2020 B.E.Sc
Related Work Experience:	Graduate Research Assistant The University of Western Ontario 2017
	Graduate Teaching Assistant The University of Western Ontario 2020-2022